Fathoming ice

Using non-linear ultrafast spectroscopy to look at interfacial ice properties

ISBN NUMBER: 978-3-949783-01-2

Fathoming Ice

Using non-linear ultrafast spectroscopy to look at interfacial ice properties

ACADEMISCH PROEFSCHRIFT

ter verkrijging van de graad van doctor
aan de Universiteit van Amsterdam
op gezag van de Rector Magnificus
prof. dr. ir. K.I.J. Maex
ten overstaan van een door het College voor Promoties ingestelde commissie,
in het openbaar te verdedigen in de Agnietenkapel
op donderdag 25 november 2021, te 13.00 uur

door Prerna Sudera
geboren te Delhi

Promotiecommissie

Promotores:	prof. dr. E.H.G. Backus	Universiteit van Amsterdam
	prof. dr. M. Bonn	Universiteit van Amsterdam
Overige leden:	prof. dr. S. Woutersen	Universiteit van Amsterdam
	prof. dr. W.J. Buma	Universiteit van Amsterdam
	dr. J.D. Cyran	Baylor University
	dr. C. Ramanan	Vrije Universiteit Amsterdam
	prof. dr. N.F. Shahidzadeh	Universiteit van Amsterdam

Faculteit der Natuurwetenschappen, Wiskunde en Informatica

CONTENTS

Chapter 1

Water and Ice – structure and properties

Water, a ubiquitous substance on Earth, is chemically one of the simplest compounds, yet a contentious topic of scientific research. An accurate theoretical model of water remains elusive; notably one of the top 125 questions of the 125th anniversary of Science[1,2] was 'what is the structure of water?' Constituting three atoms, the water molecule has four sp^3-hybridized electron pairs, giving it a tetrahedral arrangement. The partial charge on the oxygen and hydrogen atoms gives the water molecule its polar character; which in turn leads to a water molecule being able to form hydrogen bonds with up to four of its closest neighbours. Hydrogen bonds can be 10-100 times weaker than covalent bonds, making quick rearrangements possible for water molecules whilst maintaining a three-dimensional cohesive structure.

Hexagonal ice, Ice I_h, is the most commonly encountered solid phase of water. Ice currently is known to have 19 different crystalline structures[3] under conditions of varying temperature and pressure.

Structure of water molecule

The structure of an isolated water molecule, in its gaseous state, is represented in Figure 1.1. The equilibrium O-H distance is 0.96 Å and the H-O-H angle is 104.5°; these values were deduced from the rotational components of the rotation-vibration spectrum[4]. As apparent from Figure 1.1, the water structure is bent, and not linear (like CO_2), and this form gives it a dipole moment.

The two H atoms and an O atom covalently bond together to form a water molecule. In its condensed states, water molecules interact to form a cohesive network via hydrogen bonds. This is a distinct type of chemical bonding that occurs when an H atom lies between two of the highly electronegative atoms like F, O, or N. Interestingly, hydrogen bonding is effective only for the first row of the electronegative atoms in the periodic table – explaining why HCl due to its larger molecular weight is not able to form hydrogen bonds and is thus a gas at room temperature. This hydrogen bonding between water molecules is what 'binds' the molecules together into a liquid; and accounts for the arrangements of molecules in ice.

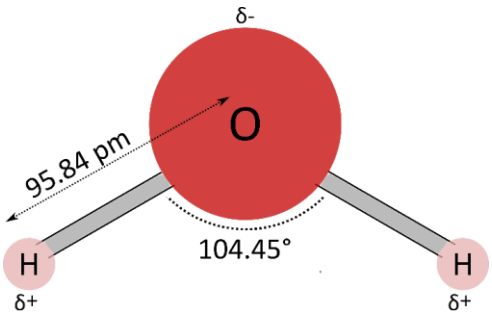

Figure 1.1: dimensions of an isolated water molecule

A hydrogen bond, represented as O-H…O, is weaker than a covalent bond H–O. Thus the O…H distance is larger than the O-H distance. A hydrogen bond donor is the molecule to which the hydrogen is covalently bonded, and the other molecule is the hydrogen bond acceptor. Water, because of its polar nature is very effective at transferring additional charges by rearrangement of molecular configurations, by the Grotthuss hopping mechanism. This mechanism is based on the 'relay' of protons by a series of water molecules, instead of a single proton diffusing through water. The solvation of excess protons occurs in two limiting forms: the Eigen – where the proton is associated with one central water molecule H_3O^+, and Zundel – where the proton is equally shared with two neighbouring water molecules forming a complex $H_5O_2^+$. Proton hopping involves cooperative efforts of water molecules upto the second solvation shell for a periodic isomerization of the Eigen and Zundel structures[5].

Structure of ice

The structure of ice in its stable state under ordinary conditions is known as Ice-I (one), which exists in two different crystalline forms – hexagonal, which is called Ice-Ih; and cubic, called Ice-Ic. Both these forms of ice are represented in the phase diagram of water shown in Figure 1.2. Ice-Ih forms under normal pressure and temperature conditions, and is thus also the most widely-existing terrestrial form of ice – in the form of snowflakes, ice crystals in the atmosphere, ice sheets and glaciers, etc. Ice-Ic is formed by depositing vapour at very low temperatures (below 120 K). Besides these, another 15 different crystalline structures of ice have been shown to exist under varying temperature and pressure conditions; and three different types of amorphous ice (low density, high density, and very high density) have been characterized. Ice-Ih is the focus of this thesis and all references to ice in the thesis are directed to Ice-Ih, unless explicitly mentioned otherwise.

The crystalline structure of ice is comprised of oxygen atoms arranged on a hexagonal lattice, where it has four nearest neighbours at the corners of a tetrahedron. Each H_2O molecule donates two hydrogen bonds, and also accepts two hydrogen bonds, hence making a tetrahedral arrangement of hydrogens around the oxygen atom. Although a crystalline structure, a long-ranging orientational order in ice is absent.

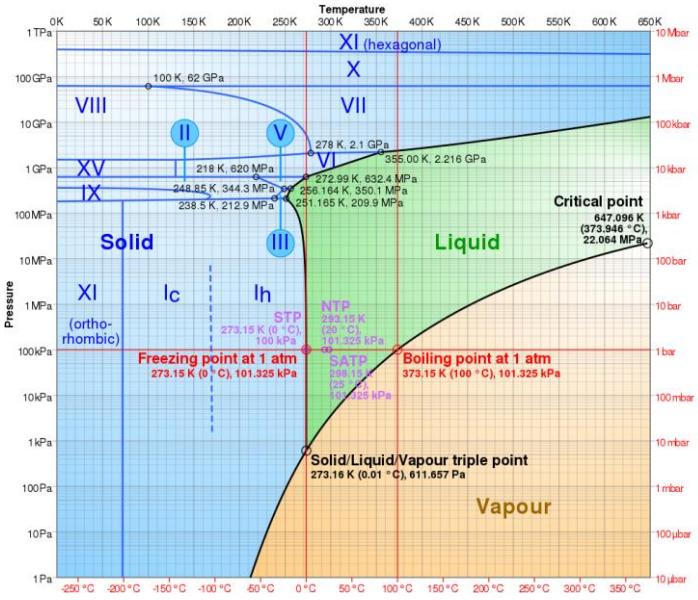

Figure 1.2: phase diagram of water from reference[6]

Crystalline structure

The hexagonal crystal representation of ice is shown in Figure 1.3. Part b shows a hexagonal lattice system, with the unit cell marked in bold lines. The unit cell is enough to represent the lattice symmetry, the 'full' hexagonal prism arrangement comprised of three unit cells is marked in dotted lines. The water molecules with the oxygen atoms corresponding to the hexagonal unit cell are shown coloured in part a of the figure, and as is apparent from the figure, the unit cell contains 4 water molecules. When looking down perpendicular to the c-axis, the oxygen atoms stack in the sequence ABAB, the A and B layers marked on the left figure. The hexagonal rings have a puckered shape, giving the stacking sequence a bi-layered form. The unit cell elucidates that the two sides of the cell have an equal length with an enclosed angle of 120 degrees. When this property is translated to the hexagonal prism, it gives it a 6-fold rotation axis. A hexagonal system is usually referenced by Miller-Bravais lattice notation, introducing a 4th direction, written as the 3rd index. The Miller-Bravais system hence uses 4 instead of 3 indices as in the Miller notation. The usage of 4 indices makes it easier in terms of crystallographic representation to deduce plane and direction symmetry as a permutation of lattice indices.

Three different planes, that correspond to the basal, primary prism, and secondary prism planes are highlighted and indexed in Figure 1.4. The space group of hexagonal ice is $P6_3/mmc$; where the first and the second m denote the mirror plane perpendicular and parallel to the c-axis; c denotes glide planes; 6_3 denotes the multiplicity and screw of the pitch axes, P denotes Primitive instead of Centred structure[7].

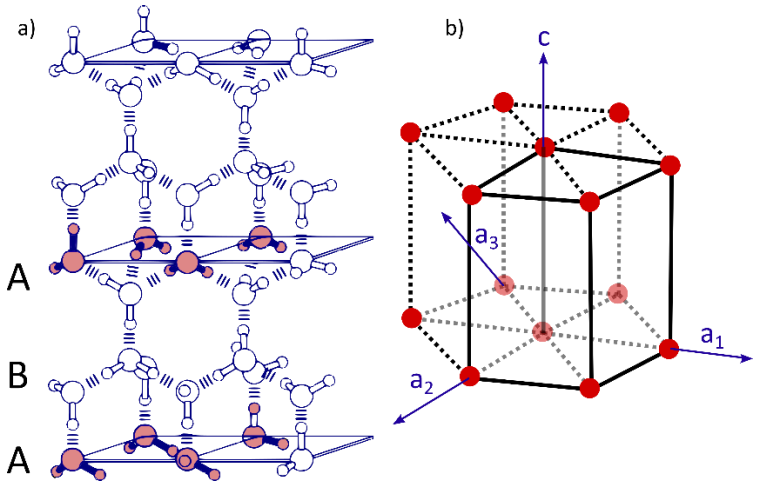

Figure 1.3: crystalline structure of hexagonal ice; left: molecular representation of the unit cell, also showing the ABA stacking sequence; right: unit cell in the hexagonal structure; image adapted[8]

The bi-layered arrangement of the oxygen atoms can be appreciated better in Figure 1.4 which shows the side views of the different plane orientations of the crystal system. It was shown that the interfacial molecules at the basal plane of ice melt in a bilayer-by-bilayer manner[9], whereas those at the secondary prism plane melt in a layer-by-layer manner; and Figure 1.4 is a pictorial explanation behind that. The figure also illustrates clearly the different plane orientations of the ice crystal with molecular and crystalline representations.

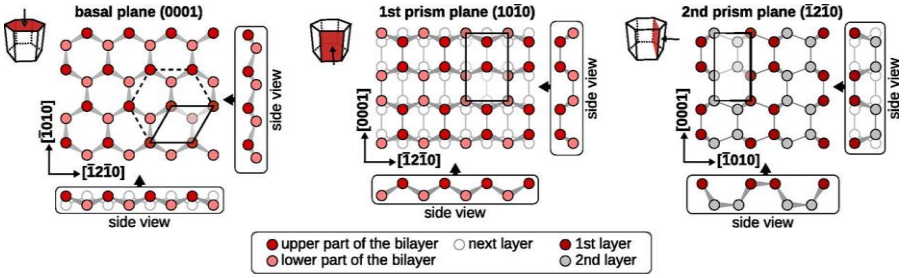

Figure 1.4: images representing the different orientation planes of the hexagonal ice structure[9]

Ice rules and orientational disorder

In 1921, Dennison, was the first person to determine unit cell parameters, and in 1922, Bragg used them to propose the structure of ice as we know now, based on positions of oxygen atoms. The determination of hydrogens atoms had to wait until 1949 using neutron diffraction. There is an inherent orientational disorder present in ice, which can be explained as follows: every individual water molecule can share its two covalently-bonded hydrogens to only two other water molecules when there are four to choose from. This

constrained arrangement can have 6 different directional configurations. The concept of disorder can be better visualized in Figure 1.5: in the left figure, the central water molecule donates two hydrogen bonds to the two water molecules above it; in its disordered phases one of them shown on its right side, it would donate to any two of the water molecules available.

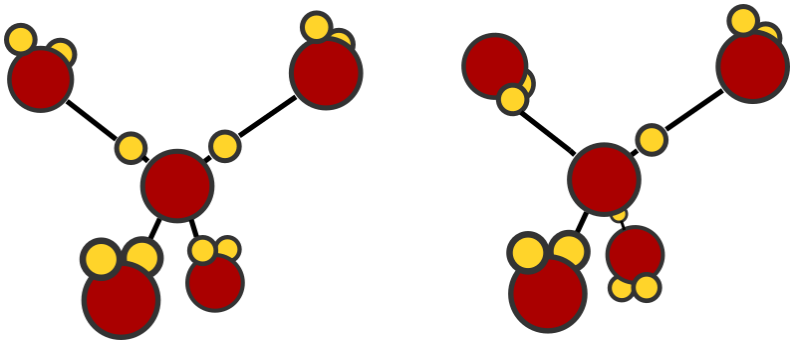

Figure 1.5: left: proton ordered arrangement wherein the central water molecule donating two hydrogen bonds to water molecules above it, and accepting two hydrogen bonds from water molecules below it; right: one of the disordered phases shown; Image adapted[10].

Bernal and Fowler, in 1933, laid down basic ice rules that govern the arrangement of atoms in ice. The rules state that each oxygen atom is covalently bonded to two hydrogen atoms, and an oxygen atom in each water molecule is hydrogen bonded to other oxygen atoms, leading to precisely only one hydrogen atom between each pair of oxygen atoms. Pauling in 1935 estimated that there are $(3/2)^N$ different ways to arrange H-bonds of N water molecules, subject to the ice rules formulated by Bernal and Fowler. A disorder in the structure, thermodynamically introduces entropy in the system, which would be R ln 3/2 = 0.806 cal K^{-1} mol^{-1}. This orientational disorder in the ordered lattice gives rise to distinct properties like electrical polarizability and conductivity, because of which ice is often described as a protonic semiconductor.

The presence of a disordered state also postulates the existence of an ordered equilibrium state at or before 0 K. This concern was solved in the 1980s when KOH-doped ice exhibited a proton-ordering transition at 72 K. This proton-ordered structure was called Ice-XI. The transition temperature from Ice-Ih to Ice-XI was independent of the KOH concentration, suggesting that it was required only as a catalyst. However, the requirement of 'defects' for the transformation process is also thought of as a violation of the ice rules.

At the surface where there is a break in symmetry, the disorder in the orientation of molecules in the ice crystal is suspected to change for electrostatic stability. Quantum chemical simulations have shown that proton ordering affects the surface energies by an order of magnitude more than the effect on bulk energies[11]. The ice surface was thought to have a ferroelectric ordering, determined from neutron diffraction[12] data and simulations[13], but the idea was challenged and the surface of ice subsequently is claimed to be antiferroelectric[14]. Computational studies expect the surface to be proton-ordered in specific alternate arrangements, known as Fletcher pattern. Experimentalists have been in the hope of being able to confirm or negate this hypothesis. Chapter 5 is an attempt towards answering this question, using SFG spectroscopy to explore ways to characterize proton ordering, if any, at the surface of ice.

Water – absorption spectrum

This thesis is about studying the structure and dynamics of water in its liquid and solid states, using its interaction with light as the measurement tool. Water absorbs light across a wide range of frequencies, being transparent only in the visible region. Light in the UV frequency range is absorbed by water through excitation of electronic modes; In the visible region, the weak absorption of red light is caused by various combinations of overtones of intramolecular bands, giving water a slightly blue tinge. The strongest vibrational mode of water is at ~3400 cm^{-1}. Going further to the red side, the bend mode appears around 1640 cm^{-1}, followed by wagging and librational modes, and finally the intermolecular vibrations and collective motion of water molecules. At very low frequencies, corresponding to wavelengths longer than 10 m, the water starts becoming transparent again, making radio communication possible in water by sub marines.

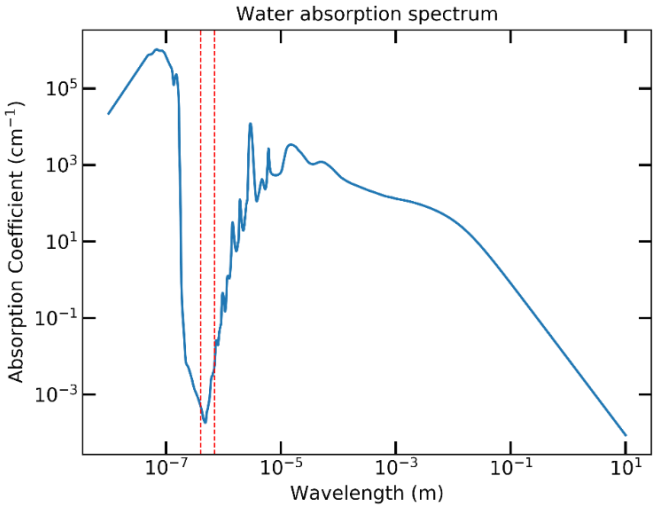

Figure 1.6: absorption spectrum of water, adapted from reference[15,16].

Vibrational modes of ice

For an ice crystal with N molecules, there would be 3 N normal modes of vibration. In a perfect crystal, the normal vibrations can be described as standing waves with a constant amplitude through the crystal and can be described by a wave vector. In an orientationally-disordered crystal-like ice, as has been described before, the intermolecular coupling constants are not periodic in space and so vibrational amplitudes are not periodic either. There are no selection rules applying in terms of the wave vector, and hence all vibrations are spectroscopically active. This explains why the Infrared and Raman spectra of ice, as shown in Figure 1.7, show an almost continuous response throughout the range displayed.

The fundamental frequencies of an isolated H_2O molecule, and H_2O and D_2O ice are presented in table 1.1, and represent the intramolecular vibrations of the water molecule. ν_1 and ν_3 depend on the force constant for stretching the covalent O-H bond: where a symmetric stretch vibrates at ν_1=3652, and the asymmetric

stretch v_2=3756 cm^{-1}. v_2 depends on the force constant for changing the bond angle, thereby leading to the H-O-H bending motion at v_2=1595 cm^{-1}. For ice, the intricate intermolecular coupling between the molecules results in a band of vibrations, which are severely complicated to disentangle and interpret. Essentially the spectrum can be divided into four distinct regions: a) intramolecular O-H stretching vibrations around 3300 cm^{-1} derived from v_1 and v_3 of the isolated H_2O molecule; b) intramolecular bending vibration at 1600 cm^{-1} derived from v_2; c) intermolecular rotational vibrations around 840 cm^{-1}; and d) intramolecular translational vibrations peaking at 230 and 165 cm^{-1}.

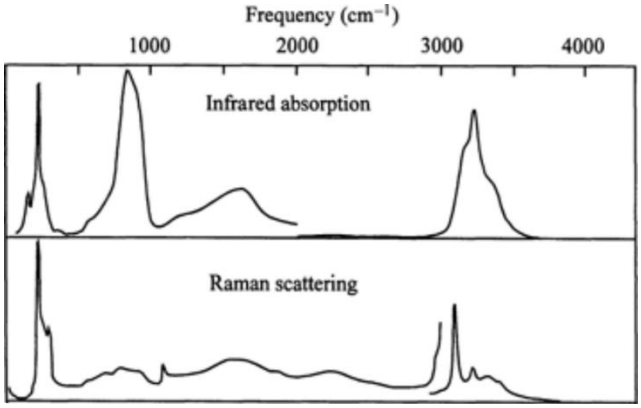

Figure 1.7: IR and Raman spectra of ice; infrared absorption (Bertie *et al.* 1969), Raman spectroscopy (Wong and Whalley 1975, 1976); figure from reference[17].

The stretch mode of ice has been extensively studied, because of easier acquisition of signal. Recently there is attention starting to be paid to the bend mode of ice, and chapter 4 will focus on the bend mode of interfacial ice, with an extensive temperature-dependent and polarization-dependent study. The aim is centred around finding how the bend mode responds to temperature changes, and how the differences in polarization-dependent signals can be explained.

Table 1.1: Vibrational peak assignments for an isolated water molecule and hexagonal ice[7]:

	H_2O vapour	H_2O ice	D_2O ice
v_1 (cm^{-1})	3652	3143	2347
v_2 (cm^{-1})	1595	1640	1210
v_3 (cm^{-1})	3756	3252	2440

In chapter 6, we come back to the stretch mode, and look at the dynamics of the oscillators in the stretch mode. So far, we have only talked about static information received from spectroscopic data, but using ultrafast lasers and pump-probe experiments, time-resolved molecular information on a femtosecond scale can be measured. Methods are discussed on how these results can be modelled and interpreted, and what can we gain from them in a bigger picture.

Preparation of single-crystalline ice

Multiple methods have been reported in the literature to produce single-crystalline ice samples: surface cooling of water by rapid evaporation under reduced pressure, variants of the Czochralski technique involving elevation of a seed crystal, and growing ice via a capillary into a wider glass tube using the Sapporo or the Bridgeman techniques. Ice for all the measurements in this thesis was grown using the Czochralski method, for which the starting seed was procured using the Lake ice technique.

Lake ice

This method propagates the growth of single-crystalline ice as it would naturally on a cold undisturbed lake surface. Treated milliQ water is poured into a cleaned Petri-dish, covered and kept undisturbed in a freezer at -20° C. Over time, nucleation of ice should start, and the water starts freezing, usually from the surface, down to the bottom. Often times an eruption of the surface was seen when water at the bottom would start to freeze beneath the already-frozen surface. Under conditions of undisturbed nucleation of ice, a few centimetre-wide cubes of single-crystalline ice blocks in an overall polycrystalline sample would be formed. The largest of such a single, or poly-crystalline areas was cut off using a bandsaw in the freezer. This would act as a seed crystal for the Czochralski process to grow much larger single-crystalline boules.

In Chapter 7, the role of structural order in the efficiency of a biologically-relevant ice-nucleating agent, cholesterol, is explored using experimental and simulation methods.

Czochralski method

The Czochralski method, which involves the extraction of a seed from the melt, is widely used to produce single crystals of metals, semiconductors, salts, and synthetic gemstones. The method established in our laboratory, was applied to obtaining single-crystalline ice boules, inspired by the work of S. Roos[18]. The setup involves a water bath maintained at around 0.5°C, a copper finger maintained at -14°C that acted as a heat sink and was adjustable in height and tilt angle, and a seed crystal, approximately 4 x 4 cm and 2-4 cm thick to start with. The water bath is constantly stirred to promote agitation and constant movement for thermal equilibrium and also to prevent bubble formation at the air-water interface. The copper finger is attached to a Peltier element with liquid back-cooling, allowing temperature control. Temperatures of both the bath and the copper finger are monitored throughout. The seed is melt-attached to the copper finger: the copper finger is cooled at a rate of ~5°C/minute from room temperature conditions; at ~5°C, the seed placed flat on a Teflon substrate is pressed against the copper finger, the cooling rate of which is increased to 10-15°C/minute, to avoid complete melting of the seed. The seed attaches as the surface of the seed touching the finger melts, and there is subsequent freezing as the temperature goes down. An image of the attached seed to the copper finger is presented in Figure 1.8a.

After seed attachment, the temperature of the copper finger is maintained at -14°C. Thereafter, the bottom surface of the attached seed is melted using a heat gun to create a molten layer of water, and it is translated immediately to the top of the bath using the adjustable height and tilt settings of the copper finger setup. The seed is lowered slowly to immerse only a couple of millimetres into the water bath, maintained at a temperature of around 0.5°C. The seed is allowed to stay in that position for half an hour or more depending

on the size of the boule one aims to produce. In that period, the seed stabilizes into a wider block of ice, that continues to get bigger the longer it stays. The seed is then pulled out of the water bath at an optimized rate using an automated height adjustment system that the copper finger is mounted to. The rate of extraction depends on the dimensions of the final boule size. We would like our boules to be around 8-10 cm in wide, and 10 cm long cylindrically shaped, to slice out 5 cm thick samples for experiments. For these dimensions, we had optimized the pulling rate to be nearly 5 mm per hour. Ice would usually grow over a period of 24 hours.

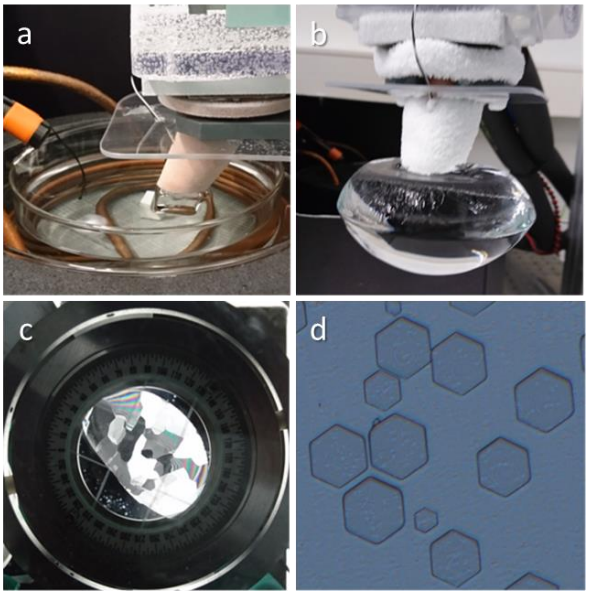

Figure 1.8: steps to making single-crystalline ice

When the boule looks satisfactory in size, the process is stopped and the ice is extracted by raising the boule out of the bath; an example of the boules produced is shown in Figure 8b. At this point, to release the boule from the copper finger, the temperature of the finger is raised to above the melting point of water to let the boule just drop from the finger, which is caught by gloved hands. The boule was kept in the freezer immediately after release from the finger, undisturbed for equilibration reasons, and to avoid immediate cracks or defects because of sudden temperature changes and handling.

Characterization of single crystals

Cross-polarizer setup

Ice is birefringent, thereby having an ordinary wave that has the same velocity in all directions, and an extra-ordinary wave that travels with a different speed of light in different directions, producing a phase shift. At the optical axis the two waves meet, the optical axis of ice coincides with its c-axis. Therefore, using a cross-

polarizer setup, it is possible to determine the c-axis of the ice sample. A cross-polarizer setup, also called a Rigsby stage, consists of two orthogonal polarizers. In between the two polarizers there is space to insert and rotate a sample. Without any sample between the first polarizer and the second polarizer (called the analyser), the transmitted light is completely extinguished by the two orthogonal polarizers. With a polycrystalline sample within the polarizer and analyser, light incurs a phase shift between the ordinary and extra-ordinary waves when passing through ice, changing the polarization. This causes the sample to appear bright, and the brightness varies for differently oriented domains of the polycrystalline sample, an example of which is shown in Figure 1.8c. The outgoing light is completely extinguished for the cases when the optical axis of the ice is aligned with either the polarizer or the analyzer, or when the c-axis is parallel to the line of sight. When the c-axis is indeed parallel to the line of sight, rotation in that axis should remain dark at all angles. This would be the basal or 0001 plane of ice.

The accuracy of using a Rigsby stage is a user-dependent process. Although it can offer complete information, it was used only to roughly estimate the basal plane, and to check the single-crystallinity of the sample. For a more quantitative determination of the crystal-orientation, Formvar etching was performed.

Formvar etching

Crystallographic information from the ice surface can be obtained in the form of etched pits using thermal and anisotropic etching, known as Formvar etching. A thin slice of ice (10-20 mm thick) is obtained using a bandsaw, it is vital to pay attention to the viewing plane of the cut slice in reference to the boule to pinpoint the correct axis. The ice slice is melt-attached onto a glass cover slip: the ice slice is rubbed over the glass slide to initiate melting of the contact surface of ice, after which it is placed in the centre of the slide and moved to the freezer to attach. After attachment, the sample is placed in a microtome holder to produce a flat and smooth surface for the etching process. Thereafter, the cover slip is mounted onto a microscope holder. A 2% solution of polyvinyl formal (Formvar) in ethylene dichloride is used to cover the surface of the thin ice slice using a clean cotton swab. After the solvent evaporates, a polymer film forms on the sample.

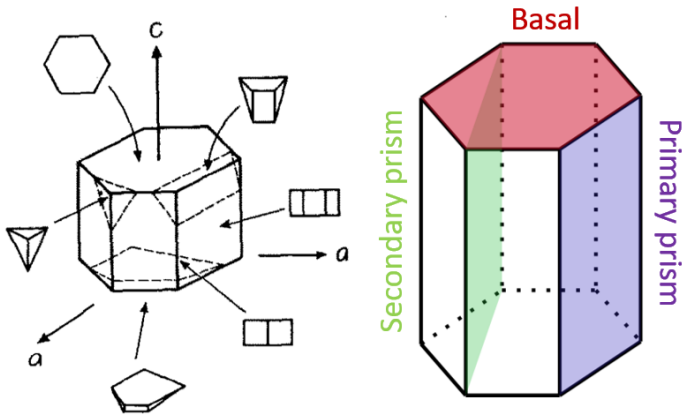

Figure 1.9: a) etch pits shapes for different orientation plane cut, from reference[19]; b) basal, and the prism planes of ice depicted in the hexagonal crystalline structure.

The polymeric film causes the formation of etched pits as water starts to evaporate through small randomly distributed holes of the film. The etched pits take the shape associated with the lattice structure dependent on the crystal orientation, and start from tiny pits and increase in size with time due to continuous evaporation of water. From the shape of the pits, it is thus possible to determine the orientation of the axis. The basal plane leaves hexagonally-etched pits, an example of which is shown in Figure 1.8d. Other shapes of the pits are shown in Figure 9a, corresponding to the plane orientations of the crystal shown in Figure 1.9b. The microscope used was Olympus BX40, at a magnification of 40X, and Nikon Digital Sight DS-U2 camera was used to take photographs.

When starting with a crystal seed not already basal-oriented, the sample orientation can be far from that desired. The etch pit images help to obtain the degree to which the orientation plane is off. Having an estimate of the angles, based on the shadows of the etched pits in one or multiple directions, the boule is cut at the respective angle in a direction referenced to the slice of ice being observed for etched pits. This can be a tedious, iterative process, based on trial and error in the beginning. Once the desired plane orientation is obtained, enough ice is grown to always have a seed for the next growth process of the correct orientation.

Sample preparation for measurements

After an ice boule is correctly oriented to the desired plane, a parallel disc of ice (~5 mm), maintaining the same orientation, is cut from the boule using a bandsaw. A stainless steel device, with high mass concentration at one end, and very thin features in the shape of a circle (4.4 mm) on the other end, is used as a 'cookie cutter.' The thick side helps to take up the heat when heated before usage, and transfer it while cutting the disc using the thin sharp side, assisting the cut with some melting from the heat. Once the disc is cut in the right dimensions, it is melt-attached to a pin in the centre of an aluminium ice cell. The ice cell with ice attached to it can be seen in Figure 1.10 b and c, with the aluminium pin with grooves in the middle.

After attachment to the cell, the cell is screwed to a microtome holder, as shown in Figure 10a. The microtome used was an adapted version of a Swift and Anderson Rotary Microtome. The ice attached to the cell is microtomed, by moving the ice cell up and down in reference to the microtome blade. The microtome blade chosen after trying at least 15 different types, was a Leica three-facetted blade. When the ice cell is positioned above the blade, it is moved in minimal distance steps over the microtome blade position, and then lowered to scrape off the ice. This is an extremely important step that determines the ice surface quality.

To obtain an optically-flat ice sample, the step sizes of ice scraping are kept small, and the cell is moved slowly and smoothly while scraping to avoid line ridges. An optically flat shining sample after microtoming is shown in Figure 1.10b. The reflectivity of some direct light was a good check of the sample surface. After microtoming, the ice cell is then closed air-tightly within a Calcium Fluoride window, and a plastic cap is threaded closed to retain air-tightness, shown in Figure 1.10c. The ice cell is left overnight for annealing so the surface can reach an equilibrium state.

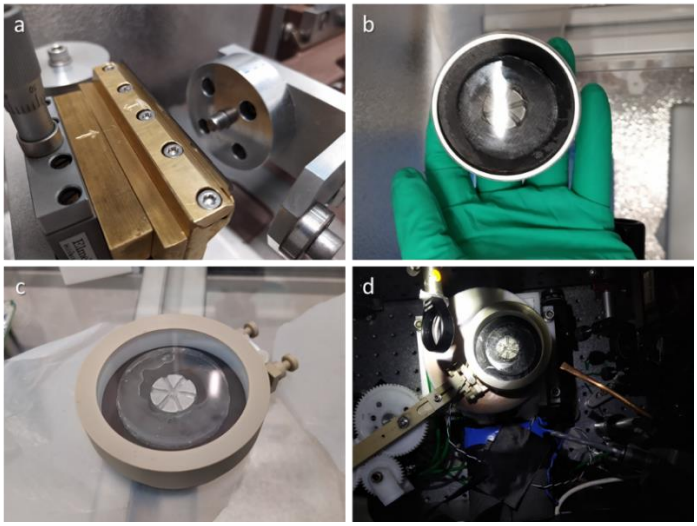

Figure 1.10: a) microtome; b) microtomed ice sample in its cell; c) ice sample covered by a Calcium Fluoride window, allowed to anneal; d) ice cell in the setup, rotation enabled using a crank-shaft mechanism upon a Copper cooling stage

The ice cell is subsequently transferred to the setup in the lab for measurements. The ice cell in the setup rotates over a copper cooling stage using a crank-shaft mechanism and an additional wobbling. The ice cell is rotated at a rate so that every pulse from the laser (assuming a ~100 µm diameter) hits a subsequent new spot on the ice, thus avoiding the accumulation of heat in the sample and preventing it from melting. The copper plate can be cooled down to 218 K, and the aluminium cell being a good thermal conductor can attain temperatures almost as close. The temperatures of the ice (by drilling a hole in the ice and placing a sensor), and the ice cell corresponding to the temperature of the copper block were recorded for reference to the ice temperature later. The setup was purged to avoid condensation over the cell or copper block, and a nitrogen jet pipe placed close to the cell would avoid condensation over the cell window.

Outline

Having had a general overview so far about the structure, properties, and synthesis of crystalline ice, the subsequent chapters are outlined as follows. Chapter 2 and 3 give an overview on the theory of non-linear light-matter interaction, ultrafast lasers and Sum Frequency Generation spectroscopy, followed by a brief explanation of the experimental setup, and data analysis. Chapter 4 to 6 present experimental results pertaining to the ice surface, discussing specifically the vibrational bend mode, proton order, and dynamics of the vibrational stretch mode, respectively. Finally, Chapter 7 showcases experimental and simulation results on the ice-nucleating properties of cholesterol monolayers.

A brief summary of the PhD work closes the thesis.

Chapter 2

Static and time-resolved optical interactions

Introduction to Nonlinear Interactions

Nonlinear optics encompasses all phenomena for which the response of a material system to an applied optical electric field depends nonlinearly on the strength of the applied field. Linear optical phenomena (like reflection, refraction, absorption) occur when the applied electric field is relatively weak (~10^3 V/cm) and the material response varies linearly with the strength of the applied field. Nonlinear effects occur when the applied electric field is of an order comparable to the electric field in matter (which is around 10^9 V/cm). Such intense fields can be generated using powerful pulsed lasers, and can cause nonlinear effects like intensity-dependent refractive index leading to the Kerr effect, generation of light beams of another frequency, like Sum Frequency Generation (SFG), Difference Frequency Generation (DFG), third harmonics; and other effects like stimulated Raman scattering, two-photon absorption, self-phase modulation, etc. Nonlinear optical effects were discovered in 1961[20] upon demonstration of Second Harmonic Generation (SHG) in a nonlinear crystal using a ruby laser, soon after the ruby maser[21] was invented in 1960.

The equation for the propagation of a light wave can be derived from Maxwell's equations, considering a non-magnetic medium with no free charges and no free currents, and is represented as:

$$\nabla^2 \tilde{\mathrm{E}} + \frac{\epsilon^{(1)}}{c^2}\frac{\partial^2 \tilde{\mathrm{E}}}{\partial t^2} = -\frac{1}{\epsilon_0 c^2}\frac{\partial^2 P}{\partial t^2} \qquad \text{Eq. 2.1}$$

where ϵ_0 is the electric permittivity in vacuum, $\epsilon^{(1)}$ is the relative permittivity, c is the speed of light, $\tilde{\mathrm{E}}$ is a time-varying electric field, and P is the polarization. A neat derivation to Equation 1 can be found here[22]. The equation is an inhomogeneous differential equation, with the polarization acting as a source term: the polarization can serve as an appropriate representative quantity for the induced electric field in the medium. Polarization in a medium upon interaction with an external field must obey causality; it is not induced instantaneously. Hence, the more general form as a function of time is:

$$P(t) = \epsilon_0 \int_{-\infty}^{t} \chi_e(t-t')E(t')dt' \qquad \text{Eq. 2.2}$$

which says that the polarization is a convolution of the electric field at previous times with the time-dependent susceptibility given by $\chi_e(\Delta t)$. A Fourier Transform of the above function gives a more convenient frequency-dependent function:

$$P = \epsilon_0 \chi_e(\omega) E(\omega) \qquad \text{Eq. 2.3}$$

where χ_e is the linear electric susceptibility. Eq. 3 holds true when the light entering a medium has a low intensity.

When the electric field E of the incident light increases, the polarization of the medium is no longer linearly-dependent, but is instead expanded in a power series. Writing $E = E_1 \cos\omega t$, the induced Polarization becomes:

$$P = \epsilon_0 \left(\chi^{(1)}(E_1 \cos \omega t) + \chi^{(2)}(E_1 \cos \omega t)^2 + \chi^{(3)}(E_1 \cos \omega t)^3 + \cdots \right) \qquad \text{Eq. 2.4}$$

which can be written as:

$$P = \epsilon_0 \left(\begin{array}{c} \chi^{(1)} E_1 \cos \omega t + \frac{\chi^{(2)}}{2} E_1^2 (1 + \cos 2\omega t) + \\ \frac{\chi^{(3)}}{4} E_1^3 (3 \cos \omega t + \cos 3\omega t) + \cdots \end{array} \right) \qquad \text{Eq. 2.5}$$

where $\chi^{(1)}$, $\chi^{(2)}$, $\chi^{(3)}$ are the first, second, and third – order susceptibilities, which are associated with the linear, second, and third – harmonic responses of the polarization. Equation 2.5 states that an intense external electric field upon interaction with a medium causes an induced polarization in the medium, which then emits light at twice (Second Harmonic Generation), thrice (Third Harmonic Generation), etc. the frequency of the incident field E_1. The susceptibility is a complex quantity containing optical information of the dielectric material. The real part of the susceptibility is associated with the refractive index, and the imaginary part to the absorption coefficient. It is easier to directly measure the absorption properties of a material and hence the imaginary part of the susceptibility. The real part is usually indirectly inferred using the Kramer-Kronig relations. It can be measured directly using phase-sensitive measurements utilizing a local oscillator of known phase as a reference.

The susceptibility is a tensor because the electrons in a material, when an electric field is applied, experience a restoring force in the direction of the field, and also additional forces from the neighbouring molecules. Hence, Equation 4 should ideally be written incorporating forces in x, y and z directions in the Cartesian coordinate system:

$$P_i = \chi_{ij}^{(1)} E_j + \chi_{ijk}^{(2)} E_j E_k + \chi_{ijkl}^{(3)} E_j E_k E_l + \cdots \qquad \text{Eq. 2.6}$$

where i,j,k,l each denote the x,y,z Cartesian components; and summation should be performed for the repeated indices.

Second Order Nonlinear Phenomena

If the incident external field is a sum of two different oscillating fields, E_1 and E_2, then the total incident field can be expressed as:

$$E = E_1 \cos \omega_1 t + E_2 \cos \omega_2 t$$

Substituting the combined E field in the second-order term of Equation 2.5:

$$P^2 = \epsilon_0 \chi^{(2)} (E_1 \cos \omega_1 t + E_2 \cos \omega_2 t)^2 \qquad \text{Eq. 2.7}$$

which gives the following four terms:

$$E_1^2 + E_2^2;$$
$$E_1^2 \cos 2\omega_1 t + E_2^2 \cos 2\omega_2 t;$$
$$\frac{E_1 E_2 \cos(\omega_1 - \omega_2)t}{2};$$
$$\frac{E_1 E_2 \cos(\omega_1 + \omega_2)t}{2}$$

Eq. 2.8

The first term depicts the generation of a static DC field, the second terms depicts the SHG, the third and fourth terms depict the DFG and SFG effects, respectively.

Nonlinear optical media and Phase-Matching

The generation of these nonlinear fields requires an effective medium. This can be elaborated by considering the incoming laser beam to be a monochromatic plane wave at frequency ω_1 and with a wave vector k_1, hence having an electric field $E(r,t) = E_0 \cos(k_1 r - \omega_1 t)$, and inducing a second-order polarization at the modulated frequency $2\omega_1$ or $\omega_1 + \omega_2$. The macroscopic second-harmonic wave produces a large intensity only when the phase-velocities of the incoming waves and the outgoing wave are synchronized. The phase velocity in a medium is characterized by the index of refraction n(ω):

$$v_{ph} = \frac{\omega}{k} = \frac{c}{n(\omega)}$$

The phase-matching condition is fulfilled when:

$$k_3(\omega_3) = k_1(\omega_1) + k_2(\omega_2)$$

or

$$\Delta k = k_3(\omega_3) - k_1(\omega_1) - k_2(\omega_2) = 0 \qquad \text{Eq. 2.9}$$

Since the wave vector k is related to photon momentum $p = \frac{h}{2\pi} k$, the condition simply states that the law of conservation of momentum is obeyed when three photons participate in the process of frequency mixing. When all the beams are collinear, the condition can be replaced by:

$$n_3\omega_3 = n_1\omega_1 + n_2\omega_2 \qquad \text{Eq. 2.10}$$

For the SHG process, $\omega_1 = \omega_2$, and $\omega_3 = 2\omega_1$, hence Equation 2.10 takes the form $n(2\omega_1) = n(\omega_1)$. This would imply that SHG may only be efficiently generated when the index of refraction at $2\omega_1$ equals that at ω_1. This is typically not possible because dispersion dictates that waves of different wavelengths do not experience the same indices of refraction.

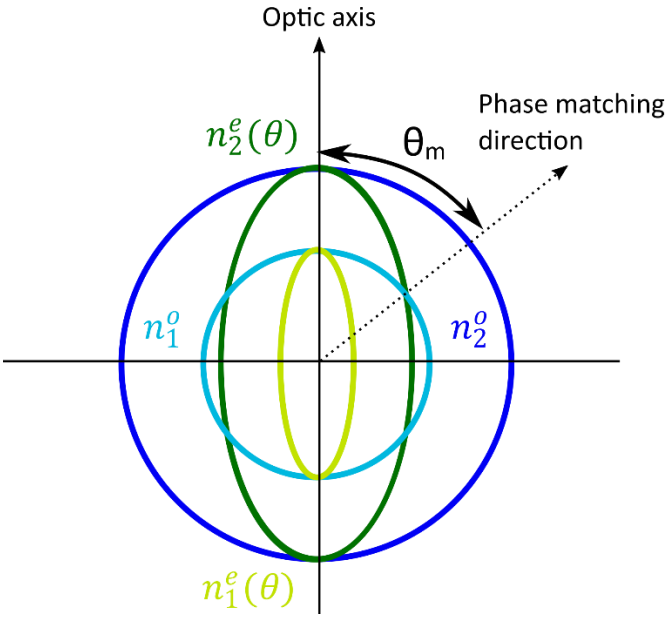

Figure 2.1: Phase-matching direction in a negative uniaxial crystal; n_1 is refractive index of the fundamental, and n_2 of the second harmonic.

However, birefringent crystals are often used to make the condition hold true, utilizing their orientation- and polarization-dependent refractive indices. Many anisotropic crystals that have an optical axis (including calcite, quartz, ice, etc.) are birefringent, meaning that the light beam undergoing refraction divides into two rays: the ordinary and the extraordinary ray, both of them being linearly polarized in planes perpendicular to each other. The ordinary beam is polarized orthogonal to the optical axis of the material, and propagates along the same direction, regardless of crystal orientation. The extraordinary beam, however, propagates at a different velocity as it takes a different propagation upon crystal rotation, depending on the angle between the polarization direction to the optical axis of the material. Thus for the ordinary beam, the index of refraction n^o is independent of the direction of propagation (θ), in contrast to the extraordinary index of refraction n^e, whose value changes from the maximum equal to n^o, and minimum when the direction of beam propagation is perpendicular to the optical axis[23]. The following equation describes the dependency of n^e on the angle θ which the beam propagation makes with the optical axis z:

$$n^e(\theta) = \frac{n^o n^e}{[(n^o)^2 sin^2\theta + (n^e)^2 cos^2\theta]^{1/2}}. \qquad \text{Eq. 2.11}$$

Figure 2.1 shows the cross sections of the refractive indices for the fundamental and second harmonic in a negative uniaxial crystal. There are certain directions of propagation in the crystal where the fundamental and second harmonic have the same refractive index, along θ_m. Propagation of the laser beam along this direction hence leads to the fulfillment of the phase-matching condition.

Centro-symmetry effects

Second-order nonlinear effects, by theory, only occur in non-centrosymmetric media. The following is the proof for the statement[24]. In a centrosymmetric media, forces are balanced in all directions, and the value of $\chi_{ijk}^{(2)}$ for two opposing directions must be equal, that is:

$$\chi_{ijk}^{(2)} = \chi_{-i-j-k}^{(2)} \qquad \text{Eq. 2.12}$$

However, as $\chi_{ijk}^{(2)}$ is a third-rank tensor, changing signs of the three subscripts must lead to reversing the axis system. Therefore,

$$\chi_{ijk}^{(2)} = -\chi_{-i-j-k}^{(2)} \qquad \text{Eq. 2.13}$$

Equations 2.12 and 2.13 can both together only hold true when $\chi_{ijk}^{(2)} = 0$. Hence, second-order effects are forbidden in centrosymmetric media. However, at an interface, the bulk-like behaviour terminates and therefore surfaces are second-order active. Hence, planar isotropic surfaces, symmetric about the surface normal, having a C_∞ rotation axis (shown in figure 2.2), are good candidates for second-order nonlinear effects.

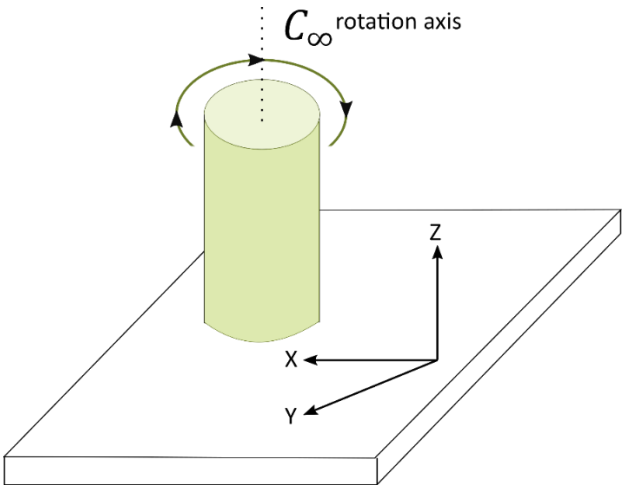

Figure 2.2: A planar surface symmetric about the surface normal

From this symmetry, z ≠ -z, but x ≡ -x and y ≡ -y. Reversal of an axis would imply a negative sign on $\chi^{(2)}$ according to Equation 2.13. Hence, the symmetry conditions for the C_∞ plane along with application of Equation 2.13 leaves only zzz and quadratic x or y terms from the 27 tensor elements of $\chi^{(2)}$ being non-zero. Such terms are mentioned below:

$$\chi^{(2)}_{zxx} = \chi^{(2)}_{zyy};\ \chi^{(2)}_{xxz} = \chi^{(2)}_{yyz};\ \chi^{(2)}_{xzx} = \chi^{(2)}_{yzy};\ \chi^{(2)}_{zzz}$$

Basic principle of Sum Frequency Generation, influence of Fresnel factors

SFG is a second-order process, and, therefore, surface-specific, as discussed in the previous section. Since work in this thesis focuses on SFG, a more detailed theoretical framework on it is presented.

A general equation of the SFG process can be represented as:

$$P^{(2)} = \epsilon_0 \chi^{(2)} E_{Vis} E_{IR} \qquad \text{Eq. 2.14}$$

where the two beams of different, infrared (IR) and visible (Vis), frequencies overlap on the sample in space and in time to generate a subsequent SFG beam. The IR beam is broadband, can be tuned and is overlapped in the resonant-frequency range of the sample; the visible beam is narrow in frequency, kept fixed and used for upconversion of the IR absorption signal to get an outgoing SFG beam in the near-visible frequency range. The addition of the visible beam hence makes the signal second-order and hence surface-specific, and also makes signal detection easy. The angle of the SFG beam to the surface normal follows the phase-matching condition.

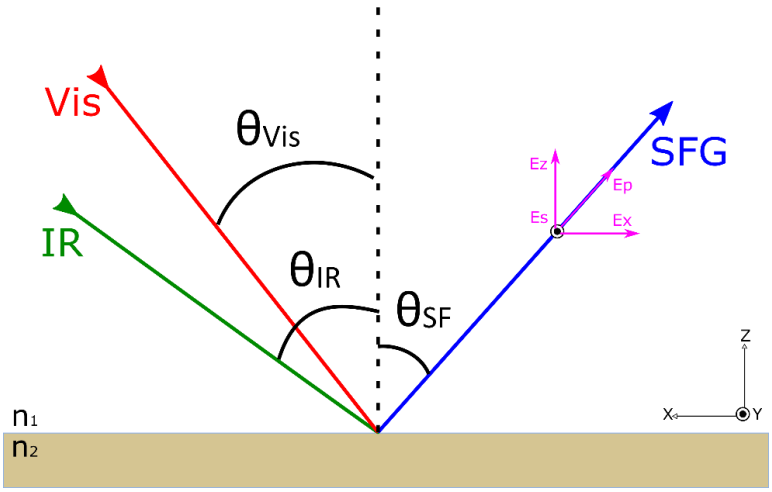

Figure 2.3: Illustration depicting SFG generation from incident Vis and IR beams; also showing parallel and perpendicular electric field coordinates.

Eq. 2.14 is a rather simplified version of the overall SFG phenomenon. The presence of $\chi^{(2)}$, which is a third-rank tensor, implies 27 different directions have to be considered. This can be represented by utilizing Cartesian coordinates for the induced polarization, and both the incident fields, which brings us to the following equation:

$$P_{SF}^{(2)} = \sum_{i}^{x,y,z} P_{i,SF}^{(2)} = \epsilon_0 \sum_{i}^{x,y,z} \sum_{j}^{x,y,z} \sum_{k}^{x,y,z} \chi_{ijk}^{(2)} E_{j,Vis} E_{k,IR} \qquad \text{Eq. 2.15}$$

For example, a polarization induced in the x direction by the E fields in the x and z axes, can be represented by:

$$P_{x,SF}^{(2)} = \epsilon_0 \chi_{x,x,z}^{(2)} E_{x,Vis} E_{z,IR} \qquad \text{Eq. 2.16}$$

Which accounts only for 1/27th of the total contributions of the SF signal from the surface given by Equation 15.

From figure 2.3, s (perpendicular to the z-x plane) and p (parallel to the z-x plane) polarizations of an incident electric field can be split into the Cartesian components by general trigonometric relations:

$$E_x^I = \pm E_p^I \cos\theta_I;\ E_y^I = E_s^I;\ E_z^I = E_p^I \sin\theta_I$$

Under the electric dipole approximation, the nonlinear polarization generated in media 1 and 2 with refractive indices n_1 and n_2 must vanish due to inversion symmetry, and the sum frequency intensity in the reflected direction from the interfacial polarization sheet is given by[25]:

$$I(\omega) = \frac{8\pi^3 \omega_{SFG}^2 sec^2\beta_{SFG}}{c^3 n_1(\omega_{SFG}) n_1(\omega_{Vis}) n_1(\omega_{IR})} \left|\chi_{eff}^{(2)}\right|^2 I(\omega_{Vis}) I(\omega_{IR}) \qquad \text{Eq. 2.17}$$

where n_i is the refractive index of medium i, β_{SFG} is the reflection angle of the SF field.

The local electric field is determined by the Fresnel coefficients which take into account the frequency-dependent refractive indices of the interfacial and bulk media. As mentioned above, assuming an azimuthal isotropic interfacial geometry, only 4 out of 27 independent, non-vanishing $\boldsymbol{\chi}^{(2)}$ tensor components remain. If z is along the interface normal, and x in the incidence plane, these tensor components are: $\chi_{xxz}^{(2)}$=$\chi_{yyz}^{(2)}$, $\chi_{xzx}^{(2)}$=$\chi_{yzy}^{(2)}$, $\chi_{zxx}^{(2)}$=$\chi_{zyy}^{(2)}$, and $\chi_{zzz}^{(2)}$. For SFG measured in SSP and PPP polarization combinations, these translate into[25]:

$$\chi_{\text{eff,SSP}}^{(2)} = L_{yy}(\omega_{SFG}) L_{yy}(\omega_{Vis}) L_{zz}(\omega_{IR}) \sin\beta_{IR} \chi_{yyz} \qquad \text{Eq. 2.18}$$

$$\begin{aligned}\chi_{\text{eff,PPP}}^{(2)} = &-L_{xx}(\omega_{SFG}) L_{xx}(\omega_{Vis}) L_{zz}(\omega_{IR}) \cos\beta_{SFG} \cos\beta_{Vis} \sin\beta_{IR} \chi_{yyz} \\ &-L_{xx}(\omega_{SFG}) L_{zz}(\omega_{Vis}) L_{xx}(\omega_{IR}) \cos\beta_{SFG} \sin\beta_{Vis} \cos\beta_{IR} \chi_{xzx} \\ &+L_{zz}(\omega_{SFG}) L_{xx}(\omega_{Vis}) L_{xx}(\omega_{IR}) \sin\beta_{SFG} \cos\beta_{Vis} \cos\beta_{IR} \chi_{zxx} \\ &-L_{zz}(\omega_{SFG}) L_{zz}(\omega_{Vis}) L_{zz}(\omega_{IR}) \sin\beta_{SFG} \sin\beta_{Vis} \sin\beta_{IR} \chi_{zzz}\end{aligned} \qquad \text{Eq. 2.19}$$

ω_{SFG}, ω_{Vis}, and ω_{IR} correspond to SFG, Visible and IR frequencies. $\chi^{(2)}_{xzx}$ and $\chi^{(2)}_{zxx}$ are neglected considering their approximately equal and small magnitude, and the opposite signs of their respective equations, that is lines 2 and 3 of equation 2.19.

$L_{xx}(\Omega)$, $L_{yy}(\Omega)$, $L_{zz}(\Omega)$ are the diagonal elements of $L(\Omega)$, and are defined as:

$$L_{xx}(\Omega) = \frac{2\, n_1(\Omega)\cos\beta_2}{n_1(\Omega)\cos\beta_2 + n_2(\Omega)\cos\beta};$$

$$L_{yy}(\Omega) = \frac{2\, n_1(\Omega)\cos\beta}{n_1(\Omega)\cos\beta + n_2(\Omega)\cos\beta_2};$$

$$L_{zz}(\Omega) = \frac{2\, n_2(\Omega)\cos\beta}{n_1(\Omega)\cos\beta_2 + n_2(\Omega)\cos\beta}\left(\frac{n_1(\Omega)}{n'(\Omega)}\right)^2 \qquad \text{Eq. 2.20}$$

where Ω is the corresponding SFG (ω), Vis (ω_1) or IR (ω_2) frequency; and n' is the refractive index of the interface, often defined[25] as: $n' = \sqrt{\frac{n_1^2 + n_2^2 + 4}{2(n_1^{-2} + n_2^{-2} + 1)}}$

β and β_2 are the beam angles in medium 1 and 2.

Macroscopic Averaging

$\chi^{(2)}$ represents a macroscopic average of the molecular quantity β, the hyperpolarizability, of the molecules at the surface. Molecular hyperpolarizabilities use a molecular-bound coordinate system, and to represent a macroscopic $\chi^{(2)}$, one employs Euler's identity rules to relate the coordinate and the molecular-bound systems.

The sum of hyperpolarizabilities of all adsorbed molecules in a given volume gives $\chi^{(2)}$:

$$\chi^{(2)}_{ijk} = \frac{N}{\epsilon_0}\sum_{\alpha\beta\gamma}\langle R(\psi)R(\theta)R(\varphi)\beta_{\alpha\beta\gamma}\rangle \qquad \text{Eq. 2.21}$$

where $R(\psi)R(\theta)R(\varphi)$ is the product of three rotation matrices using all three Euler angles to convert from the molecular to the surface coordinate system; the $\langle\rangle$ brackets indicate the orientational averages and N is the number of molecules per unit volume.

The equation below is a general expression for $\beta_{\alpha\beta\gamma}$

$$\beta_{\alpha\beta\gamma} = \frac{1}{2\hbar}\frac{M_{\alpha\beta}A_\gamma}{(\omega_\upsilon - \omega_{IR} - i\Gamma)} \qquad \text{Eq. 2.22}$$

where ω_{IR} is the tuneable IR frequency, ω_υ is the vibrational resonance frequency, Γ is the dephasing time of the vibrational resonance. $M_{\alpha\beta}$ and A_γ are the Raman and IR transition moments, respectively. The above equation lays down the selection rules of an SF-active vibration: the vibration has to be both IR and Raman active.

Interpretation of SFG using density matrices, and Feynman diagrams

General introduction to eigenstates, coherences and emitted field:

Light-molecule interaction is treated semi-classically: the time-dependent electric field is treated classically, and the vibrational states of a molecule quantum mechanically. Considering a gas-phase molecule with only one vibrational mode, the energy of interaction between the molecule's dipole and an external electrostatic field is given by: $\widehat{W}(t) = \hat{\mu}\, E(t)$. The total Hamiltonian then is $\widehat{H} = \widehat{H}o + \widehat{W}(t)$ where $\widehat{H}o$ is the Hamiltonian for an isolated molecule. $\widehat{H}o$ is time-independent in the absence of a laser pulse, however the coefficients themselves are time-dependent during interaction with the laser pulse, as the laser field is coupling the molecular eigenstates. Keeping all that into account, for a two-level system with a ground state and an excited state, two coupled equations as a solution to the time-dependent equations are obtained[26]:

$$\frac{\partial}{\partial \mathrm{t}} c_1(t) = +\frac{i}{h} c_0(t) e^{-i\omega_{01}t} \langle 1|\hat{\mu}|0\rangle E(t)$$
$$\frac{\partial}{\partial \mathrm{t}} c_0(t) = +\frac{i}{h} c_1(t) e^{+i\omega_{01}t} \langle 0|\hat{\mu}|1\rangle E(t)$$

Eq. 2.23

where $\langle n|\hat{\mu}|m\rangle = \frac{d\mu}{dx}\langle n|\hat{x}|m\rangle$ is defined as the transition dipole moment, having two terms, dμ/dx which gives the transition dipole strength, and the second term that gives the selection rules; x is the coordinate of the vibrating bond. After solving the above coupled equations for a two-level system, after interaction with the laser pulse, the molecule is in a linear combination of eigenstates of $|0\rangle$ and $|1\rangle$

$$|\psi(t)\rangle = c_0 e^{-iE_0 t/h}|0\rangle + ic_1 e^{-E_1 t/h}|1\rangle$$

Eq. 2.24

where c_n includes the transition dipole and other factors. This equation implies that the laser pulse creates a coherent linear superposition of states, in other words a wavepacket. The time dependence of this wavepacket is defined by the intrinsic time-dependence of the molecular Hamiltonian, and is known as the molecular response, R(t). This state is equivalent to the laser pulse pulling and pushing the charges to get the molecules vibrating[27].

The macroscopic polarization P(t) is measured by detecting the emission field created by the oscillating charges following Maxwell's equations. P(t) is calculated as the expectation value of the transition dipole[27]:

$$\begin{aligned} P(t) &= \langle \mu \rangle = \langle \psi(t)|\hat{\mu}|\psi(t)\rangle \\ &= (c_0 e^{iE_0 t/h}\langle 0| - ic_1 e^{iE_1 t/h}\langle 1|)\,\widehat{\mu}\,(c_0 e^{-iE_0 t/h}|0\rangle + ic_1 e^{-iE_1 t/h}|1\rangle) \\ &= c_0 c_1 \langle 0|\hat{\mu}|1\rangle \sin(\omega_{01} t) + c_0^2\langle 0|\hat{\mu}|0\rangle + c_1^2\langle 1|\hat{\mu}|1\rangle \end{aligned}$$

Eq. 2.25

the last two terms of the equation represent the molecule's static dipoles in its ground and first excited states, and these being time-independent, do not contribute to the emission of the electric field. Also, the coefficient c_1 is proportional to their transition dipoles, as can be seen from equation 2.23, so P(t) becomes:

$$\begin{aligned} P(t) &\equiv c_0 c_1 \mu_{01} \sin(\omega_{01} t) \\ &\propto +\mu_{01}^2 \sin(\omega_{01} t) \end{aligned}$$

Eq. 2.26

As per Maxwell's equations, oscillating charges create an electromagnetic wave which is 90° phase-shifted with respect to the macroscopic polarization[26,27]. Hence, P(t) = $\mu_{01}^2 \sin(\omega_{01} t)$ will create and emitted electric field proportional to $-\mu_{01}^2 \cos(\omega_{01} t)$, which is at the fundamental frequency between $|0\rangle$ and $|1\rangle$.

Brief introduction to density matrix formalism

For molecules in a condensed state where the vibrational frequencies of each molecule are slightly different from one another, statistical treatment of the quantum mechanical description is required. The density matrix provides one way of doing that. The density matrix replaces the wave function, and repackages information from the time-dependent Schrödinger equation, enabling one to do relatively simple calculations of the time dependence of expectation values.

Considering a 2-level system, where the laser pulse interacts only with the $|0\rangle$ and $|1\rangle$ quantum states, the density matrix is defined as[27]:

$$\rho = \begin{pmatrix} \rho_{00} & \rho_{01} \\ \rho_{10} & \rho_{11} \end{pmatrix} = \begin{pmatrix} \langle c_0(t) c_0^*(t) \rangle & \langle c_0(t) c_1^*(t) \rangle \\ \langle c_1(t) c_0^*(t) \rangle & \langle c_1(t) c_1^*(t) \rangle \end{pmatrix} \quad \text{Eq. 2.27}$$

The diagonal terms are the populations, the off-diagonal elements are the coherences and are ultimately the source of the emitted field.

When dephasing and population relaxation are considered to be absent, the time evolution of the density matrix elements is described as[26]:

$$\begin{aligned} \rho_{00}(t) &= c_0^2 = constant \\ \rho_{11}(t) &= c_1^2 = constant \\ \rho_{01}(t) &= -ic_0 c_1 e^{+i\omega_{01} t} \\ \rho_{10}(t) &= ic_0 c_1 e^{-i\omega_{01} t} \end{aligned} \quad \text{Eq. 2.28}$$

Homogeneous dephasing is a result of the time decay of the off-diagonal elements, described[27] utilizing a homogeneous dephasing time T_2:

$$\begin{aligned} \rho_{01}(t) &= -ic_0 c_1 e^{+i\omega_{01} t} e^{-t/T_2} \\ \rho_{10}(t) &= ic_0 c_1 e^{-i\omega_{01} t} e^{-t/T_2} \end{aligned} \quad \text{Eq. 2.29}$$

Also, population relaxation results in the decay of ρ_{11} with a time constant T_1, together with refilling of the ground state ρ_{00}.

$$\begin{aligned} \rho_{11}(t) &= \rho_{11}(0)\, e^{-t/T_1} \\ \rho_{00}(t) &= 1 - \rho_{11}(t) \end{aligned} \quad \text{Eq. 2.30}$$

Homogeneous dephasing T_2 and population relaxation T_1 are related by:

$$\frac{1}{T_2} = \frac{1}{2T_1} + \frac{1}{T_2^*} \quad \text{Eq. 2.31}$$

T_2^*, which is the pure dephasing time is caused by the fluctuations of the environment.

The density matrix can also be expressed using quantum mechanical operators: $\rho = |\psi\rangle\langle\psi|$. Its matrix elements are found by expanding the wavefunction in an eigenstate basis:
$|\psi^s\rangle = \sum_n c_n^s |n\rangle$ and for its conjugate complex: $\langle\psi^s| = \sum_n c_n^s \langle n|$ where s is a molecule in the system. Taking an ensemble average over all molecules, we get: $\hat{\rho}_{nm} = \langle c_n c_m^* \rangle \, |n\rangle\langle m|$ which means that the matrix elements $\langle c_n c_m^* \rangle$ of the density operator are related to a coherence $|n\rangle\langle m|$ between states $|n\rangle$ and $\langle m|$. The polarization is calculated by:

$$\langle \mu \rangle = \sum_{nm} \langle c_n c_m^* \rangle \mu_{mn} = \sum_{nm} \rho_{nm} \mu_{mn} \qquad \text{Eq. 2.32}$$

The right side of the equation above is called the trace of $\rho\mu$

$$\langle \mu \rangle = Tr(\rho\mu) = \langle \rho\mu \rangle \qquad \text{Eq. 2.33}$$

Density matrix for the SFG process

To take into account the interaction of a laser pulse with a molecule, ρ is multiplied by μ, from both the bra and ket sides. This procedure, upon interaction of one pulse gives:
$\rho^{(1)} = i(\mu(0)\rho(-\infty) - \rho(-\infty)\mu(0))$, where $\rho^{(1)}$ is a first-order term in the Taylor expansion of the density matrix.
The macroscopic polarization evolves as per the molecular response, and is obtained by taking the trace $\langle \mu(t_1)\rho^{(1)} \rangle$ to get the linear response function or the first-order response function[27]:
$R^{(1)}(t_1) = i\langle \mu(t_1)\mu(0)\rho(-\infty) \rangle - i\langle \rho(-\infty)\mu(0)\mu(t_1) \rangle$ which is slightly rearranged using invariance of the trace under cyclic permutation
$R^{(1)}$ is the first term of the perturbative expansion of the molecular wavefunctions to incorporate interaction with the light field.

Depending on which side the μ acts on the density matrix, we can have different pathways to how an interaction proceeds. When a dipole operator acts from its left side on a density matrix in its ground state, $i\mu(0)\rho(-\infty) = i \begin{pmatrix} 0 & 1 \\ 1 & 0 \end{pmatrix} \begin{pmatrix} 1 & 0 \\ 0 & 0 \end{pmatrix} = \begin{pmatrix} 0 & 0 \\ i & 0 \end{pmatrix}$ there is coherence generated in the (10) state. If the dipole operator however acts from its right side on the density matrix in its ground state $i\rho(-\infty)\mu(0) = i \begin{pmatrix} 1 & 0 \\ 0 & 0 \end{pmatrix} \begin{pmatrix} 0 & 1 \\ 1 & 0 \end{pmatrix} = \begin{pmatrix} 0 & i \\ 0 & 0 \end{pmatrix}$ then the coherence is generated in the (01) state.
There are two pathways to the interaction of a single laser pulse, these are called the Liouville pathways or Feynman pathways:
$(\rho_{00} \rightarrow \rho_{01} \rightarrow \rho_{00}) \equiv (|0\rangle\langle 0| \rightarrow |0\rangle\langle 1| \rightarrow |0\rangle\langle 0|)$ and
$(\rho_{00} \rightarrow \rho_{10} \rightarrow \rho_{00}) \equiv (|0\rangle\langle 0| \rightarrow |1\rangle\langle 0| \rightarrow |0\rangle\langle 0|)$

To incorporate the effect of the electric field of the external pulse in the macroscopic polarization generation in the medium, ideally, the time-dependent Schrödinger equations should be solved for each of the molecules comprising the system, which is not realistic. Hence, the linear response theory is used wherein it is assumed that the laser pulse is weak. Under the linear response theory, the first-order response function is convoluted with the laser pulse. The electric field of the laser pulse is formally described as two terms with positive and negative frequencies. This is applied for the rotating wave approximation, wherein, upon convolution, when μ operates on the ket (left), it is $E(t)$ that creates the coherence, and we obtain for the linear polarization: $P^{(1)}(t) = \int_0^\infty dt_1 \, E(t - t_1) R^{(1)}(t_1)$ where $E(t) \propto e^{-i\omega t}$; whereas when μ operates on the bra (right) side, the $E^*(t)$ which is $\propto e^{+i\omega t}$ creates the coherence.

Finally, the macroscopic polarization can be represented rather well and compactly with Feynman diagrams. In the double-sided Feynman diagrams below, time runs from the bottom to the top; two vertical lines are used to represent evolution of the bra (right) and ket (left) sides of the density matrix. Interactions with the dipole operator at a given time are represented by arrows, and the corresponding matrix element to denote a coherence or population state is noted between two vertical lines.

For the linear response, there are two pathways, as explained before, each pathway having two possibilities because of interaction with the electric field with positive frequencies, $E(t) \propto e^{-i\omega t}$, or negative frequencies, $E^*(t) \propto e^{+i\omega t}$. This creates four Feynman diagrams as in Figure 2.4.

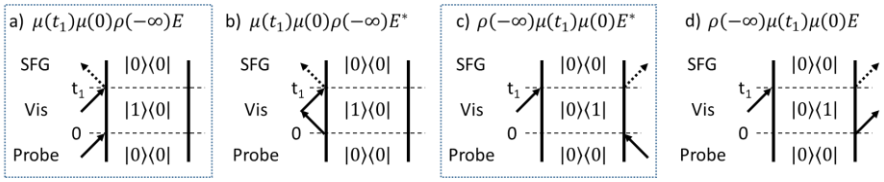

Figure 2.4: Feynman diagrams for the static SFG process

In the Feynman diagrams, $E(t) \propto e^{-i\omega t}$ is depicted by an arrow pointing right, and $E^*(t) \propto e^{+i\omega t}$ by an arrow pointing to the left. As explained before, figure b does not survive the RWA for the left term of the linear response where μ acts on the ket side of the density matrix (shown by a $|1\rangle\langle 0|$ coherence in figures a and b). Similarly, figure d also dissolves under the RWA for the second terms of the first-order linear response.

Probing vibrational dynamics of interfacial systems

The following section will look into using SFG in a time-resolved manner, to capture the ultrafast dynamics of vibrational motion of molecular systems. Optoelectronic systems used for photon detection as of yet do not have the resolution to measure phenomena occurring at a femtosecond level. The most efficient systems are capable of a few picoseconds, which is too slow for the field of femto-chemistry[28,29]. To probe dynamics at the femtosecond timescale, a pump-probe scheme is implemented where the time resolution of the measurement becomes independent of the resolution of the electronic devices. Some other techniques like photon echo, or CARS, etc. are also well-developed techniques, however this thesis would focus on pump-probe SFG spectroscopy, applied for surface-specific vibrational measurements.

Pump-Probe SFG

In a pump-probe SFG experiment, the time resolution is obtained by implementing a variable time-delay between the pump beam – which excites the sample of interest, and the probe beam (a probe pair here – visible and IR beams together) which probes the sample after excitation, progressively in time. The vibrational spectra thus acquired at multiple time points after excitation by the pump, provides information on reaction intermediates, vibrational couplings, spectral diffusion, and vibrational relaxation time constants. This

information is useful for understanding general reaction mechanisms, especially on interfaces, with applications in atmospheric sciences, electrochemistry, biological reactions, etc.

An excitation-level diagram for the pump-probe scheme for SFG experiments is depicted in Figure 2.5, where the pump and probe pulses cover the same frequency region. The pump pulse strikes the sample, and due to its high intensity, causes a certain number of oscillators to be excited from the v = 0 to v = 1 state (represented in lightly shaded circles). This excitation of oscillators requires two interactions with the electromagnetic field: the first interaction with the electromagnetic field causes a coherence state, and the second interaction causes the actual excitation of the oscillator. The excited state now has fewer oscillators in its ground state, such that the probe-pair when incident on the sample, generates a less-intense SFG signal compared to the unpumped situation. Both the pumped and unpumped signals are independently recorded in a pump-probe experiment. The relative decrease in intensity of the generated SFG signal is what is known as 'bleach' and is represented as a difference or ratio of the pumped and unpumped SFG signals. The presence of excited-state oscillators in the v = 1 state when the probe-pair interacts with the sample, leads to an additional two signals: the excited state absorption (ESA), which probes the absorption of oscillators from the v = 1 to v = 2 vibrational states; and stimulated emission (SE) which causes relaxation of excited-state oscillators in v = 1 to v = 0.

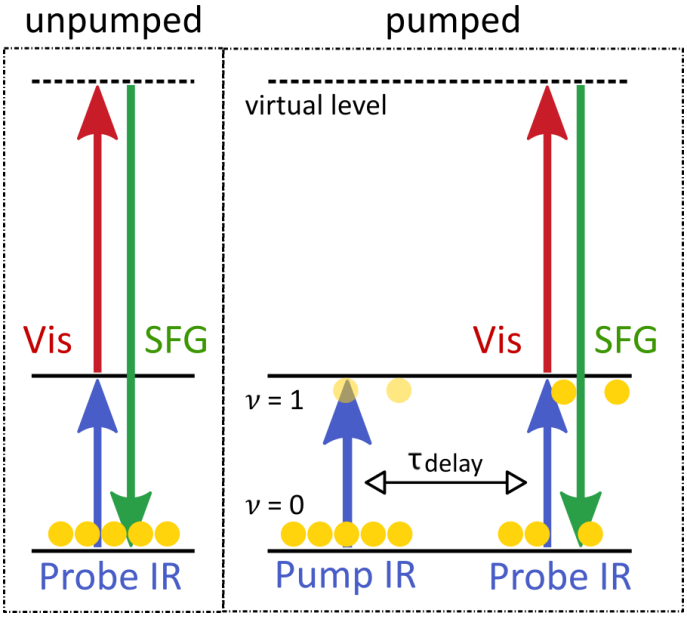

Figure 2.5: Excitation-level diagram for the pump-probe SFG process

Feynman diagrams for Pump-probe SFG

Pump-probe SFG being a 4th order technique, will have a fourth-order response that can be represented compactly as following:

$$R^{(4)}(t_4,t_3,t_2,t_1) \propto i\langle\mu(t_4+t_3+t_2 + t_1)\Big[\mu(t_3+t_2+t_1),\Big[\mu(t_2+t_1),\Big[\mu(t_1),[\mu(0),\rho(-\infty)]\Big]\Big]\Big]\rangle = i\,\langle\mu_4\Big[\mu_3,\Big[\mu_2,[\mu_1,[\mu_0,\rho(-\infty)]]\Big]\Big]\rangle \quad \text{Eq. 2.34}$$

Since the visible interaction with a non-resonant or virtual level is very short-lived (~1 fs) when compared to the IR response (hundreds of fs to ps), it can be approximated as δ-shaped in the time-domain[30]. Under this assumption, the integral over the Visible field collapses, and the expression for $P^{(4)}$ simplifies to an integral over the 3 IR fields. $P^{(4)}$ looks very similar then to $P^{(3)}$ except for the polarizability (α) that enters the equation.

$$R^{(4)}(t_4,t_3,t_2,t_1) = R^{(3)}(t_3,t_2,t_1).\delta(t_4)$$
$$P^{(4)}(t) \propto \left(\frac{i}{\hbar}\right)^4 \alpha E_{4,Vis}(t)\int_0^\infty dt_3\int_0^\infty dt_2\int_0^\infty dt_1$$
$$\mu_3E_3(t-t_3)\,\mu_2E_2(t-t_3-t_2)\,\mu_1E_1(t-t_3-t_2-t_1)\,R^{(3)}(t_3,t_2,t_1) \quad \text{Eq. 2.35}$$

The equation above for $P^{(4)}$ takes into account only the real-valued electric fields. Applying the RWA, particular Feynman diagrams are created by either $E(t) \propto e^{-i\omega t}$ or $E^*(t) \propto e^{+i\omega t}$ only for each of the three laser pulses, indicated by the directionality of the field interactions in the Feynman diagrams. The electric field also contains information on the wavevector and the phase, so the RWA selects not just the frequency $e^{-i\omega t}$ or $e^{+i\omega t}$, but also determines the phase and wavevector. These prefactors can be used to discriminate between the pathways, and select particular ones for detection. For the pump-probe experiments, the generated 4th order polarization is detected in exactly the same direction as the probe, i.e. k_{pr}. To fulfill the phase matching conditions, this geometry comes with the consequence that the pump pulse interacts twice[27] with the sample with wave vectors $+k_{pu}$ and $-k_{pu}$, from the same pump field, as illustrated in Figure 2.6.

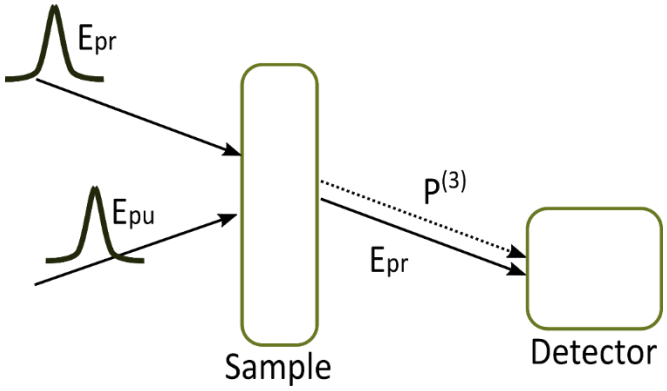

Fig 2.6: phase-matching condition for the pump-probe experiments, the outgoing field is generated in the same direction as the probe.

For a 3-level system, the 6 Feynman diagrams that survive the RWA and the aforementioned phase-matching condition, are displayed in Figure 2.6, assuming that the probe pulse interacts after the first two interactions of the pump.

Since the visible pulse is for upconversion purposes[31], the quantum state of the system is preserved, and the Feynman diagrams for the $P^{(3)}$ process, can be used, added with the visible field interaction towards the end.

The diagrams in Figure 2.7 represent the three processes to be taken into account in a pump-probe measurement. The following points are to be noted:

1. Diagrams on the top and bottom are different in just the ordering of the two pump interactions, but lead to the same response function.
2. Considering the diagrams at the top, at t=0, a ρ_{10} off-diagonal matrix element of the density matrix is generated for all 3 processes, with a probability proportional to transition dipole moment μ_{10}.

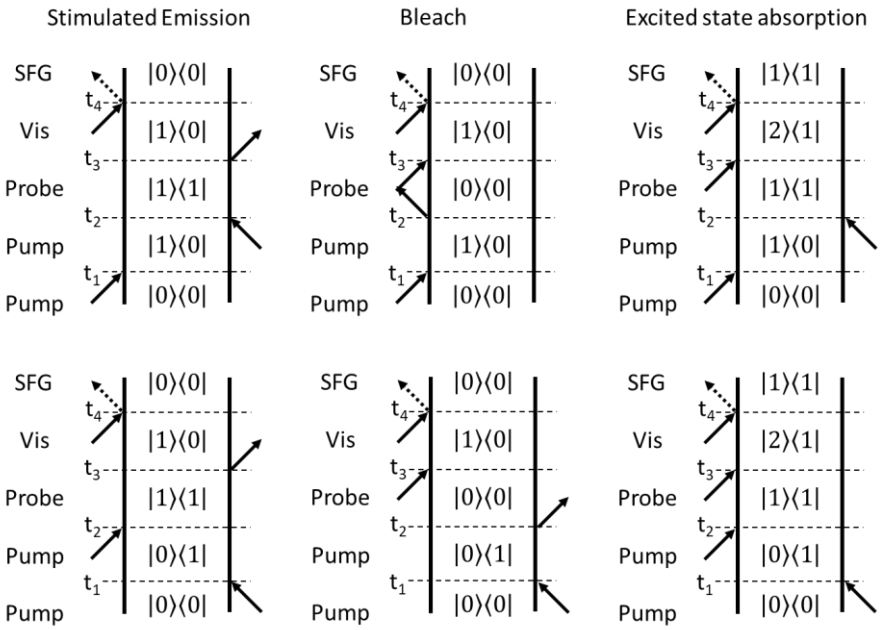

Figure 2.7: Feynman diagrams for the Pump-probe SFG process

3. Evolution of this off-diagonal element into relaxation or dephasing is neglected, so t1 is short considering the second interaction from the pump pulse almost takes place instantaneously. The second interaction generates a diagonal density matrix ρ_{11} for SE and ESA, with a probability proportional to μ_{10}^2. For the bleach process, the matrix element ρ_{00} is generated. However, since we assumed nothing happening during this time, the response for the GSB is the same as the SE diagram.
4. The diagonal elements of the density matrix stay constant in time, so $\rho_{11}(t2) \propto \mu_{10}^2$.
5. With the third interaction, ρ_{10} matrix element is generated again for the SE and GSB processes, which develops as a function of time t3: $\rho_{10}(t3) \propto \mu_{10}^3 e^{-i\omega(t3-t1)}$. For the ESA however, the third interaction generates a ρ_{21} coherence with probability μ_{21}.

6. The signs of the SE and GSE process are the same, due to an even number of interactions on the ket side, ESA is negative due to an odd number of interactions on the ket side.

The Feynman diagrams for a pump-probe experiment help elaborate easily three different processes taking place in a progressive step-by-step manner, which was not possible with the vibrational level diagrams. With this information, it is possible now to calculate the macroscopic polarizations of the $P^{(2)}$ and $P^{(4)}$ states.
$P^{(2)} = P^{(2)}_{unpumped} \propto -\mu_{01}\alpha_{01}E_{Vis}E_{IR}$, where μ_{01} is the transition dipole moment between vibrational ground state $|0\rangle$ and excited state $\langle 1|$; $\alpha_{01} = \mu_{Vis}\mu_{SFG}$ is a combined term describing the interaction of Vis and SFG, and is called the transition polarizability; and E_{Vis} and E_{IR} are the electric fields of the Visible and IR pulses. $P^{(4)}$ can be described as a summation of the 3 pump-probe polarizations and the static SFG polarization, as shown in the Feynman diagrams before:
$P^{(4)}_{pump} \propto P^{(4)}_{GSB} + P^{(4)}_{SE} + P^{(4)}_{ESA} + P^{(2)}_{unpumped}$

From the Feynman diagrams, it was shown that the polarization for the GSB and SE is the same, that is, $P^{(4)}_{GSB} = P^{(4)}_{SE} \propto \mu_{01}^2 E_{pump}^2 \mu_{01}\alpha_{01}E_{Vis}E_{IR}$, where $\mu_{01}^2 E_{pump}^2$ is due to the two pump interactions.
For ESA: $P^{(4)}_{ESA} \propto \mu_{01}^2 E_{pump}^2 \mu_{12}\alpha_{12}E_{Vis}E_{IR}$, where μ_{12} and α_{12} are the IR transition dipole moment and the electronic transition polarizability, respectively, for the transition between states 1 and 2.
Due to anharmonicity, the sum of the pump-probe processes does not actually cancel out (because $\mu_{12} = \sqrt{2}\mu_{01}$ and the same for the transition polarizability), but just causes a shift in frequency of the ESA to the red side.

To evaluate intensities, the $P^{(2)}_{unpumped}$ and the $P^{(4)}_{pump}$ are squared; the $\left|P^{(4)}_{pump}\right|^2$ term upon expansion leads to many cross-terms and four square terms. The anharmonicity is used again here to simplify the $I_{SFG,pump}$, as all cross-terms containing transitions 0-1 and 1-2 are assumed to be zero because of their separation in frequency. Also $P^{(4)}_{ESA}P^{(2)}_{unpumped} = 0$, and the difference in signal intensity with the pump on and pump off can be written as:
$\Delta I_{SFG} = I_{SFG,pump} - I_{SFG,unpumped}$:

$$\Delta I_{SFG} \propto \left|P^{(4)}_{ESA}\right|^2 + 4\left|P^{(4)}_{GSB}\right|^2 + 4P^{(4)}_{GSB}P^{(2)}_{unpumped}$$

The ratio between GSB+SE and ESA is 9:1, and thus peaks corresponding to decrease of the 0-1 transition dominate the intensity spectrum[32]. ΔI_{SFG} is the differential SFG signal; for the analysis $Ratio_{SFG}$ is also used for a normalized SFG signal by: $I_{SFG,pump}/I_{SFG,unpumped}$.

Analysis of Pump-probe measurements

For the pump-probe measurement, an SFG signal is detected individually for the unpumped and the pumped states, for different time-delay points, along with background signals at each time point. The setup is described in chapter 3. The spectra are background-subtracted, and $Ratio_{SFG}$ is obtained at each time-point by dividing the unpumped spectrum by the pumped spectrum. The $Ratio_{SFG}$ spectra can be plotted as a function of time, to obtain contour plots, to observe changes in the SFG intensity as a function of time and frequency. An example of such a contour plot is shown below, with a variation of colors representing negative or positive changes in the intensity.

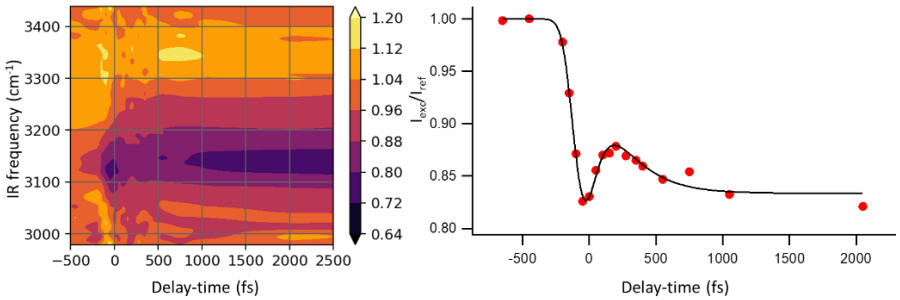

Figure 2.8: a) contour plot for ice pumped at 3050 cm^{-1}; b) an example of a Ground State Bleach (GSB) trace obtained by integrating specific spectral regions from plot a. The 'bleach' process in the trace displayed here is represented by the sharp decrease in the intensity ratio around time zero.

From such contour plots, different frequency regions can be picked for intensity integration to obtain 'traces' representing the processes of GSB (plus SE), and ESA, as described above. The obtained traces (example shown in Figure 2.8b) are fitted using a 4-level model, describing populations in different states. This is a model typically used for fitting dynamics of aqueous systems[33].

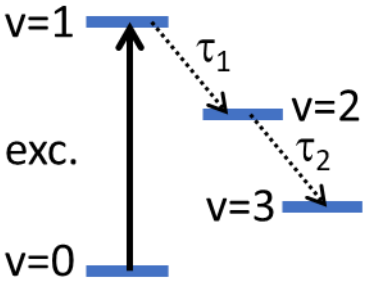

Figure 2.9: 4-level model typically used for water in a pump-probe experiment

The pump pulse excites a fraction of oscillators from the ground state v=0 to the excited state v=1. The excited molecules stay in state v=1 for an average lifetime of τ_1 and decay via an intermediate state v=2 to the heated ground state v=3. The absorption of the highly intense pump beam causes the temperature of the system to change, and a heated ground state is accounted for as the temperature cools down at a much slower rate than the experiment resolution. The model can be described by a system of coupled first-order linear differential equations as described below, where N is the total number of oscillators and $N_i(t)$ denotes the corresponding number of oscillators in state i at time t.

$$N_0(t) = N - N_1(t) - N_2(t) - N_3(t)$$

$$\frac{dN_1(t)}{dt} = S(t) - N_1(t)/\tau_1$$

$$\frac{dN_2(t)}{dt} = \frac{N_1(t)}{\tau_1} - N_2(t)/\tau_2$$

$$\frac{dN_3(t)}{dt} = N_2(t)/\tau_2$$

The source term $S(t)$ is represented by a Gaussian function, with a temporal width equalling that of the instrument response function. The instrument response is obtained by performing a cross-correlation scan by recording the integrated intensity of the pump-probe-visible signal as a function of delay-points between the pump and the probe. The width of the obtained spectrum is used to estimate for the instrument response function, and describes the temporal width of the system. This is because the pulse duration of the individual pulses is complicated to measure, and of interest is the time dependency of the convolution of the pump pulse with the SFG signal.

Chapter 3

Generation of ultrashort high-intensity pulses

Vibrational dynamics influence molecular reactions and occur on a timescale of a few femtoseconds to picoseconds. To resolve such ultrafast dynamics, a probing methodology of a similar time resolution, if not shorter, is required. It took only two decades after the laser was invented for the duration of light pulses to shrink down by six orders of magnitude, from nanosecond to the femtosecond regime. So far, the shortest light pulse being generated is a mere 80 attoseconds. To put things into perspective, light only travels 300 nanometers in 1 femtosecond.

Laser basics

Stimulated emission

Einstein postulated that three different processes can take place when light interacts with matter (figure 3.1): Absorption – a photon with a radiation field transfers its energy to an electron, which transfers its state from E_m to E_n, with the probability B_{mn}; Spontaneous emission – From the excited state E_n, an electron with a probability A_{nm}, spontaneously falls to the lower state E_m, with simultaneous emission of a photon with energy $h\nu = E_n - E_m$, with a random direction, phase and polarization; and Stimulated emission – wherein a photon with energy $h\nu$ passes by an excited atom causing a stimulated emission of a twin photon, with the same energy, phase, polarization state, and direction of propagation, with the probability B_{mn}.

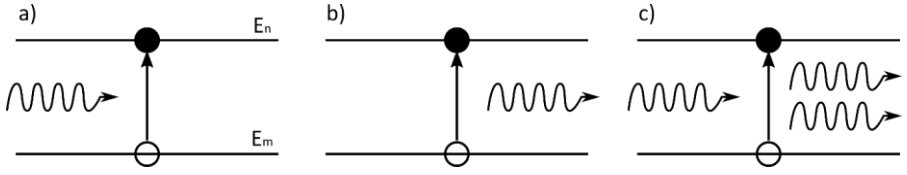

Figure 3.1: elementary electron-photon interaction processes in atoms: a) absorption, b) spontaneous emission, c) stimulated emission

Stimulated emission is the working principle of lasers: the key idea being light amplification by creating a population inversion, that is, having more atoms in the excited states than in the ground state. This can be done via optical pumping, wherein a material with natural electronic states with 3 or more levels (figure 3.2) is able to sustain population inversion when energy is given to it. In such a material, state 2 acts as a metastable state, and the radiative transition of interest is from 2 to 1. Population inversion is achieved when a) the pumping rate from level 1 to 3 is large enough to overcome the spontaneous emission from state 2 to 1, b) the electronic decay from state 3 to 2, that is the pumping to the radiative state is the fastest in the system, c) the radiative decay time is long enough to ensure that the intermediate metastable state is substantially over occupied.

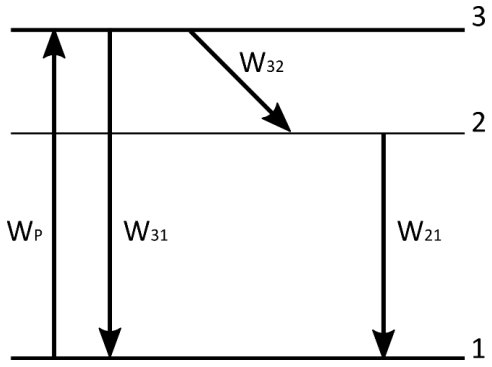

Figure 3.2: three-level system to illustrate population inversion

Intensity dependence of Amplification

Upon establishment of population inversion in a medium, light can be amplified. The following equation[34] describes light amplification in an inverted population system for an EM wave propagating along the *z*-direction:

$$\frac{dI(z)}{dz} = -I(z)\,\Delta N\,\sigma_{21} \qquad \text{Eq. 3.1}$$

where σ_{21} is the stimulated emission cross-section of the transition, and depends on both the medium and the wavelength of the light, and ΔN is the population inversion. The intensity dependence of the population inversion of an efficient gain medium can be formulated as below:

$$\Delta N \approx -N \,/\, (1 + \frac{I(z)}{I_s}) \qquad \text{Eq. 3.2}$$

where I_s is a constant intensity depending on the gain medium. When equation 3.2 is substituted into equation 3.1, we get:

$$\frac{1}{I(z)}\frac{dI(z)}{dz} = g_0/(1 + \frac{I(z)}{I_s}) \qquad \text{Eq. 3.3}$$

where $g_0 = N\sigma_{21} > 0$ is the low-intensity gain. The saturation intensity I_s allows one to distinguish between the low- and high-intensity regimes for light amplification in a gain medium. When $I(z) \ll I_s$, the intensity grows exponentially along the propagation direction, and the amplification process is said to be very efficient. For $I(z) \gg I_s$, the intensity grows as a linear function, the amplification process is much less efficient, and the gain is said to saturate in the high-intensity regime. In the high-intensity regime, the gain saturation follows a hyperbolic model which is very similar to how saturable absorbers work, for important applications like pulse shortening.

Most of the gain media, that is, the media used with electronic structures that facilitate population inversion, are formed into a geometrical shape such that one of their dimensions is larger than the others. This reduces the unwanted amplified spontaneous emission which takes place in laser amplifiers. To reduce such unwanted signal, amplifier decoupling is also done, using Faraday polarizers or saturable absorbers that use the principle of gain saturation.

Longitudinal modes

An oscillator is the association of an amplifier with a positive feedback loop. To produce short pulses using lasers, the most essential property of optical resonators is that the resonator supports longitudinal modes. Transverse modes (not considered here in detail) are a geometric consequence of light propagation; longitudinal modes are a time-frequency property. An electromagnetic (EM) field can be established between two parallel mirrors only when a wave propagating in one direction can interfere constructively with the wave propagating in the reverse direction. The resulting superposed wave is a standing wave, which is established if the distance L between the two mirrors is an integer-multiple of the half-wavelength of the light. τ being the period of the wave, and c the speed of light, and thus $\lambda = \tau c$, the standing wave condition is:

$$\frac{mc\tau}{2} = L, \qquad m \in N^+ \qquad \text{Eq. 3.4}$$

which fixes the value of m. The cavity has a specific period T = mτ, which is also a round-trip time of flight T = 2L/c. These numbers fix the repetition rate of mode-locked lasers and also the period of the pulse train. For a typical laser cavity, L = 1 m, the period is 6.6 ns, and the characteristic frequency Δν = c/2L = 150 MHz. This frequency gives the spacing between the different modes of the laser cavity, and m gives the number of modes. The resonant modes of the cavity are considerably narrower in frequency than the bandwidth of the normal spontaneous atomic transition. For example, a ruby laser radiating at 694.3 nm, 0.53 nm wide, has a bandwidth of 300 GHz, compared to the 150 MHz spacing between different modes for the laser cavity.

In a continuous wave (CW) regime, the amplification process of the laser is basically coherent and linear.

Generation of ultrashort pulses

Mode-locking

A laser in a free-running regime has its longitudinal (and transverse) modes in a random phase relationship with each other. The interference of all these modes with no defined phase relations in time, produces a

chaotic sequence of fluctuations, giving a time-averaged statistical mean output value (figure 3.3a). Suppose, however, the different longitudinal modes of the laser are somehow made to have a fixed phase relationship to each other. In that case, this mode-locked condition produces periodic repetitions of a wave-packet resulting from the constructive interference of the longitudinal modes (figure 3.3b). Mode-locking, hence has the outcome of a train of pulses having a repetition period T, which is the round-trip time in the optical resonator, T = 2L/c. The temporal duration of the pulse t_p, equals the round-trip time T divided by N, the total number of phase-locked modes[35].

The duration of the pulse is dependent on the number of longitudinal modes N; the longitudinal mode in turn depends on the laser gain bandwidth δλ by: $N = 4L\delta\lambda / \lambda_0^2$. Hence, the greater the number of longitudinal modes (depending on the cavity length) involved in a broader spectral transition (depending on the gain or lasing medium), the shorter is the mode-locked pulse[35]. The titanium-sapphire (Ti-Saph) laser is a vibronic solid-state laser wherein the coupling between the vibrational and electronic states leads to a considerable spectral band broadening, making it possible to generate femtosecond pulses.

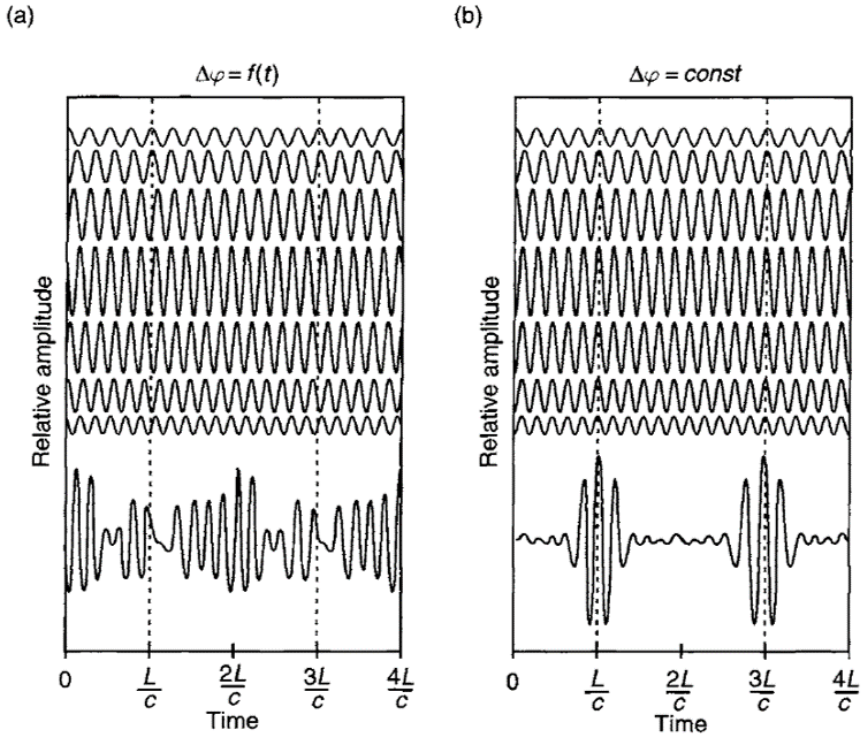

Figure 3.3: electric field as a function of time representing different modes in a) a free-running laser in multimode regime; b) a mode-locked laser; Figure from reference[23].

The total electric field from the longitudinal modes N can be represented by:

$$E = E_0 \exp(i\omega_0 t) \frac{sin\frac{N(\Delta\omega_q t + \Delta\varphi_q)}{2}}{sin\frac{(\Delta\omega_q t + \Delta\varphi_q)}{2}} \quad \text{Eq. 3.5}$$

where $\Delta\omega_q \; and \; \Delta\varphi_q$ are the frequency difference and the phase difference, respectively, between the neighboring longitudinal modes. If $\Delta\varphi_q$ changes randomly, then the E changes chaotically. If $\Delta\varphi_q$ between modes is constant, then E has its total intensity as an amplitude-modulated wave at a carrier frequency ω_0, equal to the central mode with the envelope expressed in the form

$$A(t) = E_0 \frac{sinN(\Delta\omega_q t + \Delta\varphi_q)/2}{sin(\Delta\omega_q t + \Delta\varphi_q)/2} \quad \text{Eq. 3.6}$$

The intensity, given by $I(t) = A^2(t)$ is a function of type $(\frac{\sin nx}{\sin x})^2$, which is well known from diffraction theory. Since it is a periodic function, it shows that the radiation intensity generated from synchronized longitudinal modes is a repetition of pulses, periodic in time.

The pulse bandwidth and the pulse duration are tied together by the Heisenberg uncertainty principle: $\Delta t \; \Delta E \; \geq h/2\pi$ and the magnitude of the equation is given by the pulse shape. For a Gaussian pulse shape, the product is equal to 0.441. This is an ideal situation, and such a pulse is also called a Fourier-transform limited pulse.

Methods of Mode-locking

As addressed before, a laser only would generate high-power short-duration pulses when the different frequency modes are phase-locked. This can be achieved via active, passive, and self-phase modulation methods. Active mode-locking includes using acousto-optic devices that produce a sound wave modulating laser beam's intensity; or electro-optical modulators that are driven at exactly the frequency-separation of the modes. An active mode-locking mechanism involves modulating the longitudinal mode frequency ω_0, with a modulation frequency Ω which causes additional radiation at the frequency component $\omega_0 + \Omega$. When this additional component is equal to frequency-separation $\Delta\omega_q$ of the longitudinal modes, the additional components overlap with the neighboring modes and induce coupling, stimulating oscillations in the same phase[35]. An example of an acousto-optic device is a piezoelectric transducer. A Pockels cell is an example of an electro-optic device. Pockels cells are used in Ti-Saph amplifiers to retain high peak power pulses for Chirped Pulse Amplification (CPA).

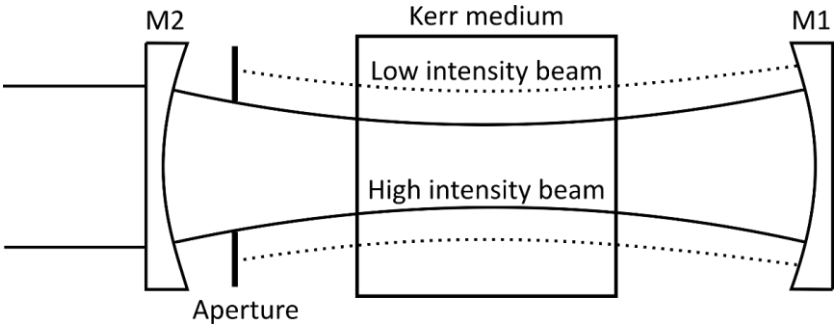

Figure 3.4: Illustration depicting the Kerr lens modulation

Passive mode-locking involves using saturable absorbers that modulate the amplification factor of an active medium. Using saturable dyes is an example, wherein at first, there is linear amplification and linear dye absorption, followed by non-linear absorption of the dye, and then finally non-linear amplification leading to bleaching of the dye. This method can only be applied when the dye has a lifetime comparable to the duration of modelocked pulses. For shorter, femtosecond pulses, a faster 'shutter' is needed, and has been replaced by Kerr Lens Modelocking or other passive methods like saturable Bragg reflectors.

The Kerr Lens Modelocking (KLM) is based on the Kerr effect. For high intensities, the refractive index becomes a function of the light intensity I by

$$n = n_0 + n_2 I \qquad \text{Eq. 3.7}$$

This is known as the Kerr effect, and it indicates an intensity-dependent variation of the laser beam profile, if that profile is different from a top-hat profile. For a Gaussian beam, the index modification of the beam is higher in the center, when seen along the x-axis as the beam propagates in the z-direction, than in the wings. This corresponds to inserting an additional lens of a Gaussian shape into the medium, thereby introducing a self-focussing effect. KLM requires no active or passive elements to mode-lock. Many solid-state lasers employ the KLM phenomenon combined with a hard aperture, to modulate the amplitude of the resonator modes, having a frequency determined by the round-trip time doubled. The refractive index 'lens' formed in the center of the beam leads to beam focusing, and the placement of an aperture in the resonator works as a selective shutter. Thereby, the edges of the continuous-wave beam incur more loss, while the centre is focussed even more. Thus the central part of the laser gain is monopolized with every new round-trip of this loss-amplification process, leading to amplitude modulation. This is called self-mode locking because the Kerr Lens medium can be the laser crystal itself. This is a heavily used method for Ti-Saph oscillators to produce stable and highly reliable femtosecond pulses.

Amplification of pulses

The amplification, done using the Chirped Pulse Amplification (CPA) process, involves first stretching the seed pulse in time using dispersive elements like a grating pair, to reduce the peak power and avoid destruction of the gain medium. The pulse is then amplified in the gain medium either by regenerative amplification or by a multipass amplifier, subsequently followed by compression in time.

In a regenerative amplifier, the gain medium is pumped to accumulate energy. An electro-optic switch is then used to inject the initial pulse into the resonator, which is opened only for a short time, shorter than the round-trip time of the oscillator. A Pockels cell in combination with a broad-band polarizer can be used as an electro-optic switch for trapping and letting the pulse in and out of the resonator. Pockels cell is a birefringent crystal that can change the polarization of a traveling laser field when high voltage is applied to it. Usually in a regenerative amplifier, two Pockels cells are employed, the first one in combination with a quarter wave plate. Voltage applied to switch the first Pockels cell into a quarter waveplate leads to $4*\lambda/4 = \lambda$, therefore no change in polarization of the light, and the pulse stays inside the resonator until it reaches saturation. To release the pulse, the voltage to get $\lambda/4$ polarization is applied to the second Pockels cell, to have an overall $2*\lambda/4 = \lambda/2$ effect which changes the polarization state of the beam, which is subsequently reflected off a thin-layer polarizer[36].

The basic difference between a multi-pass and a regenerative amplifier, is how the input and output pulses are distinguished. In a multipass amplifier, it is done geometrically, whereas polarization is used in the case of a regenerative amplifier.

After amplification, the amplified pulse is recompressed to its initial duration. Besides the dispersion of the stretcher, the compressor must also compensate for the dispersion introduced by the amplifier. This can be done by setting the gratings used to recompress at a larger distance than what was used between the gratings when stretching the pulse. More details on dispersion of a propagating pulse will be presented below.

Pulse Propagation

Figure 3.5 is a depiction of a mode-locked pulse train out of a femtosecond laser system. In red is represented the oscillatory electric field, with the oscillatory period ~2.7 fs for 800 nm wavelength, leading to very few oscillations present for a 25 fs pulse. For such short pulses, usually, the intensity is more convenient for describing the pulse properties. The amplitude is defined by the wave envelope, represented in black in the figure, and the intensity by the square[37].

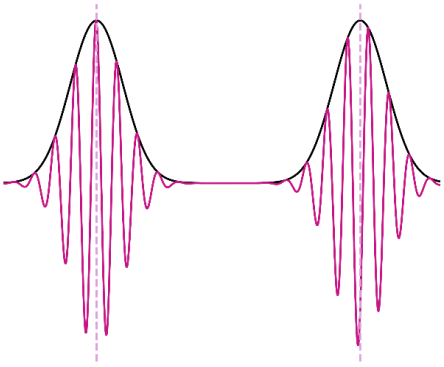

Figure 3.5: mode-locked pulse train; dashed lines represent change in phase of the pulses

The amplitude envelope is defined as $A(t) \propto e^{-\Gamma t^2}$ with the slowly-varying envelope approximation, where $\Gamma \equiv \Gamma_1 - i\Gamma_2$ is a complex function, with its real part related to the pulse duration $\tau_p = \sqrt{\frac{2ln2}{\Gamma_1}}$, and its imaginary part describing the time-dependence of frequency, $\omega(t) = \frac{d\phi_{tot}(t)}{dt} = \omega_0 + 2\Gamma_2 t$, therefore accounting for 'chirp.'

In a dispersive medium, as $\phi(\omega) = k\, n(\omega)\, L$, where L is the length of the dispersive medium, the pulse acquires a frequency-dependent phase-shift. The phase shift can be expanded using the Taylor series around the central angular frequency ω_0:

$$\phi(\omega) = \phi_0 + \frac{\partial \phi}{\partial \omega}(\omega - \omega_0) + \frac{1}{2}\frac{\partial^2 \phi}{\partial \omega^2}(\omega - \omega_0)^2 + \frac{1}{6}\frac{\partial^3}{\partial \omega^3}(\omega - \omega_0)^3 + \cdots \qquad \text{Eq. 3.8}$$

where ϕ_0 is the absolute phase of the pulse, the first derivative of ϕ changing linearly with ω is the group delay without any change in the temporal shape of the pulse. The higher-order phase shifts modify the shape of the pulse, the second-order derivative corresponds to Group Delay Dispersion or GDD, and the Third Order Dispersion (TOD) becomes increasingly important the shorter the pulse duration gets.

The GDD describes a linear frequency dependence of the group delay, $\frac{\partial(\partial\phi/\partial\omega)}{\partial\omega}$, and separates the frequency components of the pulse. A positive GDD corresponds to the components at higher frequencies being delayed with respect to the components at lower frequencies, creating a positive chirp, where red precedes the blue in time. A negative chirp is when blue recedes the red in time. Figure 3.6 depicts an unchirped, and a positively and negatively chirped Gaussian pulse.

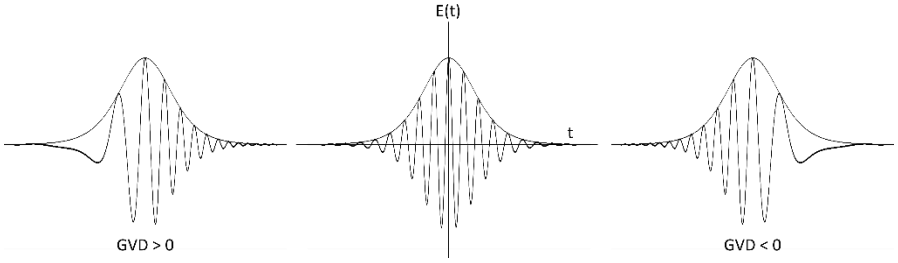

Figure 3.6: Gaussian pulse with a) positive chirp; b) zero chirp, perfect mode-locking; c) negative chirp; figure adapted[38].

Experimental laser setup

A Ti-Saph oscillator (Mai Tai, Spectra Physics), pumped by a frequency-doubled Nd:YAG, generates laser pulses of 30 femtoseconds, with a pulse rate of about 80 MHz, at a central wavelength of 800 nm and 60 nm bandwidth. The output pulse from the Ti-Saph oscillator is stretched in time and used as a seed laser for the Ti-Saph regenerative amplifier (Spitfire Ace), which is pumped by a frequency-doubled Nd:YLF. The amplified pulses are compressed using a pair of gratings or prisms. Ultrashort high-intensity pulses with a pulse energy of 5 mJ and an average power of 5 W, at a pulse rate of 1 kHz, and a pulse duration of 40 fs are generated.

The pulsed visible beam generated from the Ti-saph amplifier is expanded in beam diameter, and divided into 4 parts. Roughly 1 of the 5 W is sent to an etalon, where the spectral bandwidth is reduced from typically 55 nm to ~1 nm. Additionally, in the path of the visible beam to the sample, a combination of a half-wave plate and a polarizer are used for polarization filtering, and an additional half-wave plate is added to reduce power for sensitive samples like the ice surface or lipid monolayers.

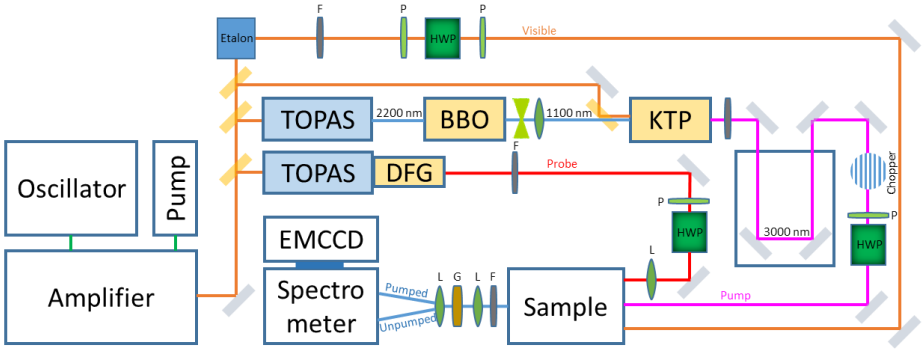

Figure 3.7: Pump-probe SFG setup: P: polarizer; F: filter; L: lens; HWP: half-waveplate; G: galvanometer

The second and third parts of the laser output, (roughly 1 W) are sent to an Optical Parametric Amplifier (TOPAS-C) each for generation of short to mid-wavelength infrared pulses using non-linear parametric generation processes. The first OPA generates IR light tunable in frequency, typically around 3300 cm^{-1} (3030 nm), with a pulse energy of ~10 µJ, used for time-averaged SFG experiments, and called the probe-IR in the pump-probe SFG experiment. To generate the Pump IR beam, the idler output (~2000 nm) from the second OPA is frequency-doubled using a BBO crystal, and this ~1000 nm output is overlapped with the last 4^{th} part of the laser output in a KTP crystal, to undergo a Difference Frequency Generation (DFG) process, producing an intense IR beam tunable in the 3000 to 3700 cm^{-1} range. A brief working mechanism of the OPA is described below.

General OPA mechanism

The principle of an OPA is based on a DFG process, in a non-linear crystal, a high-intensity high-frequency beam (pump beam, ω_3) amplifies a lower-frequency seed beam (signal beam, ω_2), also additionally generating a lower-frequency third beam (idler, ω_1). During the process, both energy and momentum conservation is fulfilled; energy conservation determines the resulting frequencies, and momentum conservation leads to phase-matching determining the direction of the beam[39].

A small part of the pump beam (can be 800 nm - the fundamental frequency, or 400 nm – the second harmonic of the Ti-Saph laser) is used to generate the seed beam via a process called the supercontinuum white light generation, wherein the pump beam is focussed into a thin (1-2 mm) sapphire plate. The pulse undergoes self-phase modulation (SPM) due to high intensity-dependent refractive index changes, and other

effects like spatial and temporal focussing, there is a change in the carrier frequency on both the leading and trailing edges of the pulse, leading to broadening of the spectrum.

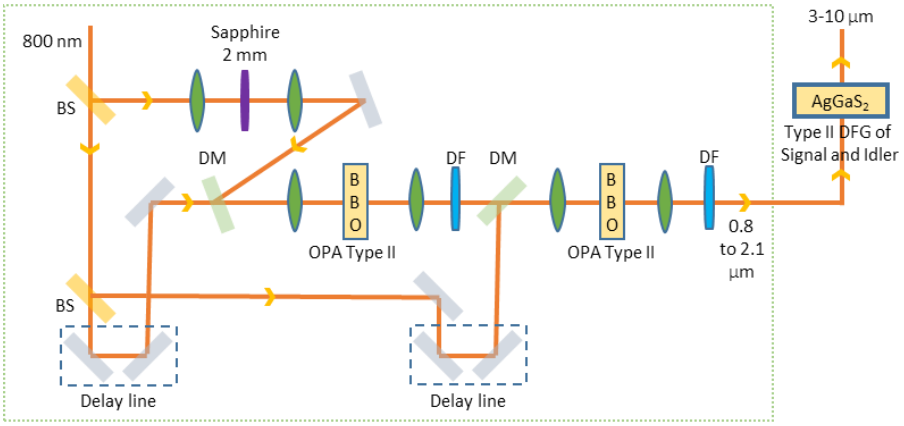

Figure 3.8: Working principle of a near-IR OPA setup to generate near-IR wavelengths in dashed green box; DF: dichroic filter, DM: dichroic mirror, BS: beam splitter. Figure adapted[40]. Further DFG process to produce mid-IR wavelength beams.

Following the seed generation, the pump and the seed pulses undergo amplification in two stages, via spatial and temporal overlapping in a non-linear crystal, by the non-linear parametric amplification process, where the pump beam (ω_3), amplifies the lower frequency signal beam (ω_2), also additionally producing a lower frequency idler beam (ω_1). The first amplification stage is used to compensate for the group velocity mismatches between the pump and signal pulses using a delay line. The second amplification stage, called the power stage, causes significant pump depletion with a conversion efficiency above 30%. The second stage is able to produce much more stable pulses as the seed fluctuations are minor after the first amplification. After the second amplification process, the signal and idler beams are separated from the pump beam using dichroic mirrors or filters.

The signal and idler produced in the near-IR region are subsequently separated using dichroic mirrors to induce time-delay changes, and go through a Type II DFG process in an $AgGaS_2$ crystal to produce pulses in the mid-IR frequency range. The whole process is depicted in Figure 3.8.

Chapter 4

Interfacial Vibrational Spectroscopy of the Water Bending Mode on Ice Ih

This chapter is adapted with permission from the published manuscript in the Journal of Physical Chemistry C, 2021, with the assigned DOI: https://doi.org/10.1021/acs.jpcc.1c08046

ABSTRACT: We study the molecular-level properties of the single-crystal ice Ih surface using interface-specific Sum Frequency Generation spectroscopy. We probe the water vibrational bend region around 1650 cm^{-1} of the basal plane of hexagonal ice, to understand the interfacial structure from vibrational properties. As opposed to the stretch mode of ice, the bend mode response depends very weakly on temperature. The large linewidth of the bending mode response, relative to the response on water, is inconsistent with inhomogeneous broadening, and points to ultrafast pure dephasing. The bend mode of ice provides an excellent means to study adsorbate-ice interactions and understand differences in ice and water reactivity.

Introduction

The water-air and ice-air interfaces act as actives sites for chemical reactions in both natural and engineering settings. Water molecules at the surface are different from those in bulk, owing to the truncation of the hydrogen bond network. The properties of interfacial water molecules have been extensively studied owing to relevance in atmospheric[41,42], biological[43], electrochemical[44,45], and geological sciences[46]. Ice interfaces have raised particular scientific interest owing to their reported high catalytic activity[47,48], and implications in frost heave, supraglacial chemistry[49], and exchange of trace gases establishing atmospheric concentrations of species[50]. Information on the molecular properties of specifically the interface can be obtained with surface-specific vibrational spectroscopic methods, such as Sum Frequency Generation (SFG) spectroscopy[24,51]. As a second-order nonlinear technique, SFG is inherently interface-specific owing to its selection rule that inversion symmetry must be broken for the signal to be generated. In this method, two laser beams, an infrared beam in resonance with a vibrational transition, and a visible beam for upconversion

are overlapped in space and time. An SFG signal is generated at the sum of the frequencies of the two incoming laser beams. When the infrared beam is vibrationally resonant with surface molecules, the signal is enhanced. The SFG intensity as a function of infrared frequency thus provides the vibrational spectrum of specifically the interfacial molecules.

SFG research has traditionally focused on the ~3300 cm^{-1} OH stretch mode of water in the study of interfacial properties of aqueous systems. The stretch mode frequency is correlated to hydrogen bond strength[52,53], allowing access to molecular structure information from spectroscopic observables. The stretch-mode region of water gives a relatively high intensity compared to other vibrational modes, simplifying signal detection. Despite the clear advantages, water vibrational stretch mode spectra can be challenging to interpret due to the strong effects of inter- and intra-molecular couplings on the spectral lineshape[54]. This coupling causes delocalization of vibrational OH stretch quanta, affecting the vibrational response. Further complications appear in the presence of other moieties with OH groups due to interference of the vibrational OH-stretch of water with that of alcohols, other biomolecules, etc. The HOH bend mode of water can act as an insightful alternative to the stretch mode: as it avoids such complications. The weaker inter-molecular coupling for the bend mode and the correlation of the bend mode frequency to the hydrogen-bonding strength can complement the stretch mode results[55,56]. Due to its smaller transition dipole moment, the bend mode is expected to be less influenced by intermolecular dipole-dipole coupling, which was recently experimentally verified for water interfaces[57]. Furthermore, the bend mode of water is spectrally separate from the C-O-H and C-N-H bending modes of alcohols and biomolecules, making such composite systems simpler to study. The vibrational bend region has thus recently gained interest to obtain molecular information of both bulk and interfacial systems.

The first SFG measurements of the vibrational bend mode of interfacial water, at ~1650 cm^{-1}, dates back to 2012[58], but has not yet been reported for ice. Previous theoretical work has shown that, for ice, the total dipole moment is reduced due to anti-correlated effects of permanent and induced dipole moments, indicating it is more challenging to determine the bending mode response from the surface of ice than of water [59,60]. Nevertheless, the bend mode region of interfacial ice is of fundamental importance, as its lineshape may provide information on the low-frequency excitations and bend-libration coupling mechanisms[61] at interfaces, and on the bending overtone, which determines the rate of vibrational energy relaxation[62]. As the bending mode is expected to be a more 'local' probe than the stretch mode, it can be important for studies of adsorbate-based systems on the surface of ice, allowing to observe spectral changes without intermolecular coupling effects[59].

Results and Discussion

Here, we report vibrational bend mode spectra of the basal plane of interfacial ice Ih, measured using SFG spectroscopy. Figure 4.1 a and b show SFG spectra of ice in the vibrational stretch and bend mode regions, respectively, at comparable temperatures in the SSP polarization combination (S-polarized SFG, S-polarized visible, and P-polarized infrared). The stretch mode spectrum is dominated by a signal at roughly 3200 cm^{-1} assigned to O-H modes hydrogen-bonded to neighbours. The signal at 3700 cm^{-1} originates from so-called free OH groups, while the 3500 cm^{-1} could be mainly attributed to the asymmetric stretch mode of fully coordinated water molecules[63] .

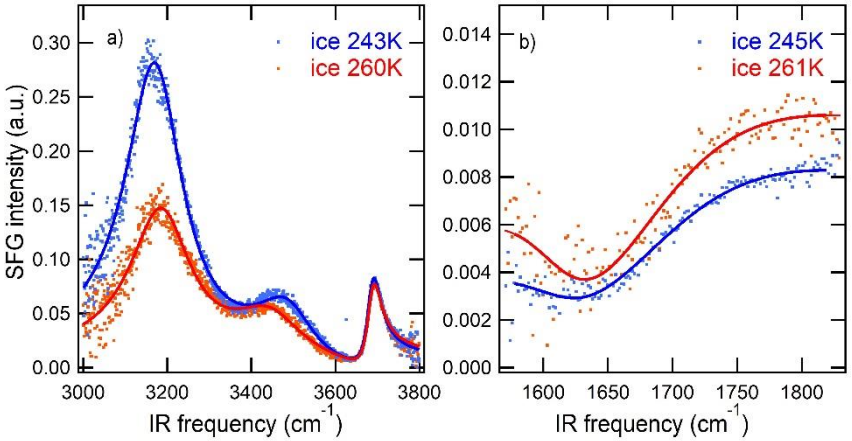

Figure 4.1: Experimental SFG measurements (dots) and fits (solid lines) in the vibrational stretch (a) and (b) bend mode region recorded from the surface of ice at two different temperatures, both measured using SSP polarization combination. The intensity axes in the left and right panels can be directly compared, indicating that the bend mode intensity is at least an order of magnitude smaller than that of the stretch mode.

As apparent from figure 4.1a, the ice surface exhibits a strong temperature-dependence in the OH-stretch region, with a ~100% intensity increase for a ~7% temperature decrease from 260 to 243 K. A straightforward explanation for this signal increase would be the enhanced orientation of interfacial water molecules at lower temperatures. However, MD simulations, shown in Figure 4.2, reveal that the orientational ordering of water molecules in the top two bilayers on the surface of ice can only account for a ~10% increase in the SFG intensity over this limited temperature interval. Thus, the major change in the stretching mode intensity for interfacial ice is attributed to temperature-dependent intermolecular coupling in the stretch region[64].

In contrast, Figure 4.1b shows no indication of a similar intensity increase for the interfacial ice bend mode region upon lowering the temperature, in line with the notion that bending modes are weakly coupled. The response in the bend region is, however, less straightforward than in the stretch region. For the stretch region, several clear peaks can be identified. In contrast, the bend mode response appears derivative-like, due to a relatively sizeable non-resonant contribution to the overall signal, as apparent from the high baseline relative to the signal size.

Figure 4.1a reveals a redshift of the stretch mode upon a decrease in temperature, as reported before[65]. A redshift in the stretch mode region is associated with stronger hydrogen bonding. Conversely, stronger hydrogen bonding is reflected by a blueshift of the bend mode frequency, as first shown by Falk[66]. For the given temperature interval, the ~15 cm^{-1} redshift of the low-frequency peak of ice in the stretch region translates to a negligible frequency shift in the bending region, as per the empirically inferred relationship[67] between the frequencies of the two modes. Indeed, no shift is apparent from the data in Figure 4.1b. Having established that the bend mode is less affected by intermolecular coupling, we further analyze the bending mode response at the ice interface, and compare it with the response of water. The polarizations of the incoming visible beam and the SFG beam were varied to generate signals in SSP and PPP polarization combinations. The three letters indicate the polarization of the SFG, Visible, and IR beams, respectively.

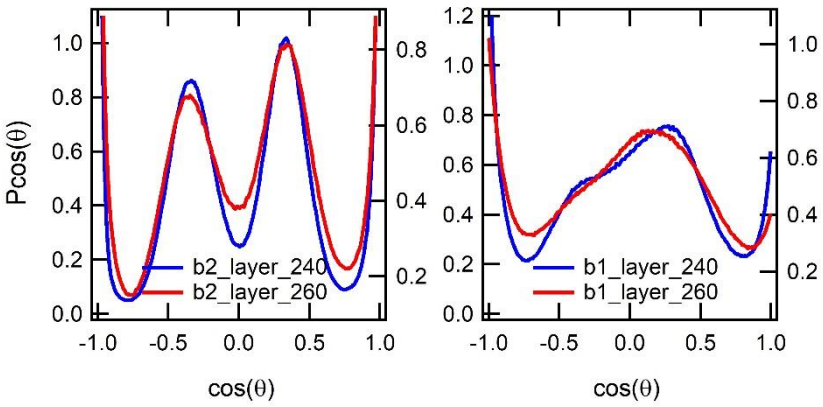

Figure 4.2: Probability distributions of water molecules with the OH-group pointing up (cosθ=0.3) and with the OH pointing down (cosθ=-0.3) for the top two bilayers on the surface of basal ice Ih. The figures are obtained from MD simulations, from the work of Sanchez et al[9]. Both the bilayers show certain asymmetry between the peaks representing the up and down pointing OH groups, which eventually leads to generation of an SFG signal. To elucidate the contribution of orientational ordering of water molecules to the increasing SFG intensity upon lowering the temperature in the stretch region, we evaluate the difference in probability distribution of the water molecules at the two temperatures. We integrated the Probability*cosθ within the range of -0.5 to 0.5 for both bilayers and compared the difference at the temperatures 240 and 260 K. We find an increase of 5.7% in the value for 240 K compared to 260 K, meaning an intensity increase to be $(1.057)^2$ = 11%. Thus we expect that the ordering of water molecules would lead to an intensity increase of roughly 10% upon lowering the temperature from 260 to 240 K.

The bend mode of interfacial ice compared to water

Figures 4.3 a and b represent the bend mode SFG intensity obtained from the interfaces of ice and water for the polarization combinations SSP (left column) and PPP (right column) as a function of the IR frequency. From the raw data, it is apparent that the bending mode response of ice is blueshifted and substantially broadened compared to water.

Both effects are qualitatively also present in the bulk infrared response (Figure 4.3e), but the blueshift is more pronounced at the interface. Perhaps remarkably, the SFG intensity for ice and water in the bend mode region is comparable. This observation is remarkable for two reasons: First of all, the intensities in the stretch mode region are strikingly different, with interfacial ice having a considerably higher intensity than water, as shown in Figure 4.4. This difference is in line with the strong intermolecular coupling present in the stretch region for ice[64], and its absence in the bend region. Secondly, the bulk infrared response of the ice bending mode is substantially weaker (by a factor 2-3) than that of liquid water (see Figure 4.3e). Nonetheless, the SFG bend mode intensities are very similar for ice and liquid water.

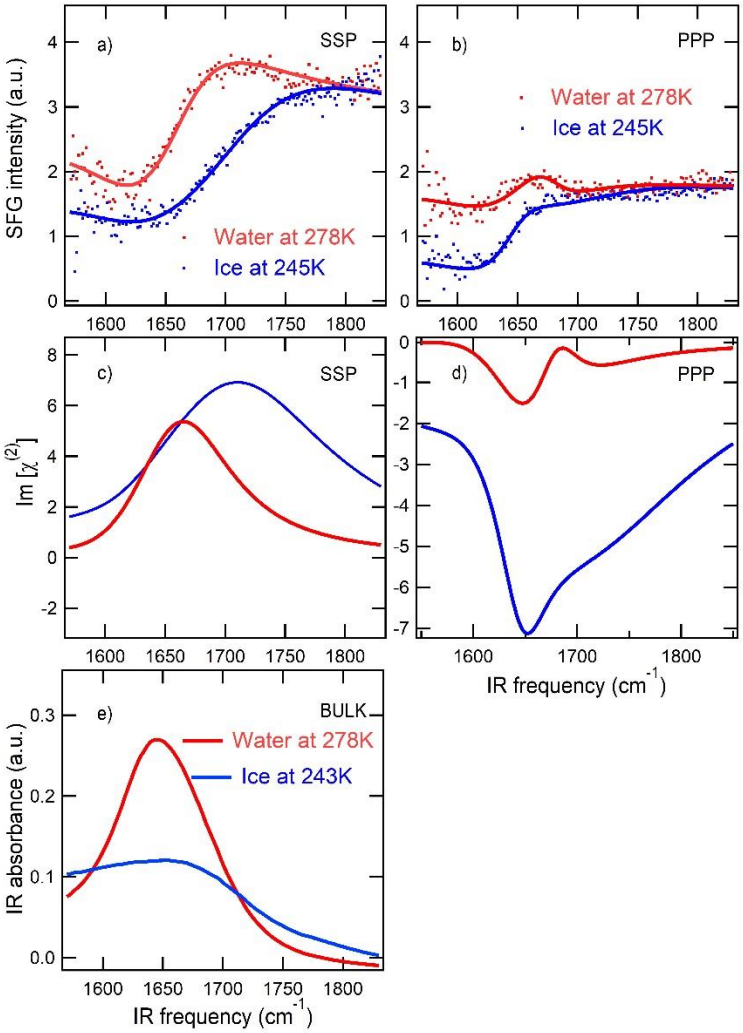

Figure 4.3: a) and b): Experimental SFG measurements (dots) and fits (solid lines) in the vibrational bend mode region of interfacial ice (blue) and water (red) with SSP measurements depicted in the left column, and PPP in the right. Water and ice spectra, also SSP and PPP are plotted on the same scale; see the Appendix for correction due to intensity alteration on the window of the ice cell. c) and d): Imaginary $\boldsymbol{\chi}^{(2)}$ for both polarization combinations obtained from the spectral fits. e) Linear infrared absorption spectra for bulk ice and water in the H-O-H bending region.

The bend spectra display dispersive lineshapes for both polarization combinations. The PPP spectra are less intense for both ice and water, compared to the SSP spectra. The SSP response is most insightful since it is determined by one independent ($\chi^{(2)}_{xxz} = \chi^{(2)}_{yyz}$) element of the $\boldsymbol{\chi}^{(2)}$ second rank tensor; the PPP response, in

contrast, contains contributions from two ($\chi^{(2)}_{xxz}$ and $\chi^{(2)}_{zzz}$) independent tensor elements[25], as explained in the Appendix. To quantify the observed spectral changes, the SSP spectra are fitted using a purely real non-resonant contribution and two complex resonant Lorentzian contributions (see Table 4.1 for the fitting parameters). The interfacial water SSP spectrum was described in accordance with previously reported parameters[56] in agreement with the reported heterodyne measurements of the water-air interface[68]. The high-frequency resonance is attributed to a DD-type water molecule, which donates two hydrogen bonds. The low-frequency resonance corresponds to a D-type molecule having one H-bond donating OH group and a dangling, free OH group[55,56,69,70]. Thus, the low- and high-frequency contributions correspond to water molecules having a free-OH and the strongly hydrogen-bonded water molecules at the surface, respectively.

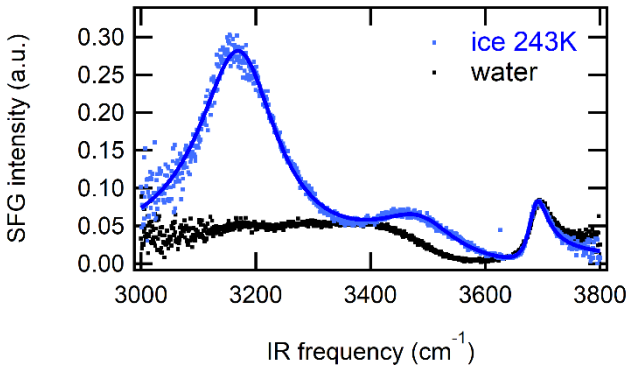

Figure 4.4: SFG spectra in the OH-stretch region of ice at 243 K and of water close to melting temperature

Ice and water – fit comparisons

To fit the interfacial ice SSP spectrum, the center frequency and linewidth of the low-frequency feature, corresponding to interfacial molecules with a free-OH, are kept similar to the fit for water. This assumption is based on the observation that the free-OH groups at the interface of water and ice have a very similar stretch frequency (Figure 4.4). The amplitude, central frequency, and linewidth of the high-frequency bend feature are allowed to vary between ice and water spectra. The SFG spectra in the bend-mode region are fitted using the expression:

$$I_{SFG}(\omega) = \left|\chi^{(2)}(\omega)\, E_{Vis}(w)\; E_{IR}(\omega)\right|^2 \qquad \text{Eq. 4.1}$$

wherein $\boldsymbol{\chi}^{(2)}$ is a sum of resonant and non-resonant contributions, related with a phase difference Φ, as follows:

$$I_{SF} \propto \left|\chi^{(2)}_R + \chi^{(2)}_{NR}\right|^2$$

$$or, \qquad \chi^{(2)} = A_{NR} * e^{i(\Phi)} + \sum_j \left(\frac{A_j * \Delta\omega_j}{\Delta\omega_j^2 + \sigma_j^2} + \frac{-iA_j * \sigma_j}{\Delta\omega_j^2 + \sigma_j^2}\right) \qquad \text{Eq. 4.2}$$

where A_{NR} is the non-resonant amplitude related to the resonant signal by a phase difference Φ; A is the strength of the vibrational mode, $\Delta\omega$ is the difference in the resonant and excited frequency, σ is the HWHM of the Lorentzian peak, and j is an integer representing number of Lorentzian resonances.

From fitting the interfacial ice SSP spectrum, a strong correlation between the position and width of the high-frequency peak was observed. The peak frequency varied between 1706 to 1689 cm^{-1}, when varying the peak width between 200 and 300 cm^{-1}; Table 4.1 shows the fitting parameters, and Figure 4.3c shows the imaginary part of the fitted response function.

A comparison of the interfacial ice and water spectra of the SSP polarization combination reveals that the ice bending mode is blueshifted by ~35 cm^{-1}, (taking an average peak position of 1697 cm^{-1} for the ice SSP response). This blueshift for the bend-mode feature represents stronger hydrogen bonding. From the empirical relationship[67] between the bend and stretch frequencies, a blueshift of 35 cm^{-1} for the bending mode of ice corresponds very well with the ~200 cm^{-1} redshift observed, Figure 4.4 displays the stretch mode in ice compared to water.

Table 4.1: Fitting parameters for the bend mode spectra of SSP and PPP polarization combinations for both ice and water. Values in brackets for ice denote alternative fitting parameters.

	Ice SSP	Water SSP	Ice PPP	Water PPP
NR Amp	-0.14	-0.16	0.1	0.13
ω_1 cm^{-1}	1612	1612	1612	1612
$2\sigma(\omega_1)$ cm^{-1}	130	130	130	130
A (ω_1)	0.9 (2.57)	1.3	-0.54 (-1.5)	-0.78
ω_2 cm^{-1}	1706 (1689)	1661	1706 (1689)	1661
$2\sigma(\omega_2)$ cm^{-1}	200 (300)	110	200 (300)	110
A (ω_2)	-7.3 (-13.8)	-3.6	4.38 (8.28)	2.16
ω_3 cm^{-1}			1646	1679
$2\sigma(\omega_3)$ cm^{-1}			60	60
A (ω_3)			1.1	-0.8

The vibrational bend bandwidth is roughly doubled for interfacial ice (200-300 cm^{-1}) compared to water (110 cm^{-1}), as is apparent from the raw data in figure 4.3a and the fits presented in Figure 4.3c and Table 4.1. This is in strong contrast to the OH-stretch lineshape being much narrower for interfacial ice than for interfacial water as seen in Figure 4.4, further narrowing upon lowering the temperature of ice[71]. If the ice surface bend mode were inhomogeneously broadened, the observed bandwidth > 200 cm^{-1} would translate to an extremely broad band of more than a 1000 cm^{-1} in the stretch region, using the empirical relationship mentioned above. This is clearly not observed, indicating that the bend mode of ice is predominantly homogeneously broadened, with a short dephasing time of the ice bend mode, which would include the pure dephasing time, population and orientational relaxation. Ultrafast studies of the bulk water bend mode report a vibrational lifetime of ~170 fs [57,72], and ultrafast anisotropy decay of 80 fs[73]. The >200 cm^{-1} bandwidth of the bend mode of ice compared to water, and the incompatibility with inhomogenous broadening mechanism, suggest sub-25 fs vibrational dephasing times for the bend mode of ice. Consistent with the interfacial spectra, the bulk bend mode spectrum also has a broader lineshape for ice, as seen from Figure 4.3e, also opposite to the stretch mode[74].

Comparison of the SSP and PPP spectra

Fitting for the PPP spectra was conducted keeping the SSP parameters corresponding to the effective (i.e. including the Fresnel factors) $\chi^{(2)}_{xxz}$ consistent (the amplitudes were adjusted according to prefactors as per equation 2.18), and adding an additional peak representing an effective $\chi^{(2)}_{zzz}$ as the additional tensor element in PPP spectra. The non-resonant signal contribution is kept purely real. Both PPP spectra can be very well fitted in (see Fig. 4.3b) and result in an additional peak at 1646 and 1679 cm^{-1} for ice and water, respectively.

From a comparison of the raw data for the two polarization combinations, we observe a spectral shift to the red side for the PPP spectrum compared to the SSP spectrum for both ice and water (Figure 4.5). Considering the complications of direct comparison from the data fits according to tensor elements described before, the spectral shift was quantified using simple sigmoidal fits to the ice and water spectra. For water, the PPP spectrum shift is quantified to be ~20 cm^{-1} to the red side. This shift is in line with the 15 cm^{-1} shift reported before[70], explained by the authors as an interference effect of two types of hydrogen bonding populations giving the same resonances in both the PPP and SSP response. However, we observe that an additional peak is needed to describe the PPP response; solely the SSP response is not enough. Interestingly, we observe an even larger frequency redshift for PPP compared to SSP in the case of interfacial ice, amounting to ~50 cm^{-1} as per the sigmoidal fit. This 50 cm^{-1} shift is in good agreement with the frequency difference between ω_2 and ω_3 in Table 4.1 indicating that for ice the PPP signal is dominated by the $\chi^{(2)}_{zzz}$ tensor element. A section in the Appendix elaborates on effects due to Fresnel factors, showing that optical effects due to setup geometry are not causing the differences.

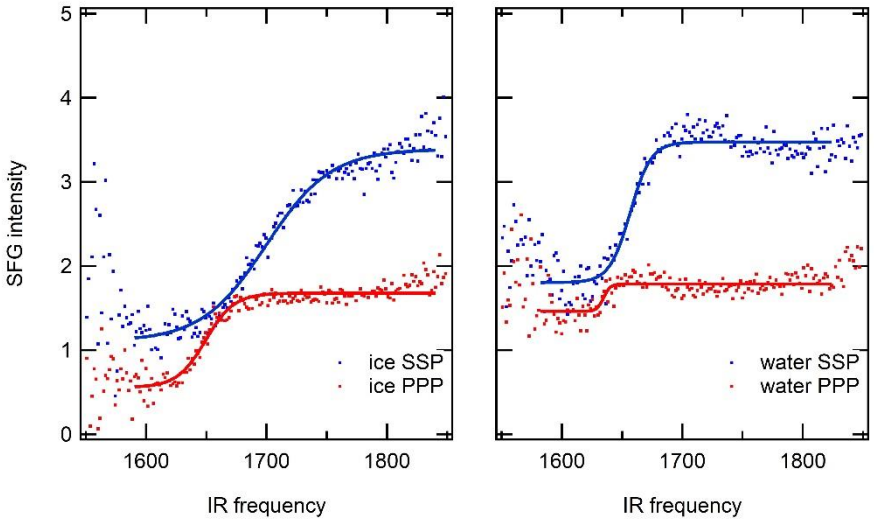

Figure 4.5: Sigmoidal fits to ice and water spectra in SSP and PPP polarization combinations. The fitting was performed to extract x-axis positions for the bend bands from the raw data to illustrate frequency shifts between the SSP and PPP spectra. From the fits, for water, the PPP (1634 cm^{-1}) spectrum shifts to the red side by ~20 cm^{-1} compared to the SSP spectrum (1656 cm^{-1}). For ice, a larger shift of ~50 cm^{-1} is observed between the PPP (1649 cm^{-1}) and SSP (1699 cm^{-1}) spectra.

Conclusions

In conclusion, this work has shed light upon the observed contrasting features of the bend mode spectra for ice and water, compared to the stretch mode. Stronger hydrogen bonding for ice manifests as a redshift in the stretch-mode region, and a blueshift in the bend mode region, as was empirically predicted and experimentally confirmed by our measurements. A comparable intensity of the bend mode for ice and water (unlike for the stretch mode), and little or no temperature dependence in our range of temperature variation, points towards negligible intermolecular coupling for the bend mode region. The anomalously increased bandwidth of ice in the bend mode compared to water points towards the line broadening mechanism to be predominantly homogeneous, unlike in the stretch mode. Also, polarization-dependent studies in the bend mode region indicate an inherent 20 and a 50 cm^{-1} frequency shift between the SSP and PPP spectra, for ice and water respectively, the origins of which remain incompletely understood.

Appendix

Intensity alteration due to CaF_2 window

Ice samples were measured inside a cell, with a CaF_2 window to allow equilibration of the ice sample in a closed environment, and to avoid evaporation to facilitate long-time measurements of the sample. However, to make a fair comparison of the SFG intensities on ice for SSP and PPP polarization combinations, one has to take into account the different reflectivity of P and S polarized light when interacting with a CaF_2 surface. An analysis for the Visible and SFG wavelengths is done below, as the Infrared remains constant for the SSP and PPP polarization combinations.

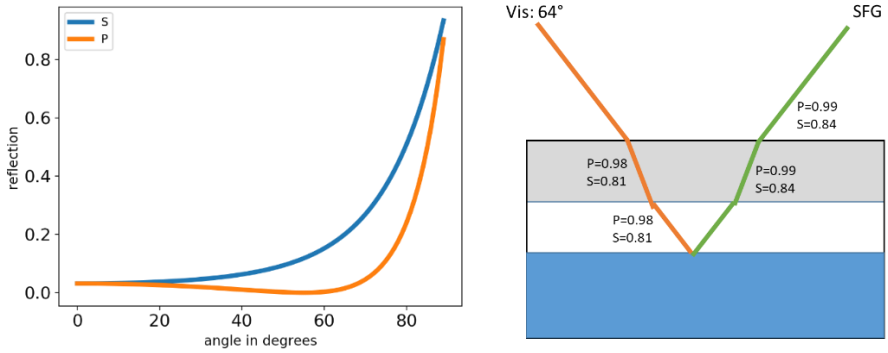

Figure 4.A1: left column: reflection coefficients of 800 nm S and P polarized light at the CaF_2 interface; right column: transmission accounted for incoming visible and outgoing SFG beams at the air-CaF_2 and CaF_2-air interfaces.

Figure 4.A1 left column shows the different reflectivity for S and P polarized light as a function of the incoming angle at an air-CaF_2 interface. The figure is depicted for an incoming visible beam of 800 nm wavelength. The refractive index of CaF_2 for the visible beam of 800 nm and the SFG outgoing beam of ~704 nm was taken as 1.4306 and 1.4317, respectively. The incoming angle of the visible beam was 64° and the SFG beam was calculated to be reflecting at 60°. The S and P reflection coefficients were calculated using the Fresnel equations for reflection and transmission. From Figure 4.A1 left column, it is apparent that at an angle of ~65°, there is a ~20-fold difference in the reflectivity coefficients of S and P polarized light. Using Fresnel equations for intensity reflectance and transmission coefficients, the transmission (or 1 – reflectance) of Visible light at the air-CaF_2 interface (P=0.98, S=0.81), and at the CaF_2-air interface (P=0.98, S=0.81), coupled with the reflection loss of SFG light at the air-CaF_2 interface (P=0.99, S=0.84), and then at the CaF_2-air interface (P=0.99, S=0.84), as depicted in the right column of Figure 5.A1, the subsequent light transmission out of the window is 0.94 for the PPP, and 0.45 for the SSP beams. Therefore, for fair comparison between SSP and PPP spectra, the SSP spectra were multiplied by a factor 2 to account for the reflection losses due to the CaF_2 window.

Contributions due to setup geometry: influence of Fresnel factors

The lineshape of an SFG spectrum can be adversely affected by the local electric fields of the incoming/outgoing beams at the interface[75]. An introduction to Fresnel factors was made in Chapter 2. For the experiment, the refractive index of air n_1 was taken as 1, for n_2 (refractive index of second medium: water or ice), the value was taken from Warren (1984)[76] for Visible wavelength 800nm and SFG wavelength 704 nm. For the infrared light, the values were taken from Zasetsky et al[77], for ice at 235 K and water at 273 K.

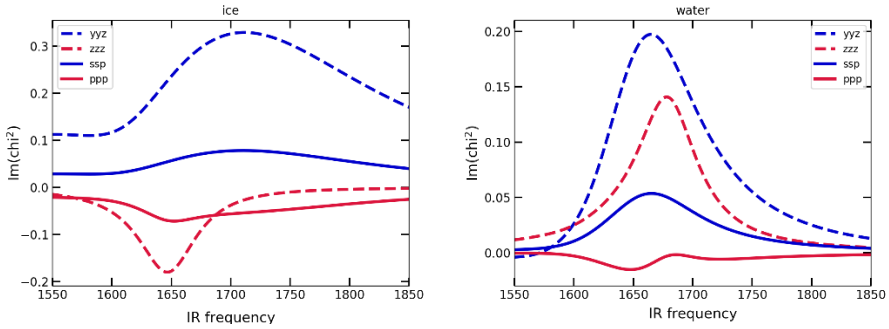

Figure 4.A2: Imaginary $\chi^{(2)}$ responses of the SSP and PPP spectra obtained from fitting SFG intensity data shown in red and green respectively; and of the calculated yyz and zzz tensor elements shown in blue and orange respectively. Left column displays spectra for ice, and right for water.

To analyse the effects of incoming beam angles and polarizations, Fresnel-corrected spectra are obtained for the $\chi^{(2)}$ tensor elements corresponding to SSP and PPP polarizations. The complex $\chi^{(2)}_{eff}$ required for the Fresnel factor analysis, are obtained from fitting the measured SFG intensity spectra in SSP and PPP polarization combinations; the fitting parameters are mentioned in the main text. The imaginary part of the $\chi^{(2)}_{eff}$ obtained from fits to the SSP and PPP data are plotted in green and red respectively, for ice (left column) and water (right column), in Figure 5.A1. These responses were used to calculate the $\chi^{(2)}_{yyz}$ and $\chi^{(2)}_{zzz}$ for the two systems, also plotted in Figure 4.A1 in blue and orange respectively. $\chi^{(2)}_{yyz}$ is calculated using equation 2.18 where the $\chi^{(2)}_{eff,SSP}$ is obtained from fitting the measured SFG intensity in SSP polarization combination. The $\chi^{(2)}_{yyz}$ thus obtained is then used to calculate $\chi^{(2)}_{zzz}$ from equation 2.19. $\chi^{(2)}_{yyz}$ and $\chi^{(2)}_{zzz}$ are the $\chi^{(2)}$ responses without influence of the Fresnel factors. Clearly, the differences between ice and water also remain in the $\chi^{(2)}_{yyz}$ and $\chi^{(2)}_{zzz}$ spectra. Therefore, we conclude that the differences between ice and water in spectral features observed for the SSP and PPP polarization spectra are not an optical artefact, but an inherent feature.

Figure 4.A3 is a direct comparison of the $\chi^{(2)}_{yyz}$ for ice and water (in solid and dashed lines, respectively). The blue-shift for the ice spectrum compared to water for the Fresnel-corrected SSP spectrum, reinstates the frequency shift observed in the measured intensity spectra to be indeed a physical phenomenon, and not an optical 'illusion' seen in the intensity spectra.

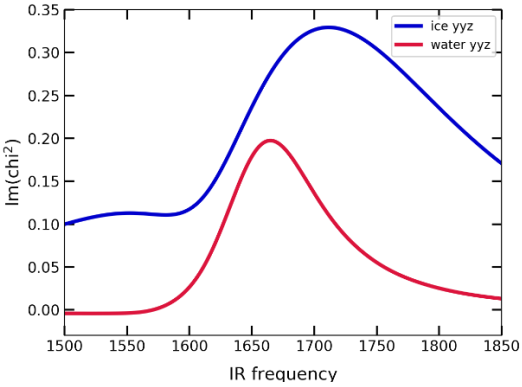

Figure 4.A3: direct comparison of the $\chi^{(2)}_{yyz}$ responses of ice and water.

Chapter 5

Proton ordering on the surface of ice

ABSTRACT: The surface of ice is complex, yet imperative for glacier motion, sliding and adhesion, and providing the atmospherically relevant environment for molecular adsorption and photocatalytic conversion. As such, the ice surface has been intensely studied and several of its unique properties have been elucidated, in particular the presence of a disordered liquid-like layer at temperatures well below the freezing point. The bulk of ice being orientationally disordered has also long been established, but the surface of ice is thought to reconstruct to a proton-ordered formation accounting for electrostatic stability. This work explores the proposition of the coexistence of the disordered liquid layer, followed by a proton-ordered layer before the remainder bulk of the ice. The concepts of residual entropy and enthalpy are explored, and related to experimental measurements in the –OH stretch region of interfacial ice. The current status of the work hinders from making conclusive statements, and asks for further research in this domain.

Introduction

The ice surface has been a subject of fundamental interest encompassing atmospheric, terrestrial, and interstellar sciences. After postulation of the ice rules by Bernal and Fowler[78] in 1933, Pauling[79] already in 1935, based on disordered positions of hydrogen atoms in the ice crystal, theoretically calculated the residual entropy of ice, which was soon affirmed by experiments in 1936 based on measurement of the heat capacity of ice by Giauque and Stout[80]. Pauling's estimate however was a lower bound, as was recognized by advanced theoretical approximations by Nagle[81]. Various computational approaches have since then taken over, and the residual entropy of ice has become a standard to test accuracy of simulation algorithms[82].

Residual entropy is directly related to the configuration number, an estimate of the discreet representative positions of a system. It has been shown theoretically that the proton order versus disorder effects in the bulk of the ice do not have a major impact on the crystal lattice energy[11,83], a difference within ~5 meV/H_2O was seen for the different configurations. At the surface, the energy differences between differently proton ordered configurations amounted to almost an order of magnitude more[11], ~100 meV/H_2O. The surface

proton activity of ice has been shown to be markedly enhanced (three orders of magnitude more) compared to its bulk[84]. While the bulk of ice remains fully disordered over the entire temperature range, the ice surface will not become fully disordered at any meaningful temperature before the onset of pre-melting[11,85]. The estimated order-disorder transition temperature at the surface is as high as 390 K[86]. Low surface entropy of polar liquids like water has been associated to ordering of layers of surface molecules, proposed in 1956[87].

Fletcher in 1992 proposed that at temperatures below the quasi-liquid-layer (QLL), the surface of ice will undergo reconstruction to reduce surface free energy involving the orientation of surface dipoles into a striped phase with alternating rows of dangling H and dangling O atoms[88]. Today, we know that the temperature[89] at which pre-melting begins is estimated to be in the range of 200 – 260 K[9,71,90,91]. In fact, a recent study reported that as temperature increases above 200 K, there is a strong interplay of disordering of the bond order keeping oxygen positions fixed, and the disruption of oxygen framework altogether, in the structural evolution of the ice surface[92]. In this work, we explore the proposition of the coexistence of three distinct regions: the disordered QLL on the top, proton-ordered layer(s) below that, and finally the bulk of the ice crystal. The proposed idea accounts for counteracting findings of the prevalence of proton ordering at temperatures as high as 390 K, and pre-melting starting to occur already at 200 K.

We employed both experimental and theoretical methods to study the proposition, being Sum Frequency Generation (SFG) spectroscopy to probe the buried proton-ordered layers at the surface of ice at varying temperatures; and ab-initio-based POLI2VS molecular dynamics simulations simulating the SFG spectra. To be able to experimentally study ice surfaces, large single-crystalline ice samples are synthesized and measured in a moving cell to prevent laser-induced heating. Moreover, consistency in the temporal overlap of the two laser beams, on the order of a hundred femtoseconds, is maintained during spectroscopic measurements to avoid variation of frequency-dependent lineshape of SFG spectra[93].

Results and discussion

Figure 5.1 displays the SFG intensity of interfacial ice at temperatures from 228 K (blue) to 255 K (yellow), as a function of the IR frequency. The interfacial ice spectra have three prominent features: the hydrogen-bonded OH-stretch symmetric mode around 3200 cm^{-1}, the asymmetric stretch mode of fully-coordinated water molecules around 3500 cm^{-1}, and the high-frequency peak at 3700 cm^{-1} arising from water molecules with a free-OH pointing up. Clearly, the 3200 cm^{-1} feature is strongly temperature-dependent, increasing sharply upon lowering the temperature. The peak intensity increases almost 4.5-fold for an 11% drop in temperature from 255 K. The Free-OH region however maintains a rather stable intensity count in this temperature range. The experimental spectra of interfacial ice are qualitatively consistent with previous reports. However, there have been discrepancies reported in the intensity ratio of the bonded-OH to the Free-OH peaks[63,71,94]. The wide range of values can be attributed to the sensitivity of the ice surface to evaporation, contamination, equilibration conditions, variation in surface reflectivity, and macroscopic changes induced due to surface tension effects over time. Therefore, considerable attention was paid to growth and handling conditions of ice samples for measurement.

This chapter aims to explain the underlying mechanism of the sharp increase of the 3200 cm^{-1} peak of the interfacial ice spectra with decreasing temperature. As mentioned above, this decrease has been observed before, but a fundamental understanding of the behaviour is lacking. Theoretical studies point towards intermolecular coupling as the major contributing factor for the sharp rise in intensity[64,95]. However, an increasing number of studies also point to the reordering of the surface, potentially reasoning the to the

observed rising SFG intensity[87,96,97]. This work aims on disentangling these two effects with the help of simulations, and basic theoretical calculations, supporting experimental data.

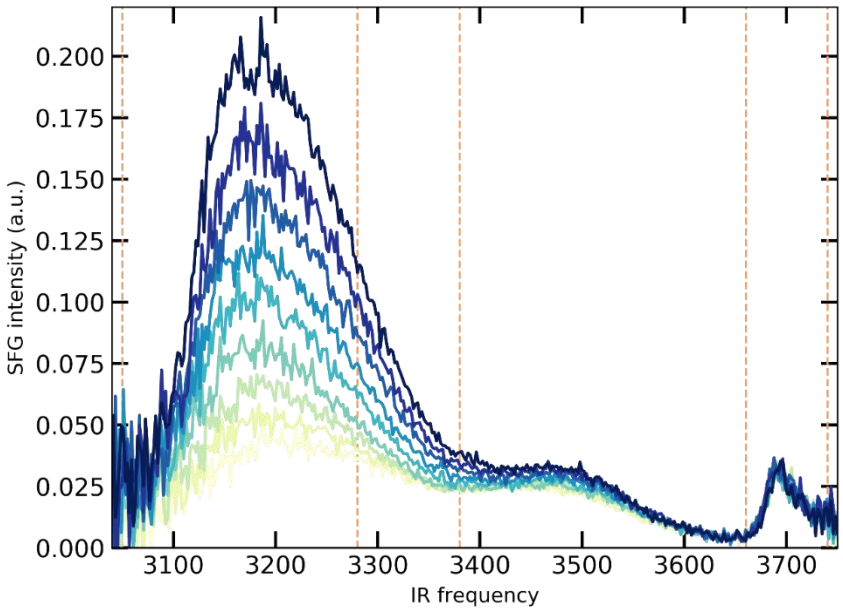

Figure 5.1: SFG spectra (in arbitrary units) plotted as a function of the IR frequency in wavenumbers for hexagonal ice oriented to the basal plane, at temperatures ranging from 228 K (darkest color) to 255 K (lightest color)

Simulations on proton-ordered models

To shed light on the strong intensity increase of the 3200 cm^{-1} peak with decreasing temperature, ab-initio-based molecular dynamics simulations based on the POLI2VS model were conducted at three temperatures. The 3200 cm^{-1} peak is associated to the hydrogen-bonded OH-stretch populations, and is reported to be sensitive to intermolecular couplings. Intermolecular coupling is extremely sensitive to the relative orientation of chemical bonds through their transition dipole moments[98].

In 1961, Fletcher proposed the surface of ice to be arranged in an alternately striped pattern of water molecules, composed of molecules with their Free-OH groups pointing up, and those with an Oxygen lone-pair pointing up. 'Fletcher pattern' is widely accepted in the community to present the most likely form of proton ordering on the ice surface owing to its electrostatic stability. The Ferroelectric model has also been proposed, but was concluded to be energetically less favourable. The Ferroelectric model is described by all surface molecules in the upper half of the first bilayer having a Free-OH pointing up[99].

The Fletcher pattern, comprising of a simple striped arrangement of protons, applies to the single top layer of the ice surface. Figure 5.2 is a top view, looking down the c-axis of a Fletcher-patterned proton-ordered basal ice surface.

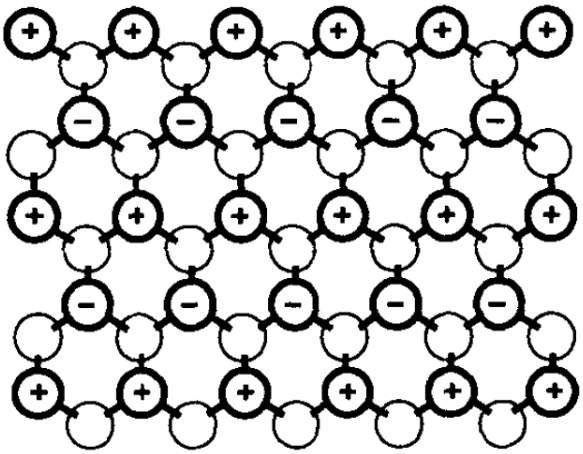

Figure 5.2: Fletcher-patterned proton-ordered ice surface looking down the c-axis. Figure from reference[88].

The bold circles represent water molecules with broken hydrogen bonds or the three-coordinated water molecules on the surface, the thin circles represent fully H-bonded four-coordinated molecules. The negative circles represent an Oxygen lone-pair pointing up, and positive circles represent the Free-OH pointing up.

However, what if this proton-ordered arrangement extends beyond the exposed surface layer? Although multiple ordered bilayers entail an entropic cost, that could be compensated by increased electrostatic interactions between the molecules. To test this hypothesis, three different models, Ih0, Ih2, and Ih3 were initiated as starting points for simulation trajectories. Since the ice structure is a 'bilayered arrangement', the models comprise of 0, 1.5, and 2.5 ordered bilayers respectively, and the configurations were chosen so the individual bilayers are in accordance with the Fletcher pattern.

Figure 5.3 shows snapshots of the three model configurations and their SFG spectra at different temperatures. Clearly, for the proton-disordered model Ih0, there is less than 40% increase in signal intensity for a temperature decrease of ~18%, which does not go along with the experimental observations. For the proton-ordered models Ih2 and Ih3, with 1.5 and 2.5 top bilayers ordered, respectively, the increase in intensity is quantitatively more comparable to the experimental results. To directly compare the experimental and theoretical results, the ratio of the 3200 cm^{-1} and 3700 cm^{-1} peak areas (considering spectral ranges 3050 to 3280 cm^{-1}, and 3660 to 3740 cm^{-1}) as a function of temperature is plotted for the simulation models and the experimental data in Figure 5.4. The ratio of the peak areas is considered and not the individual intensity to minimize nuclear quantum effect. A choice of quantum correction factors can be used to simulate systems. Taking a ratio of the two peaks instead of the 3200 cm^{-1} peak individually to evaluate peak areas, led to similar quantum corrections at low and high temperature for both the standard and the harmonic quantum correction factors, i.e. Q_S and Q_H respectively.

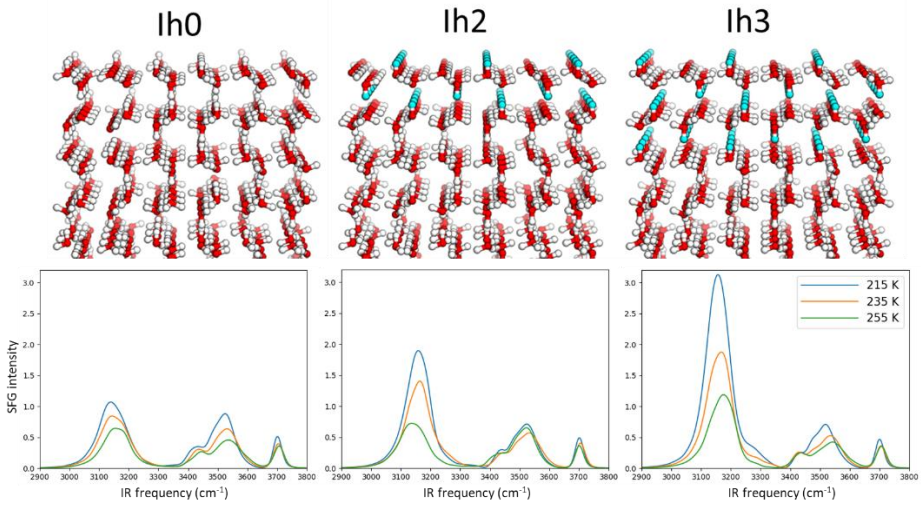

Figure 5.3: models and calculated SFG spectra at different temperatures: data from Yuki Nagata and Fujie Tang

The simulations are run for a few nanoseconds; the molecular orientation of water molecules is maintained throughout the trajectory. From Figure 5.4, each of the models, including the proton-disordered and the proton-ordered configurations, show a temperature dependence. Comparing the three models, clearly, there is a stronger temperature dependence for a more proton-ordered model. The experimental curve behaves different from any of the simulation models.

At 255 K, the experimental curve is in closer proximity to the proton-ordered models and not the proton-disordered model, suggesting prevalence of proton ordering at the ice surface, already at 255 K. Proton ordering taking place at high temperatures is in agreement with theoretical calculations, predicting the order-disorder 'transition temperature' to be near 390 K which is well above the melting temperature. The figure also points towards the different temperature dependence for the experimental data compared to the simulation models. The models have a linear-like function, while the experimental curve appears more exponential. As pointed out before, the simulation models represent a fixed ordering arrangement, as the trajectory runs were too short for rotational equilibration of water molecules to occur. Experiments though depict a time-averaged situation, and the data could thus suggest a hopping proton ordering mechanism wherein there is a jump from one model to another as proton ordering progressively increases upon decrease in temperature. The above analysis is thus not very precise in accounting for change of proton ordering over the studied temperature range. It is still of interest to theoretically evaluate if such a hopping were to take place, and the temperature range for the thermodynamic stability of such systems.

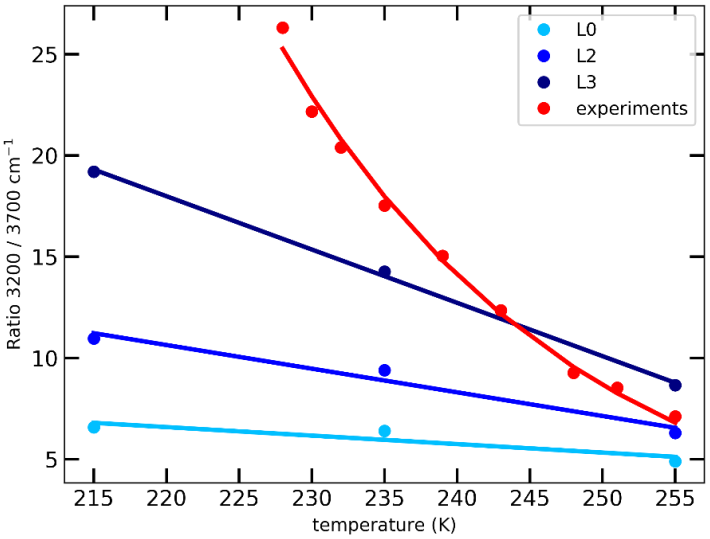

Figure 5.4: comparison of the ratio of the 3200 and 3700 spectral areas for the simulation models Ih0, Ih2, Ih3 and linear fits to them, as well as the experimental data with an exponential fit.

Entropic and enthalpic calculations for the different models

In the reconstructed Fletcher model (Figure 5.2), every surface molecule has six other neighbouring surface molecules (see second neighbours in the crystal structure in Figure 5.2), 4 of them point in the anti-parallel direction, and 2 point in the parallel direction. Considering water to be a symmetric tetrahedral structure, the bond dipole μ can be calculated from the total water molecular dipole μ_w as: $\mu_w = \mu \cos 52°$, obtaining

$$\mu \approx 2 * 10^{-30}\ Cm$$

Considering only the broken bonds protruding from the surface, as depicted in Figure 5.3a, the Coulomb forces between one bond dipole and its neighbouring 2 antiparallely (resulting from 4 antiparallel and 2 parallel) arranged dipoles can be evaluated. This leads to an electrostatic interaction energy of an approximate magnitude:

$$\Delta U_B = -\frac{\mu^2}{\pi \varepsilon_0 a^3} \approx -2 * 10^9 \frac{\mu^2}{r^3}$$

where r is the O-O bond length, and a = 1.6r, giving -10^9 J for interaction with one neighbouring dipole moment.

For a molecule at a randomly configured surface, or a proton-disordered surface, the antiparallel and parallel neighbours are equal in number, giving zero net electrostatic energy. Using the above equation, the change in enthalpy (ΔU_B) for the different simulation models, and for the Fletcher-patterned surface, as well as a

Ferroelectric model surface is calculated and displayed in Table 5.1. The evaluation was done for a system containing 10 bilayers, every bilayer having 60 water molecules. Only bond dipoles (the –OH bond dipole moment obtained from molecular dipole moment of water, as described above) in the first bilayer are considered when evaluating ΔU_B values, since dipoles in the bulk would have a counterpart. Hence, the Ih2 and Ih3 models end up having the same change in enthalpy as the Fletcher model, and Ih0 has no enthalpy change as the surface is randomized.

Table 5.1: Evaluation of Fletcher, Ferroelectric, and simulation models; number of molecules for the simulation models split up in brackets as per contribution from different bilayers

	Fletcher	Ferroelectric	Ih0	Ih2 (Ih2_qll)	Ih3 (Ih2_qll)
Number of ordered molecules	30	30	0	90 (60+30)	150 (60+60+30)
Total neighbouring dipoles per bond dipole	2	6	0	2	2
ΔU_B (kcal per mol)	-0.055	0.166	0	-0.055	-0.055

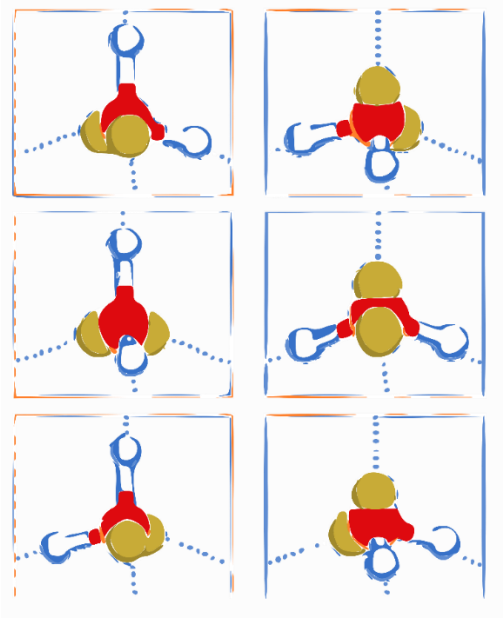

Figure 5.5: Blue-outlined: Covalently bonded hydrogen atoms; red: oxygen atom; mustard: oxygen lone-pairs. Displayed are 6 ways following the ice rules from 16 possible conformations of 4 Hydrogen atoms arranged around 1 Oxygen atom. Additionally, the left column depicts the 3 orientations of a molecule with a Free-OH pointing up, and the right column for molecules with an Oxygen lone-pair pointing up. Figure adapted[100].

Similarly, the residual entropy can be calculated for the above models, making use of the 'ice rules'. For a proton-disordered crystal, the following simple scheme can be employed:

- First rule: there is 1 hydrogen atom on each bond
- Second rule: there are two hydrogen atoms covalently bonded to each oxygen atom.

- If we consider N water molecules in a crystal, then there would be 2N Hydrogen atoms.
- Ignoring the 2nd rule for now, there are 2^{2N} configurations possible for the Hydrogen atoms to fulfil the first rule, since each Hydrogen atom has possibilities to bond to 2 oxygen atoms to form a H-bond.
- With the 4 Hydrogen atoms around 1 Oxygen atom, 16 different configurations are possible (4^2), however only 6 of them satisfy the 2nd rule. These 6 configurations are shown in Figure 5.5.
- Hence, the configurational number $W_0 = 2^{2N} * (6/16)^N = (3/2)^N$
- Residual entropy is thus equal to: $S_0 = k_B * \ln(W_0) = k_B * \ln (3/2)^N$

For the Fletcher-patterned surface, there are further orientational restrictions imposed on the surface molecules in the upper bilayer, with either a dangling-OH or an oxygen lone-pair pointing up. These 3-fold coordinated water molecules can orient in 3 different ways from the 6 shown in Figure 5.5. The left and right columns depict possibilities for molecules with a dangling-OH and an oxygen lone-pair, respectively. The residual entropy for these molecules thus turns out to be:

$S_{Fletcher} = k_B * \ln (3/2)^N (3/6)^N = k_B * \ln (3/4)^N$

This amounts to a change in entropy of $k_B \ln (3/2) - k_B \ln (3/4) = - k_B * \ln 2$ for the surface molecule.

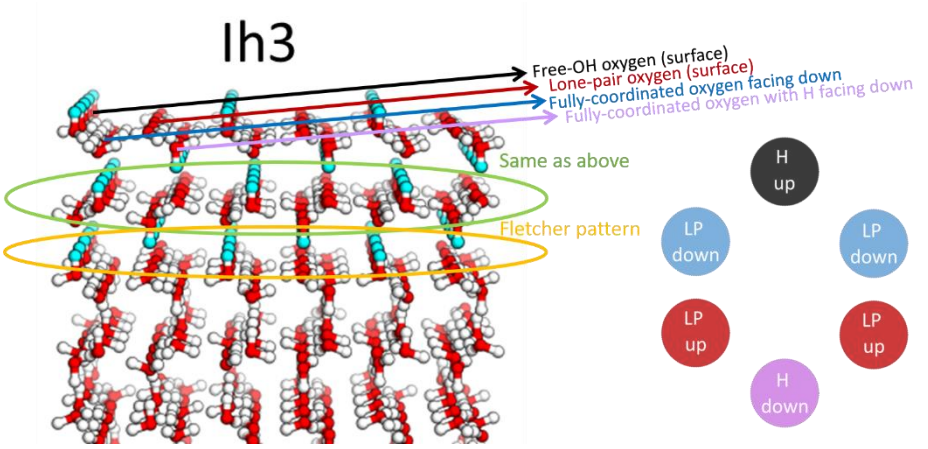

Figure 5.6: a) categorization of water molecules into 4 different types for entropic calculations; b) 6-membered water molecule ring with molecular orientations as illustrated in part a.

For the simulated models Ih2 and Ih3, the molecules are restricted in more ways than just the restrictions owing to the Fletcher pattern ordering. As can be seen in Figure 5.3, the ordering of molecules is prevalent not just at the surface, but extends further down to multiple bilayers. The fixed orientations of the OH-groups pointing up in the second/third bilayer, also pose restrictions on the 4-coordinated water molecules in the bilayer above them, which were left free in the Fletcher-patterned proton ordering model. To evaluate the entropy, the molecules due to their different orientational restrictions in the simulation models Ih2 and Ih3 are categorized into 4 types, as illustrated in Figure 5.6a.

Although with more restrictions added, it would be intuitive to think that the residual entropy of molecules corresponding to the second and third bilayers in model Ih3 would be far higher than that of the first layer

(Fletcher pattern). Upon further thought, the constrained bond dipoles of the free-OH pointing up (type 1), and a free-OH pointing down (type 4) are able to interconnect bilayers through interacting with the oxygens of the bilayers above or down. This eventually leads to a cumulative effect of every bilayer acting as a Fletcher layer, with the free-OH pointing up or down, or the oxygen lone-pair pointing up or down, each having 3 from 6 possibilities as described before. Therefore, one would expect that the residual entropy would be calculated as per the Fletcher pattern, corresponding to the number of constrained molecules per bilayer to be considered.

To confirm the above speculation on entropic contribution, we decided to work on a simplified system of a 6-membered water molecule ring, considering molecules of restrictions of the 4 types described in Figure 5.6a, and evaluate the different configurations of the molecules possible. Such a ring is shown in Figure 5.6b, and turns out that with the restrictions taken into account, 14 different configurations were possible, all of them displayed in Figure 5.7.

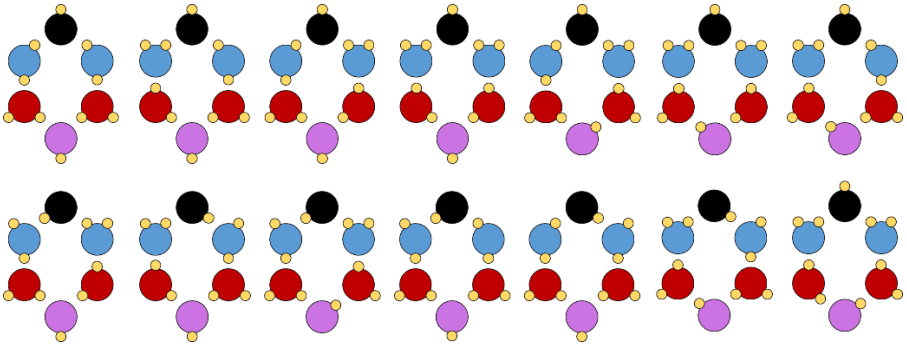

Figure 5.7: All possible configurations for a 6-membered water molecule ring consisting of the 4 types of molecules displayed in Figure 5.6b, same colours denoting the type of molecules; covalently bonded hydrogen atoms shown in yellow.

Hence, $W_0 = 14/2^6$ for 6 molecules; and $W_0 = (14/2^6)^{1/6} = 0.776$ for 1 molecule
This is very similar to the entropic contribution for a Fletcher-patterned surface which amounts to $W_0 = ¾ = 0.75$, as was described above. This leads to a total change in the entropic contribution to be $– k_B \ln(2)$.
Therefore, the final entropic change for the Ih2 and Ih3 models are:
$\Delta S_{Ih2} = – 1.5*60\ k_B \ln(2)$: which comes from having 1.5 bilayers, and each bilayer having 60 molecules consisting of dangling-OHs and oxygen lone-pairs.
$\Delta S_{Ih3} = – 2.5*60\ k_B \ln(2)$: from 2.5 bilayers.
The residual entropy for the Ferroelectric model is going to be the same as the Fletcher model.

Finally, using the enthalpic and entropic contributions evaluated above, the change in Gibb's free energy is calculated, and plotted as a function of temperature in Figure 5.8 for all the models described above.

From Figure 5.8, it is clear that the proton-disordered model (blue dashed line) has the lowest Gibb's free energy for almost the entire temperature range, compared to all the other proton-ordered models. Only after we approach very low temperatures is there a crossing point of the Fletcher model, which starts to become more stable with still lower temperatures. The Fletcher model, represented in green in Figure 5.8 starts becoming energetically favourable at around 40 K, which is close to the temperature range suggested by Fletcher in 1992[88]. Therefore, we would expect a complete proton ordering on the surface of ice to take

place in that temperature regime. The ordering of the surface energetically points towards the Fletcher pattern, as the Ferroelectric model remains unfavourable across the entire temperature range. Ih2 and Ih3 models are also energetically unfavourable, and only happen to cross over with the proton-disordered system around 5 K.

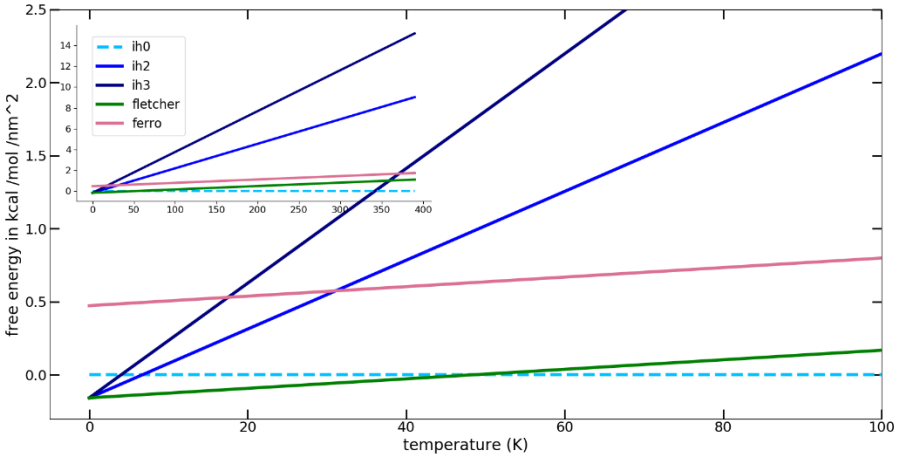

Figure 5.8: Free energy as a function of temperature for the different models

So far, for simplicity of explanation, it was assumed that water molecules in all bilayers are arranged in an ice-like fashion. However, at least the top surface bilayer of ice is known to be a quasi-liquid layer (QLL) at temperatures above 200 K. Assuming our original system taking into account the top layer to be a QLL, and the second bilayer being proton ordered, the Ih2 system perfectly transforms into a Fletcher-patterned proton-ordered system with a QLL on top of it. Similarly, the Ih3 model transforms into an Ih2 model with a QLL on top.

The entropic and enthalpic values theoretically calculated for the models before clearly did not lead to values compatible with experiments. However, using Buch's enthalpic values from MD simulations for a Fletcher-patterned ice basal surface[86], the Gibb's free energy was proposed to cross over the proton-disordered state at a temperature as high as 390 K, as plotted in Figure 5.9 and mentioned earlier in the text. Since the entropy consideration by Buch was indeed using the Fletcher model itself, it seems likely that our enthalpy calculations are based on an oversimplified model, and rigorous simulation trajectories can indeed do a better job, also considering distant bond dipoles, etc.

With the Ih0, Ih2, and Ih3 simulation models above, and also having calculated values for the Fletcher and Ferroelectric models, we expect a complete proton-ordered transformation at the surface of ice at temperatures much below our temperature range of study. Although the analysis above could provide quantitative information about the equilibrated state of complete proton ordering, information on the transitory states in between is missing. The models used above are not consistent with the 'real' proton ordering observed in experiments, as the status of proton ordering in the simulations remains static with temperature. Thus, a different model that explains the transitioning of the ice surface from a less proton-ordered to a more proton-ordered state, might be helpful.

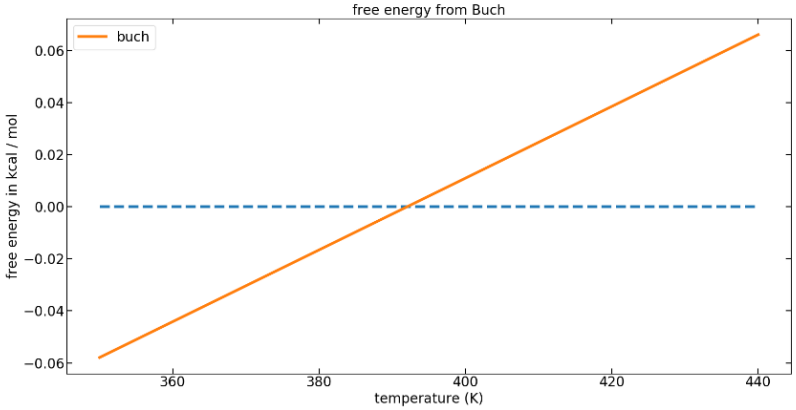

Figure 5.9: Gibb's free energy plot using parameters from Buch

Less proton-ordered state to a more proton-ordered state

A different way to analyse the data is by considering a continuous transition from a less ordered to a more ordered state. Equilibrium constant K_{eq} of the reaction from a less ordered to a more ordered state, can be represented as:

$$K_{eq} = \frac{[more\ ordered]}{[less\ ordered]} \qquad \text{Eq. 5.1}$$

K_{eq} can be linked to ΔG by:

$$\Delta G = -RT \ln K_{eq} \qquad \text{Eq. 5.2}$$

As we know that,

$$\Delta G = \Delta H - T\Delta S \qquad \text{Eq. 5.4}$$

K_{eq} can be related to ΔH and ΔS:

$$\ln K_{eq} = \frac{\Delta G}{-RT} = \frac{\Delta H}{-RT} - \frac{T\Delta S}{-RT} = \frac{-\Delta H}{RT} + \frac{\Delta S}{R} \qquad \text{Eq. 5.5}$$

Assuming that the SFG signal is a measure for an ordered state, $K = \sqrt{SFG\ intensity}$

Figure 5.10 represents the natural log of the square root of spectral areas for the 3200 cm^{-1} SFG peaks, as a function of the inverse temperature. Plotting $\ln K_{eq}$ as a function of $1/T$, the slope will be $\Delta H/R$, while the intercept should be related to ΔS. However, as the intercept depends on our measurement conditions (i.e. higher acquisition time will increase the intercept; while slope remains the same), we cannot conclude anything about the entropy from our data. However, we could link the slope to the change in enthalpy.

From the average value of the experimental slope, we obtain that
ΔH = -11.8 kJ/mol = -2.79 kcal/mol

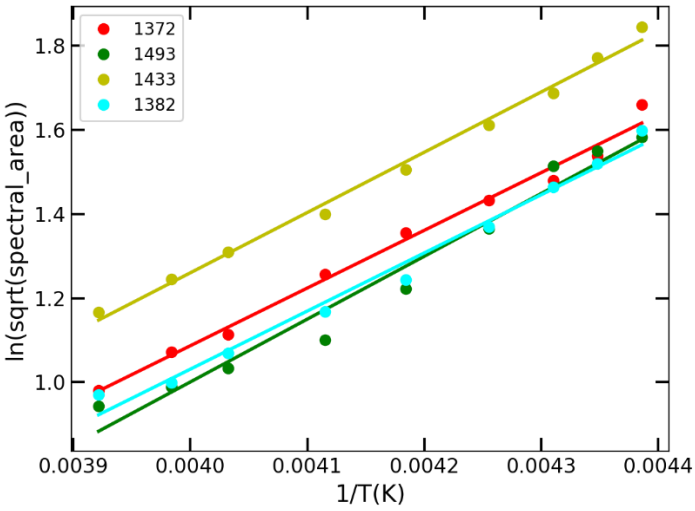

Figure 5.10: Arrhenius plots for a less proton-ordered to a more proton-ordered state; legend displays the slope values for multiple sets of experimental measurements

To place this number into context, the ΔH obtained using the method above is ~50 times the value obtained from the dipole-dipole coupling model (Table 5.1). The value obtained from the dipole coupling model is a lower limit, since, for instance, it does not take the distant-dipoles coupling into account. But our value obtained is also 5 times larger than Buch. More accurate calculations using simulations would be helpful.

Conclusions

Clearly, from the analysis so far, our understanding about proton ordering on the ice surface is far from complete. The proposition of having a quasi-liquid layer (QLL) at the ice surface, followed by a proton-ordered layer, and finally by the bulk is an enticing one, but definitely requires more theoretical help for a better estimation of the enthalpic contribution of such a system. Our assumption in the current study of the enthalpic contribution being the same as for the Fletcher model may have considerably outplayed the considered models. With the current analysis, the Gibb's free energy values for the proton-ordered models have a crossing point with the proton-disordered models at temperatures that far too low in comparison with the temperature range of our experimental studies. However, considering a different analysis modus and assuming a simple transition from a less ordered to a more ordered state of the ice surface, we could estimate an enthalpic value of ~2.79 kcal/mol, which is on a higher end of the values reported both by Buch, and that obtained from the dipole-dipole coupling model. As of yet, we are unable to make solid claims on what this means, but we hope to encourage further efforts in this direction from both experimental and theoretical contributions.

Chapter 6

Interfacial vibrational dynamics of Ice I_h and liquid water

This chapter is reused in most of its content, with permission, from the published article: *J. Am. Chem. Soc.* 2020, 142, 28, 12005–12009; with the source https://pubs.acs.org/doi/abs/10.1021/jacs.0c04526. Any further permissions related to the material should be directed to the ACS.

ABSTRACT: Insights into energy flow dynamics at ice surfaces are essential for understanding chemical dynamics relevant to atmospheric and geographical sciences. Here, employing ultrafast surface-specific spectroscopy, we report the interfacial vibrational dynamics of ice I_h. A comparison to liquid water surfaces, reveals accelerated vibrational energy relaxation and dissipation at the ice surface for hydrogen-bonded OH groups. In contrast, free-OH groups sticking into the vapor phase exhibit substantially slower vibrational dynamics on ice. The acceleration and deceleration of vibrational dynamics of these different OH groups at the ice surface are attributed to enhanced intermolecular coupling, and reduced rotational mobility, respectively. Our results highlight the unique properties of free-OH groups on ice, putatively linked to the high catalytic activities of ice surfaces.

Introduction

Solar photon-induced vibrational overtone pumping induces photodissociation of atmospherically-relevant compounds[101] like HNO_4[102], HO_2NO_2[103], H_2SO_4[104], etc. When such reagents are adsorbed on omnipresent aqueous or ice surfaces, their vibrational modes can couple to water vibrational modes, e.g., through energy transfer[105], thereby influencing the reaction pathway. Adsorption on aqueous surfaces can, moreover, shift and intensify OH-stretch overtone absorptions[106], and accelerate photodissociation reactions by orders of magnitude[107]. Besides the potential importance for atmospheric chemistry[47,108], vibrational energy dynamics on aqueous surfaces are also of fundamental interest for understanding the surface and interfaces[109,110] of arguably the most important molecule on earth: water.

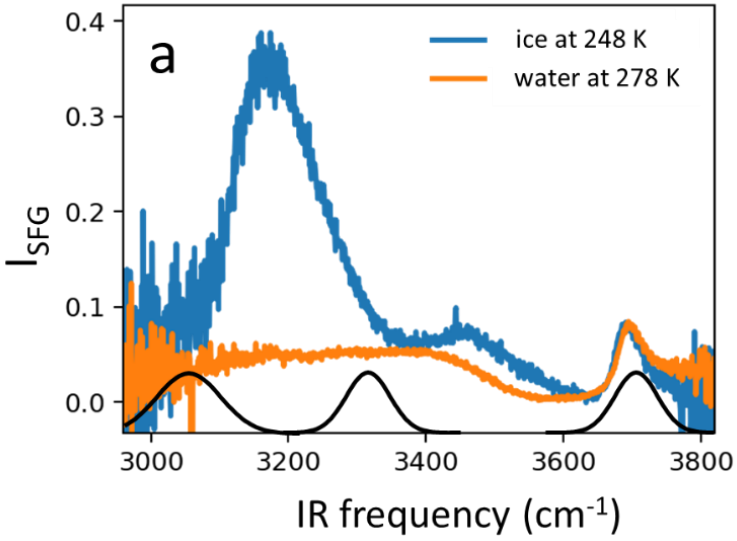

Figure 6.1: Static SFG spectra of ice and water at 248 and 278 K respectively, normalized to the free-OH peak around 3700 cm^{-1}. Shown in black are the excitation pulses for the pump-probe measurements centered at 3050, 3310, and 3700 cm^{-1}.

The vibrational dynamics of interfacial ice have not previously been reported, to the best of our knowledge, owing to the substantial experimental challenge of combining ultrafast surface-sensitive spectroscopy with molecularly-defined single-crystalline ice surfaces. Many studies have reported on vibrational dynamics of bulk ice[111–114] and water[115–120], and vibrational dynamics of interfacial water[110,121–124]. Here, we compare the vibrational dynamics of surface OH groups on single-crystalline hexagonal ice (Ice I_h) oriented to the basal plane with those on water. OH-oscillators are selectively excited using a femtosecond infrared pulse. The effect of excitation is probed using surface-specific femtosecond sum-frequency generation (SFG) spectroscopy. SFG is a second-order nonlinear process, generally generating signal only from the interfacial molecules. Monitoring the relaxation process of excited oscillators provides information on vibrational lifetimes, heat dissipation, and energy transfer mechanisms.

We study both, hydrogen-bonded-OH groups at the surface, and free, dangling-OH groups protruding from the surface into the vapor phase. The fraction of interfacial water molecules with a free-OH group is approximately 0.25 for both ice[125] and water[126]. Free-OH groups at the surface of ice are thought to influence chemical reactivities of adsorbates by preferential adsorption[127], molecular ordering[86], and energy transfer dynamics[84,107]. We find that, going from water to ice, the vibrational dynamics of hydrogen-bonded-OH groups are accelerated, while that of free-OH groups slow down substantially.

Results and Discussion

Figure 6.1 displays the static SFG spectra of water and ice as a function of IR frequency, normalized to the free-OH peak at 3700 cm^{-1}. While the free-OH response is quite similar in its frequency and shape, the

hydrogen-bonded region (3000 to 3600 cm^{-1}) is different. The SFG spectrum of ice in the hydrogen-bonded region is more intense, peaking at ~ 3200 cm^{-1}, while the water spectrum is much broader, peaking around ~ 3400 cm^{-1}. The spectral red-shift for ice compared to water is indicative of stronger hydrogen bonds in ice[128]. The increased SFG intensity can be explained by the OH-oscillators being more ordered due to the inherent arrangement of water molecules in ice crystals, as opposed to water. This ordering and hence the SFG intensity gets stronger with decreasing temperature. The static ice SFG spectrum shown here is in agreement with previous reports[9].

Time-resolved measurements of water and ice

In the time-resolved experiments, ice and water surfaces were excited at two frequencies in the hydrogen-bonded region of the OH-stretch band: 3050 and 3310 cm^{-1} to elucidate if low or high-frequency excitation affects the surface dynamics; and at the free-OH stretch region 3700 cm^{-1} to elucidate dynamics of the free-OH oscillators on ice (black traces in figure 6.1a).

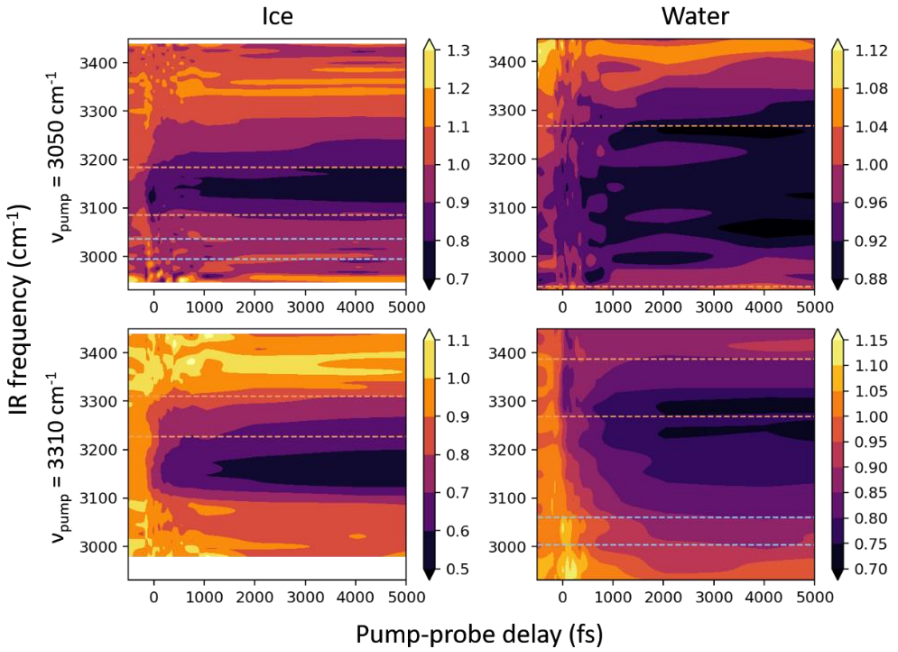

Figure 6.2: Ratio of SFG spectra for ice and water, each excited at v_{exc}=3050 and 3310 cm^{-1}. Orange and sky blue dashed lines represent the spectral region integrated for the ground state bleach (GSB) and the excited state (ES) traces, respectively. Ice is measured at 248 K, and water at 278 K. Although measured at different temperatures, the data can still be compared as it is known from literature[114] that the liquid water dynamics do not significantly depend on temperature, at least from 278 to 300 K. Please note the different z-scale for the different panels. The fine structure for water pumped at 3050 cm^{-1} is caused by noise, resulting from low signal levels. By varying the integration limits, we confirmed that the results are independent of the precise value.

Figure 6.2 shows the ratio of SFG spectra $I_{SFG}^{exc}/I_{SFG}^{ref}$ as a function of delay time after excitation, with I_{SFG}^{exc} and I_{SFG}^{ref} being the SFG spectrum in the presence and absence of the excitation pulse, respectively, for ice (left column) and water (right column) excited at the frequencies 3050 cm^{-1} (first row) and 3310 cm^{-1} (second row). For simplicity, we focus on one of the four plots shown in the figure, which is ice pumped at 3050 cm^{-1}. The initial bleach (ratio <1, indicating depopulation of the ground state) around 3150 cm^{-1} is spectrally narrow and very short-lived. The bleach is accompanied by an apparent excited-state SFG response from the first vibrationally excited state, represented by the positive signal around 3000 cm^{-1}. Upon decay of the vibrational excitation, there is a relatively slow ingrowth of the signal centered around 3175 cm^{-1}, which reflects the dissipation of excess energy over the system.

To quantify the dynamics, we integrate data in figure 6.2 over specific frequency ranges to create traces as a function of pump-probe delay shown in figure 6.3. Choosing individual integration regions for each sample and excitation wavelength is inevitable, due to a) different IR absorption line-shapes and peaking frequencies for ice and water; b) sample-dependent response for the same excitation frequency – maximum bleach being centered at different frequencies for ice and water; c) super-fast spectral diffusion, complicating the designated area of integration further to procure vibrational lifetimes. More generally, ground state bleach regions were chosen to be close to the excitation frequency, incorporating spectral diffusion (movement of bleach signal at early times across spectral range), and also spectral area with high bleach signal.

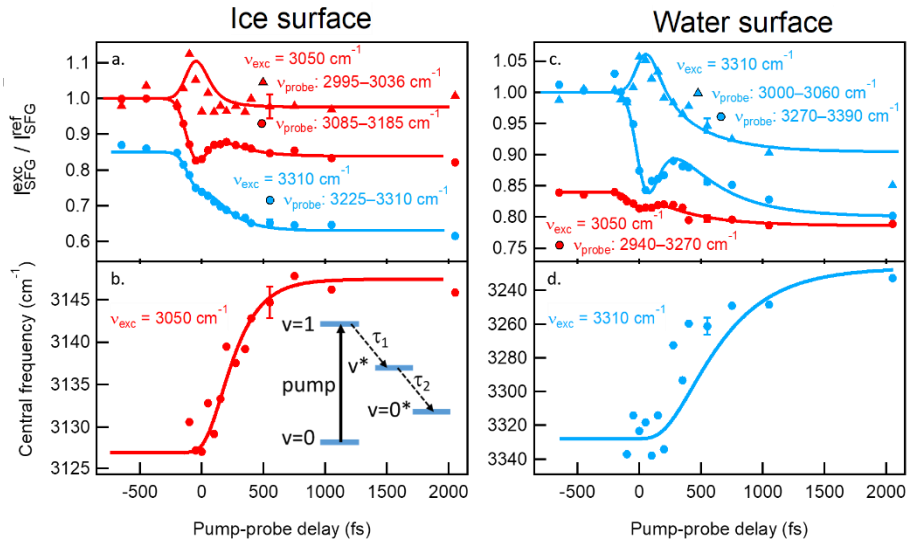

Figure 6.3: Dynamics traces following vibrational excitation of ice (248 K, panels a, b) and water (278 K, panel c, d) surfaces. Data points in red represent ν_{exc}=3050 cm^{-1}; in blue: ν_{exc}=3310 cm^{-1}. Probe frequency range for each system mentioned in legends. Circles in panels a and c show probe traces assigned to ground state bleach; triangles (ν_{exc}=3050 cm^{-1} for ice and ν_{exc}=3310 cm^{-1} for water) show response assigned to excited state SFG. The associated central frequency shift of the SFG response is shown in panels b and d. Datapoint at 2050 fs in panels b and d is an average of later time points, up till 10,500 fs. Inset in panel b depicts the 4-level model used to describe the traces, represented by solid lines. Traces for ice with ν_{exc}=3310 cm^{-1} and water with ν_{exc}=3050 cm^{-1} are offset for clarity. Typical error bars for each plot are shown at 550 fs.

In Figure 6.3, panels a and c show traces for ice (248 K) and water (278 K) respectively excited, at ν_{exc}=3050 cm^{-1} (red) and ν_{exc}=3310 cm^{-1} (blue). The signals integrated close to the respective excitation frequency (filled

circles) demonstrate a sharp decrease around time 0, and are assigned to ground state depletion; the recovery is concurrent with heat effects, which appear already within a few 100 fs. These traces marked by circles in panels a and c will hereafter be called ground-state-bleach (GSB) traces. Ice excited at ν_{exc}=3050 cm^{-1} and water excited at ν_{exc}=3310 cm^{-1} show, in addition, a transient increase in SFG signal at lower frequencies represented by triangles in the upper two panels. This signal is assigned to SFG generated from the first excited state, frequency-shifted by the anharmonicity. The excited state (ES) response for the other excitation frequency could not be detected, probably due to overlap with the bleach and heat signals. The response at the excited state frequency also contains a contribution from the ingrowing heat. Panels b and d show the temporal evolution of the first spectral moment of $I_{SFG}^{exc}/I_{SFG}^{ref}$, obtained from Gaussian fits. These traces highlight relatively slow spectral changes that presumably reflect the ingrowth of heat.

Upon pumping ice at 3050 cm^{-1}, the first spectral moment of $I_{SFG}^{exc}/I_{SFG}^{ref}$ shifts to higher frequency upon relaxation, while it shifts to lower frequency for pumping water at 3310 cm^{-1}. In both cases, the shifts in the OH stretch frequencies are the result of ultrafast heating, following vibrational relaxation; that the direction of the shift is opposite is the result of the spectral position of the excitation pulse below (exciting ice at 3050 cm^{-1}) and above (exciting water at 3300 cm^{-1}) the peak of the $I_{SFG}^{exc}/I_{SFG}^{ref}$ SFG response (respectively, 3150 and 3250). Hence, for ice pumped at low frequencies, the excitation occurs below the main response, and there is an up-shift due to the heating, while for water, there is a down-shift.

Modelling dynamics for the hydrogen-bonded –OH stretch

The observed dynamics are modeled (solid lines, figure 6.3) using the 4-level system, shown in the inset of figure 6.3b[33,129]. Excitation occurs from the ground (v=0) to the first excited (v=1) state. Relaxation with the time constant τ_1 occurs to an intermediate state (v*, possibly the overtone of the bending mode[130,131]), from which relaxation to a heated ground state (v=0*) occurs with a time constant τ_2. Single-pulse excitation triggers a local temperature rise of a few degrees, weakening the hydrogen bonds[128], and thereby reducing and blue-shifting the vibrational response[128]. As can be seen, upon pumping ice at 3050 cm^{-1}, the first spectral moment of $I_{SFG}^{exc}/I_{SFG}^{ref}$ shifts to higher frequency upon relaxation, while it shifts to lower frequency for pumping water at 3310 cm^{-1}. In both cases, the shifts in the OH stretch frequencies are the result of ultrafast heating, following vibrational relaxation; that the direction of the shift is opposite is the result of the spectral position of the excitation pulse below (exciting ice at 3050 cm^{-1}) and above (exciting water at 3300 cm^{-1}) the peak of the $I_{SFG}^{exc}/I_{SFG}^{ref}$ SFG response (respectively, 3150 and 3250). Hence, for ice pumped at low frequencies, the excitation occurs below the main response, and there is an up-shift due to the heating, while for water, there is a down-shift.

The equations used to describe the ground state bleach (GSB_{SFG}), excited-state SFG response (ES_{SFG}), and the thermal effects ($Heat_{SFG}$) are as follows:

$$GSB_{SFG}(t) = \frac{(\,N_0(t) - N_1(t) + N_*(t) + aN_{0*}(t)\,)^2}{N_0(0)^2} \qquad \text{Eq. 6.1}$$

$$ES_{SFG}(t) = (1 + bN_1(t) + cN_{0*}(t))^2 \qquad \text{Eq. 6.2}$$

$$Heat_{SFG}(t) = \frac{dN_{0*}(t)^2}{N_0(0)^2} + offset \qquad \text{Eq. 6.3}$$

a and c are constants scaling the contribution of the heat, b is a normalization constant accounting for the difference in cross-section between the 0-1 and the 1-2 transition. The observed frequency shift is used as a signature of the heated ground state. To model this frequency shift, we scaled and shifted the trace observed in the model by the constant d and an offset.

For each of the four data sets (ice and water pumped at ν_{exc}=3050 and 3310 cm^{-1}), the respective ground state bleach, excited state response, and thermal effects (figures 6.2 b and d), are described using the same set of parameters τ_1 and τ_2. Specifically, the GSB trace includes the population difference of v=0 and v=1, the population of v* and v=0*. The ES trace includes v=1 with a contribution from v=0* (heat). Since the shift of the central frequency (figures 6.2b, 2d) reflects heating, it is modeled with the population of v=0* (heat). τ_2 was fitted globally to all data sets, for ice (180 fs) and water (380 fs). τ_1 was allowed to vary with excitation frequency.

Table 6.1: Inferred lifetimes from the 4-level model used to analyze vibrational dynamics, corresponding to fitting lines in figure 2. Errors reflect variations between different measurements.

	Ice 3050	Water 3050	Ice 3310	Water 3310	Ice 3700	Water 3700
τ_1 (fs)	80±30	60±50	50±30	110±20	2500±600	1150±400
τ_2 (fs)	180±60	380±80	180±60	380±80	–	–

Given the constraints described above, the model describes the data well (lines in figure 6.3). Table 6.1 shows the inferred time constants. The dynamics for the hydrogen-bonded region appear, on average, faster for ice than for water, which can be attributed to stronger intermolecular coupling effects in ice[111]. τ_1 is a measure of the energy relaxation time of the excited oscillators, but will also include spectral diffusion. Within experimental uncertainty, we find no evidence for a frequency dependence of τ_1 for ice, implying relative homogeneity of the hydrogen-bonded OH groups for ice. τ_2 for ice is substantially faster than for water, illustrating highly efficient heat dissipation. Interestingly, τ_2 for interfacial water is very similar to that observed for bulk[33,123], yet τ_2 for interfacial ice is substantially faster than the ~500 fs reported for bulk ice[112].

Dynamics of the free-OH groups

Figure 6.4 shows the vibrational dynamics of the free-OH stretch (spectral feature at ~3700 cm^{-1} in Figure 1a) at both water (replotted from reference[132]) and ice surfaces. Ice was pumped at ~3680 cm^{-1} and probed from 3675 to 3705 cm^{-1}. The free-OH groups are less sensitive to heat effects, owing to the vanishingly small absorption in bulk at this frequency[133]. A simple single exponential decay convoluted with the instrument response function describes the data well (solid lines in figure 6.4 and Table 6.1 for the timescales).

As apparent from the data, the vibrational relaxation of free-OH groups protruding from ice is substantially slower than for water. At first sight, this may appear surprising, given the accelerated vibrational dynamics for ice in the hydrogen-bonded region. The vibrational relaxation of the free-OH groups protruding from liquid water has been shown to take place via the combination of two mechanisms[132,134]: (i) the reorientation of water molecule containing free-OH groups, so that these become hydrogen-bonded; and (ii) intramolecular energy transfer (IET) from the free-OH group to the other OH group in the same water molecule. In both cases, the excitation disappears from the free-OH group.[121,132] Since water molecules in ice form a more rigid structural arrangement compared to water, the first mechanism involving reorientation of the water molecule is expected to be suppressed for ice. IET in ice should also slow down, owing to the larger frequency mismatch between the free-OH and the hydrogen-bonded OH within the same molecule for ice[125]

(3690 to 3350 cm^{-1}) compared to water[135] (3700 to 3510 cm^{-1}). The suppression of reorientation due to structural rigidity and slow-down of IET result in substantially slower free-OH dynamics for ice.

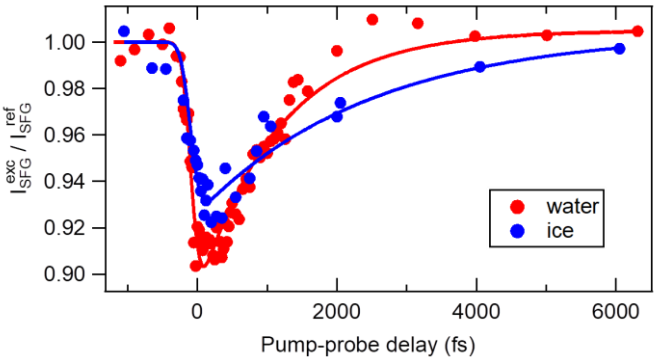

Figure 6.4: Vibrational dynamics at the free-OH frequency. Traces were obtained by exciting and probing the ice (blue) and water (red) surfaces at 3700 cm^{-1}. Lines are single-exponential decays convoluted with the instrument response function.

Conclusions

In conclusion, we have reported ultrafast vibrational dynamics of the ice interface. This study paves the way to time-resolved studies using optical or UV excitation to initiate surface photochemistry, and follow the subsequent dynamics in real-time. The vibrational dynamics of water molecules at the surface of ice are faster or slower compared to liquid water, depending on whether the hydrogen-bonded or dangling-OH groups are considered. The ordered crystalline arrangement of water molecules in ice promotes strong inter- and intra-molecular coupling, making energy transfer in the bonded-OH stretch region extremely fast. This efficient energy transport from the bonded-OH groups into the bulk ice crystal, is potentially relevant for the dissipation of adsorbed (OH-bonded) reactants at the ice surface. In contrast, the dangling-OH shows much slower dynamics for ice compared to liquid water, due to the structural rigidity of ice. The long vibrational lifetime of free-OH groups reflects their long physical lifetime, offering a potential explanation for kinetic trapping mechanisms[136] on the surface of ice, and for the isolation of reaction intermediates and preferential stabilization of charged species on the surface[137]. Differences in binding mechanism[127] and vibrational relaxation rates may account for differences in photochemical reactions on the surfaces of ice and water[138,139].

Chapter 7

Molecular Structure versus Structural Order: Understanding Heterogeneous Ice Nucleation

This chapter is based on collaborative work between the Max Planck Institute for Polymer Research, the Max Planck Institute for Chemistry, and the University of Warwick. The manuscript was majorly compiled and written by Gabriele Sosso, and this chapter is an adaption of the manuscript in major parts.

ABSTRACT: Water remains supercooled at much lower temperatures than the melting point, and only starts nucleating to form ice at ~233 K, a process called homogeneous nucleation. Ice formation typically almost always occurs at higher temperatures, owing to the presence of ice-nucleating agents, that lower the free energy cost of creating large enough ice nuclei. These INAs range from biological fragments of bacteria to mineral dust, and form ice via heterogeneous nucleation. The molecular structure, as well as the extent of structural order within the INA, both play an essential role in determining its effectiveness. Disentangling the two contributions has been a major challenge both experimentally and theoretically. In this work, we have systematically investigated the ice nucleating ability of cholesterol, from its ordered crystalline form to disordered self-assembled monolayers: thus changing the order while maintaining the same molecular structure. Utilizing a combination of experimental methods and simulations, we find that the degree of order plays a much more critical role than molecular structure in determining the extent to which an INA can facilitate ice nucleation. These findings, besides providing a novel perspective on the fundamental problem of ice nucleation, also have practical implications for the rational design of synthetic ice-nucleating agents, particularly those harnessed from biological materials.

Introduction

The phase transition of supercooled liquid water to ice is one of the most important ones, playing a role in global phenomena like climate change[140–142], and having key implications in transformative medical

treatments such a regenerative medicine[143–146], as biological materials are stored using cryopreservation protocols where control over the extent of ice formation in cells is essential. Besides a few exceptions, ice almost always forms at temperatures higher than that of homogeneous ice nucleation temperature ~233 K due to the presence of impurities, which lower the free energy cost of creating ice nuclei large enough to grow into an actual ice crystal[140,147]. This process is called heterogeneous nucleation, and is facilitated by impurities ranging from mineral dust[140,148–150] to bacterial fragments[151–155]. The mechanism behind the facilitation effective nucleation by these substances is still unclear.

Recently, both simulations and experiments in this regime have made substantial progress[147,149,164–168,156–163]. Recent studies suggest that the activity of an ice-nucleating agent (INA) might be an interplay between its inherent order (like crystallinity, presence of defects, or a long-range ordered nature), and its molecular structure, particularly the presence of certain functional groups like the hydroxyl –OH group[169–173]. Which of the two characteristics – molecular functionality or the degree of order – is most important is still unknown, and the disentanglement of the two contributions has been challenging for both experimental and simulation studies[147,173]. Most often, the effectiveness of the different materials is compared, without insight into differences of the contributing effects of molecular structure and order. In this study, we aim to answer this question by probing the ice-nucleating activity of the same substance – cholesterol (CHL), in different forms – crystalline[174], and self-assembled monolayers[175,176], characterized by a variable degree of order and flexibility. Probing its two different phases, we can investigate the role of order, while maintaining the same exact molecular structure – thus being able to assess which of the two effects plays a more prominent role in heterogeneous ice nucleation.

Bringing together experimental approaches like Sum Frequency Generation Spectroscopy (SFG), and Ice-Nucleation Freeze assays, and atomistic computer simulations, we find that the ice-nucleating activity of the CHL monolayers are weaker than that of its crystalline phase. A detailed systematic investigation of different coverages of CHL monolayers, characterizing different degrees of structural order and flexibility, reveals that the degree of order of the monolayers translates into the structuring of interfacial water molecules, which in turn directly impacts the population of pre-critical ice nuclei forming at the CHL-water interface. Hence we can argue that in this case, order outweighs molecular structure, as ordering of the monolayer has a tremendous impact on the ice-nucleating activity. Steroids of a similar structure as cholesterol, but varying in crystal size type and dimensions have been reported to show equally-strong ice-nucleating ability[177,178].

Our systematic investigation of the impact of order and disorder on the ice-nucleating ability of a biologically-relevant compound, allows us to unravel the microscopic mechanisms underpinning the ice-nucleating activity, and hence offer valuable guidelines towards rational designing of next-generations INAs. Particularly, our results imply that the supra-molecular aspects of biological INAs should be more emphasized opposed to the molecular structure.

Method section

Droplet freezing assays

Freezing experiments of the CHL monolayer were performed using the high-throughput Twinplate Ice Nucleation Assay (TINA)[179]. Droplets of pure water (30 µL volume) were pipetted into sterile 384-well plates (Eppendorf, Hamburg, Germany) by a liquid handling station (epMotion ep5073, Eppendorf). Pure water was prepared as described earlier[179]. To obtain monolayers of CHL on top of the pure water droplets, 1 µL aliquots

of CHL in chloroform at different concentrations were pipetted on top of the pure water droplets using a liquid handling station. The concentration of the solutions ranged from 0.046 mM to 4.69 mM, corresponding to a surface area ranging from 400 Å^2/molecule to 4 Å^2/molecule, respectively. Of each concentration, 96 droplets were measured, and experiments were performed from 0 °C to -30 °C at a cooling rate of 1°C /min. The temperature uncertainty was 0.2 °C. As controls, 30 µL droplets of pure water, and 30 µL droplets of pure water with 1 µL droplets of pure chloroform were measured. From the fraction of total droplets frozen, we have computed the cumulative number of nucleation sites per cholesterol molecule, referred to as n_s, which allows us to compare the ice-nucleating ability of the different CHL monolayers with that of CHL crystals. The higher the value of n_s, the stronger the ice nucleation activity of the sample (per molecule). Confidence intervals were calculated using Monte Carlo simulations[180], based on the assumption that the number of freezing events in a temperature interval is expected to follow a Poisson distribution. For each experiment, the data was divided into temperature intervals of 0.5 K width. The observed number of events in each temperature interval was taken as the expectation value for the number of events, and 1000 Poisson distributed random numbers were generated for each temperature interval. This effectively gives 1000 independent possible experimental outcomes, which were used to calculate possible n_s values. The confidence intervals are the 10th to 90th percentile range of the simulated values. Due to the relatively high number of droplets used in these experiments the confidence interval is relatively narrow.

Molecular Dynamics Simulations

Cholesterol and water molecules were both modelled at the atomistic level via the CHARMM36 force field[181,182] and the TIP4P/Ice[183] model, respectively. This specific combination has been validated on multiple occasions within the recent literature: not only has it been demonstrated to provide an accurate description of supercooled water and ice at the interface with biological material[184–186], but we have also explicitly verified its reliability for water and ice in contact with cholesterol[172]. The GROMACS package (version 5.1.4.)[187] has been used to perform molecular dynamics (MD) simulations within a variety of ensembles, including the NT ensemble (with constant surface tension)[188] so as to take into account different CHL coverages (i.e., different values of surface area per molecule, S_A/mol). A leap-frog algorithm[189] has been used to integrate Newton's equations of motion with a time step of 2 fs. A twin cutoff of 12 Å has been used for both electrostatic and van der Waals interactions, where, for the latter, forces have been smoothly switched to zero between 10 and 12 Å. The Bussi-Donadio-Parrinello thermostat[190] has been used to sample the canonical ensemble, in conjunction with the Berendsen barostat (in a semi-isotropic fashion given the slab geometry)[191] if performing simulations in the NPT or NT ensemble. The coupling constants for the thermostat and barostat are 0.5/1.0 (CHL/water) and 4.0 ps, respectively. The LINCS[192] and SETTLE[193] algorithms have been used to constrain the CHL bonds involving hydrogen atoms and to enforce the geometry of water molecules, respectively.

To simulate self-assembled CHL monolayers at the interface with water, we have used the setup depicted in Fig. 2a: the symmetry of the system along its z-axis (parallel to the long edge of the simulation box which has been extended according to the mentioned guidelines[194]) is such that it eliminates spurious electrostatic effects due to the intrinsic dipole moment of CHL molecules. 2D periodic boundaries conditions have been employed to deal with this slablike computational setup, in conjunction with the Bostick and Berkowitz Ewald summation scheme[194]. We have also considered a setup involving a single layer of CHL molecules, a situation that might be problematic because of spurious effects related to nonphysical electric fields within the simulation box, however, the results are perfectly consistent with the setup featuring two layers of CHL molecules in contact with the upper and lower part of the water slab - the thickness of which is enough to

guarantee bulk-like structural properties of water within the middle of it. Different coverages of CHL self-assembled monolayers were achieved as follows: 64 CHL molecules were randomly positions at a distance of 3 Å from a water slab equilibrated within the NPT ensemble at ambient temperature and pressure. The minimum distance between the CHL molecules in the xy-plane was 5 Å. A series of NΥT simulations enforcing different values of Υ were then performed to gradually increase the S_A/mol - we are thus computing surface pressure vs. area isotherms via a compression protocol. Each of these simulations lasted a minimum of 50 ns, which we have verified is sufficiently long to converge the structural properties of the system at room temperature.

NVT simulations were performed at selected values of S_A/mol in order to eliminate the effect of pressure fluctuations: after 50 ns of equilibration, each configuration has been quenched from 300 to 230 K in 50 ns following a linear quenching protocol. These configurations have finally been used as the starting point for the long (~1.4 μs) production runs used to obtain the results reported in this work to study the formation of ice nuclei. We note that we validated this quenching protocol in Ref. 33, where we also pinpointed 230 K as the ideal supercooling to investigate icy water for the TIP4P/Ice water model. Molecules belonging to ice nuclei have been identified thanks to a clustering algorithm based on the local order parameter introduced by Wang et al.[195], which in turn leverages the so-called Steinhardt order parameters[196].

Sum Frequency Generation Spectroscopy

SFG setup: The SFG experiments were performed using a Ti-Saph regenerative amplifier setup (Spitfire Pro, Spectra-Physics) generating 800 nm pulses with a repetition rate of 1 kHz and a duration of ~40 fs. Part of the output was used to generate broadband infrared pulses in an optical parametric amplifier (TOPAS-C, Light Conversion) with subsequent difference frequency generation. The IR pulse energy at the sample was approximately 3 μJ. The other part of the laser output was spectrally narrowed to 15 cm^{-1} using a Fabry-Perot etalon. The resulting 800 nm beam had a pulse energy of 20 μJ. All sample spectra were collected in SSP (SFG-Visible-IR) polarization with incident angles of 34° and 36° for the visible and IR beam, respectively. To reduce heating effects from the laser, the trough containing the CHL monolayer on water was rotated[197]. To prevent oxidation during the experiment, the sample area was purged with nitrogen. The sample SFG spectra were divided by an SFG spectrum from z-quartz spectra to account for the IR laser pulse spectral content. All spectra were acquired for 10 minutes.

Sample Preparation: For the SFG experiments, CHL (Sigma Aldrich) was dissolved in chloroform to a concentration of 0.64 mM; all solutions were prepared in a glove box to avoid sample oxidation. To form a monolayer on water, a well-defined number of drops were deposited onto the water surface to get a specific surface coverage (calculated using the trough surface area and number of molecules in a drop), using a microliter syringe (from Hamilton) with a droplet size of 0.5 μl. The surface pressure was monitored throughout the experiment using a Kibron surface tensiometer. The CHL layer was monitored via Brewster Angle Microscopy as well.

Results and Discussion

Comparison of the ice-nucleating ability of monolayers and crystals

Droplet freezing assays is a commonly used method to provide quantitative information on the ice-nucleating activities of substances. Figure 1 displays the cumulative number of ice-nucleating sites, n_s, for CHL crystals[172] and for self-assembled CHL monolayers of varying coverages characterized by S_A/mol values. n_s is a measure of the nucleating activity per molecule, and a higher value of n_s denotes stronger ice-nucleation activity of the sample (more in Methods section). Clearly from Figure 1, the two phases of CHL show different ice-nucleation activities, the crystalline phase having a much higher potency than the self-assembled monolayer.

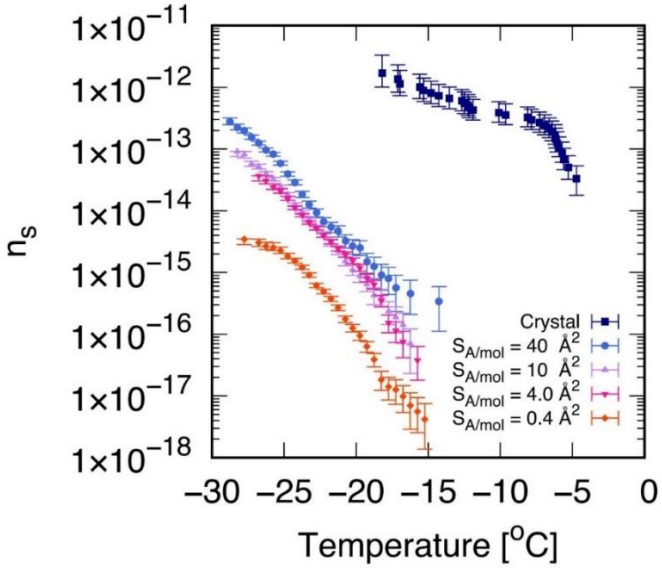

Figure 7.1: Cholesterol crystals are much more active ice-nucleating agents than cholesterol monolayers. Cumulative number of nucleation sites (n_s) as a function of temperature, measured via droplet fraction frozen experiments for CHL monohydrate crystals as well as for self-assembled CHL monolayers characterised by different values of surface area per molecule, S_A/mol. The volume of the water droplets in contact with CHL crystals and monolayers is 1 µl and 30 µl, respectively. The uncertainty, in terms of temperature, associated with the data for CHL crystals and monolayers is 0.4 and 0.2 K, respectively.

The crystalline phase, despite being clearly more efficient, also shows a two-step trend, whereas the monolayers display a more homogeneous, broad growth. The two-step trend for the crystalline form is largely because of different nucleation sites on the surface of CHL crystals that are active at different temperatures. The monolayers however do not have specific nucleation sites as the monolayer-water interface is very homogeneous with no defect states as opposed to the crystalline surfaces. The monolayer

interfaces thus offer a well-defined substrate for ice nucleation to occur, whereas the crystalline form offers a diverse variety of nucleation sites, also typical of other crystalline INAs[149,198,199].

Moreover, the ice-nucleating activity of CHL monolayers is dependent on the coverage. Surface coverage would be inversely proportional to the S_A/mol quantity. In Figure 7.1, a very high coverage of the CHL monolayer, i.e. at 0.4 Å/molecule, displays an almost negligible ice-nucleating ability. This coverage corresponds to a regime where the concentration of CHL molecules on the surface is high, and the CHL monolayers have collapsed[200] (also reported by MD simulations). At a lower coverage of 4 Å^2/molecule, the ice-nucleation activity increases, and appears very similar to that at 10 Å^2/molecule. The 40 Å^2/molecule case does indeed show slightly still better activity. At this coverage, an intact monolayer is present at the interface, as seen by the sharp rise in the pressure isotherm of cholesterol displayed in Figure 7.2. Despite the high ice-nucleation activity seen for the 10 and 40 Å^2/molecule surface coverages, the distinction from the background curves was not a clear process. Eliminating background effects is in general a challenging process with droplet freeze assays[201,202], in particular when dealing with substances displaying relatively weak ice-nucleation effects, like CHL monolayers.

Therefore, given the limited resolution of the droplet freeze assays, we probed a range of S_A/mol coverages using both SFG experiments and MD simulations, to assess if there is a 'sweet spot' in terms of the ice-nucleation activity. Such a sweet spot does indeed exist, attributed to the microscopic structure of monolayers at different coverages, as illustrated in the next section.

The structural order of CHL monolayers depends strongly on its coverage

We now focus on the degree of order within the CHL monolayers characterized by its surface pressure or S_A/mol values, and its influence on the ice-nucleation activity. Firstly, we investigated the surface pressure of CHL monolayer – water interface as a function of surface area per molecule S_A/mol. The computational setup is depicted in Figure 7.2a, which involves two CHL monolayers at the top and bottom of a slab of water. The result from the MD simulations for the surface pressure is depicted in Figure 7.2c in blue, along with the experimentally measured data depicted in yellow. The experimental results are consistent with previously measured pressure isotherms of cholesterol on water[200]. Also, the simulation data are in excellent qualitative agreement with the experimental measurements. There is a slight overestimation of the absolute values of surface pressure in the simulation data, owing to the relatively small size of simulation box, however the discrepancies are very small. Both experiments and simulations point towards ~40 Å/molecule as a critical value, below which the surface pressure sharply increases. This value denotes the formation of an increasingly compact monolayer, before the monolayer collapses, and has been reported experimentally before[175,176,203,204]. The MD simulations show a structural collapse < 30 Å/molecule, and the mismatch can be attributed to the formation of bi- and multi-layers in the experiment before collapse. Also, the range of S_A/mol in Figure 7.2 c,d correspond to coverages yielding very similar ice-nucleation activity measured via droplet freeze assay, thereby showcasing the molecular-level resolution achievable. Moreover, both experiments and simulations identify negative surface pressure values in the high range. This could be an indication of metastability, wherein the CHL molecules are repelled by the interface to an extent, also reported for low coverages of other lipids, proteins and polymers[205–207], but not CHL before; or could be an artefact as seen under some conditions also without CHL, due to evaporation in experiments, and finite size effects and surface tension mismatch in the simulations.

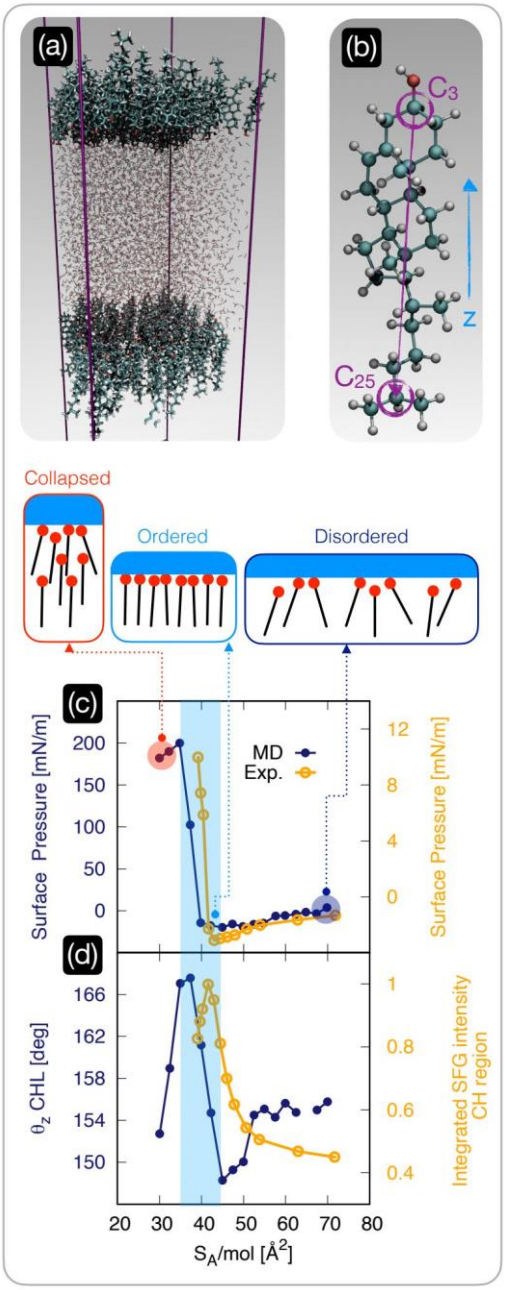

Figure 7.2: The structure of cholesterol monolayers dramatically changes as a function of surface pressure. (a) A representative snapshot of a molecular dynamics simulation used to model self-assembled cholesterol monolayers in contact with water: the hydrophilic heads of the cholesterol molecules within two monolayers point toward the water phase. (b) Atomistic model of a cholesterol molecule: the vector connecting the C_{25} to the C_3 carbon atoms forms an angle θ_z with the z-axis of the simulation box; carbon, hydrogen and oxygen atoms are depicted in light blue, white and red, respectively. (c) Surface pressure (from molecular dynamics simulations, "MD" [blue] and experimentally measured surface tension, "Exp" [yellow] as a function of surface area per molecule S_A/mol; the region of the plot shaded in light blue highlights the sharp rise in the surface pressure below a critical value of S_A/mol, beyond which the monolayer collapses. (d) The θ_z angle defined in panel (b) (from molecular dynamics simulations [blue]) and the experimentally measured square root of the integrated intensity of the sum-frequency generation spectroscopy signal corresponding to the C-H stretch region [yellow]; the same shaded region defined in panel (c) highlights the abrupt ordering of the cholesterol molecules within the monolayer in a specific interval of S_A/mol.

To understand potential structural changes in the layer, one has to first define a molecular axis for CHL molecules, as depicted in Figure 7.2b. It is defined as the vector connecting the C_{25} and C_3 carbon atoms, and θ_z is defined as the angle between the C_{25} - C_3 molecular axis and the z-axis of the simulation box (perpendicular to the CHL-water interface). From Figure 7.2d, the region with S_A/mol = 35-45 Å^2 shaded in blue corresponds to compact monolayers, having a higher degree of structural order compared to the region with higher S_A/mol values. This is demonstrated by the high θ_z average value in this region, indicating that the molecular axes of CHL molecules are on average more perpendicular to the surface, making this surface coverage region 'optimal.'

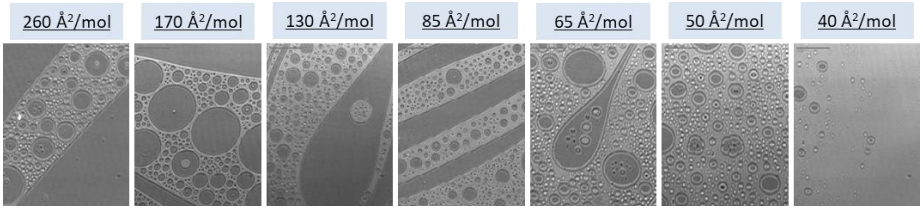

Figure 7.3: Brewster Angle Microscopy (BAM) images of cholesterol over water for varying surface coverages

To unravel the overall structure of CHL molecules as a function of surface coverage, we first perform Brewster Angle Microscopy (BAM), which enables visualization of monolayers at the air-water interface; images for different coverages are shown in Figure 7.3. A p-polarized light beam is sent to the air-water interface, at the Brewster angle of water, 53°. Bare water surface shows as dark areas due to no reflection of light, and monolayers show in a brighter form depending on the changed refractive index with the added sample. The images reported in Figure 7.3 confirm the increasing coverage of the CHL molecules on the surface of water going from left to right, and a very homogeneous coverage around 40 Å^2/molecule.

For more quantitative information, we performed SFG experiments of CHL on water, to observe intensity variation in the –CH and –OH regions at varying surface coverages. The SFG spectra for S_A/mol varying from 71.6 Å^2 to 38.5 Å^2 are shown in Figure 7.4. SFG intensity is plotted as a function of the IR frequency in wavenumbers.

From Figure 7.4, there is a relatively strong signal seen in the frequency region centred around 2900 cm^{-1}. The region from 2700 to 2850 cm^{-1} is generally associated to aldehyde or ketonic groups, and from 2850 to 3100 cm^{-1} is associated to CH_3, CH_2, or CH stretch modes. The OH vibrational stretch covers a broad range from 3000 to 3700 cm^{-1}. The SFG intensity in the –CH region increases sharply from higher S_A/mol up to an optimal surface concentration of cholesterol, ~40 Å^2. SFG intensity being maximum at this density corresponds to densely-packed ordered CHL molecules on the surface, in agreement with the very homogeneous surface seen in the BAM images at 40 Å^2. Moreover, this value closely aligns with the monolayer formation point of CHL molecules, as seen from the surface pressure Figure 7.2 c. At S_A/mol lower than 40 Å^2, the SFG intensity in the –CH region declines again, pointing towards monolayer disruption or formation of multiple layers, and hence a decrease in the structural order. SFG intensity in the –OH region show a similar trend, although difficult to observe against the super-strong –CH signals.

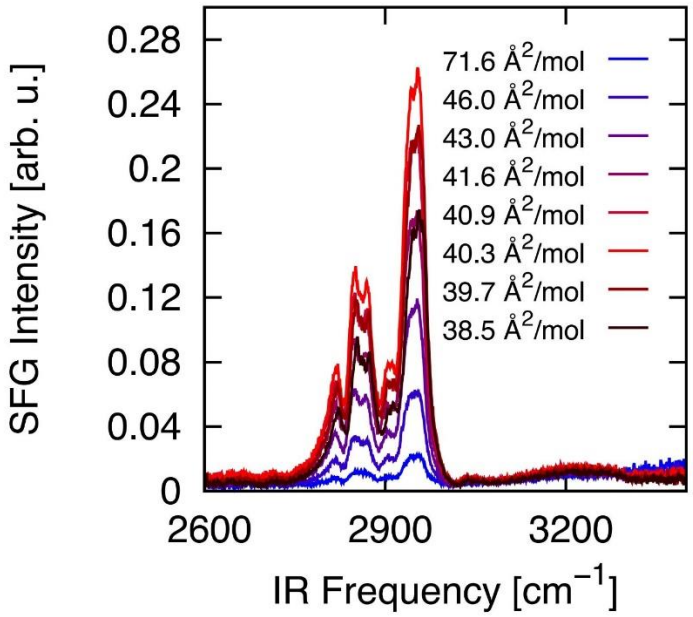

Figure 7.4: SFG spectra for various CHL coverages. The intensity of the SFG signal is anti-correlated with the decrease of the S_A/mol until it reaches the sweet spot around 40 Å^2/molecule, below which the SFG intensity reduces.

The integrated SFG signal corresponding to the –CH region in the spectral range 2750 – 3050 cm^{-1} as a function of the S_A/mol is depicted in Figure 7.2 d. Maximum collective alignment of the CHL molecules takes place for S_A/mol values within the shaded blue region in the figure corresponding to highly structured compact monolayers, as described above. Interestingly, from the MD simulations, the surface of interest for CHL crystals is characterized by S_A/mol = 38.44 Å^2, thus suggesting that indeed the range 35-45 Å^2 might correspond to the most efficient packing density, depicted in Figure 7.2 d in dark blue. This result from MD simulations further supports the SFG spectroscopy measurements. At this stage, the key question is whether the structure of the CHL monolayers characterized by the degree of order, has a direct impact on the ice-nucleation activity. We investigate on this in the next section.

Microscopic insight into the formation of ice nuclei

From the previous section we concluded that the degree of order of the CHL monolayer highly depends on the surface area per molecule. The MD simulations reveal that these structural changes in the CHL monolayers translate into formation of pre-critical ice nuclei of different propensities at the CHL-water interface. This is illustrated in Figure 7.5. Particularly, we report the probability density P(COMz) of the z-coordinate of the centre of mass of the largest ice nucleus found in each configuration generated using 0.5 µs long MD simulations. The peak positions corresponding to increase in nuclei population at the CHL-water interface have been aligned to zero. The distributions have been normalized so that the baseline

corresponding to the nuclei population within the bulk of the water slab is equal to one. From the figure, the CHL crystals display a strong tendency to form ice nuclei at the CHL-water interface (shaded area) compared to the bulk, with a P(COMz-Max) ten times higher in the interfacial region. For CHL monolayers, the tendency for the nuclei to occur at the CHL-water interface is dependent on the S_A/mol. For S_A/mol = 40 Å^2 corresponding to highly ordered CHL monolayers, there is a significant propensity for the ice nuclei to form at the ice-water interface, in comparison to lower or higher values of S_A/mol corresponding to disordered layers beyond the threshold collapse, and disordered layers due to sparsity.

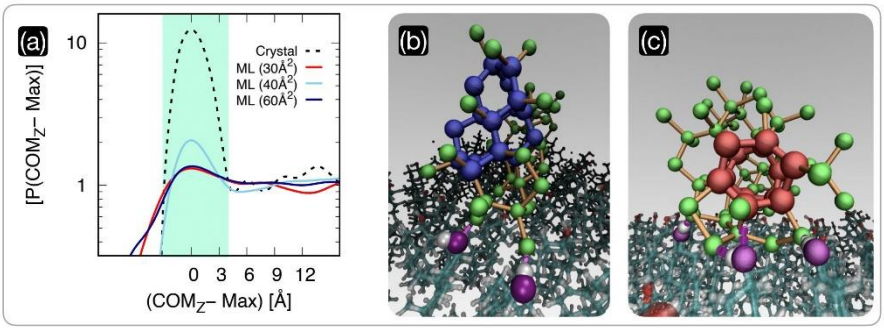

Figure 7.5: The population of pre-critical ice nuclei changes according to the structure of the cholesterol surface. (a) Probability density P(COM$_Z$) of the z-coordinate of the center of mass of the largest nucleus found in each CHL-water configuration generated by means of long (0.5 μs) MD simulations. The positions of the peaks of these distributions, corresponding to the increase in the nuclei population at the CHL-water interface, have been aligned to zero. The distributions have also been normalized so that the baseline corresponding to the population of nuclei within the bulk of the water slab is equal to one. We report results for water on a CHL crystal and on three CHL monolayers characterized by S_A/mol=30, 40 and 60 Å2. The light green shaded region qualitatively highlights the width of the CHL-water interface. (b) and (c) representative snapshots of pre-critical ice nuclei at the CHL-water interface (taken from an MD simulation of the S_A/mol=40Å2 system): double-diamond and hexagonal cages (see text) are highlighted in blue and red, respectively. Oxygen atoms belonging to ice nuclei and their interatomic bonds are depicted in green and orange, respectively. The oxygen belonging to the CHL -OH groups hydrogen-bonded with the ice nuclei are highlighted in purple.

The results thus indicate, that the analysis of the pre-critical nuclei[208] population is predictive of ice nucleation ability of the different systems considered. As already pointed out in Figure 7.1, CHL crystals are more active ice-nucleating agents than CHL monolayers, and this difference is very consistently reproduced by the data in Figure 7.5a. While frozen droplet assays, because of their relative potency could not assess the differences between the ice-nucleation activity of CHL monolayers of varying coverages, the MD simulations pinpoint a specific range of S_A/mol where CHL layers are most active. This sweet spot is at S_A/mol = 40 Å^2, that lies in between low-coverage (high S_A/mol) and collapsed (low S_A/mol) regions, highlighting the correlation between the degree of order within the monolayer and its ice-nucleating ability.

Interestingly, the examination of the nature of pre-critical nuclei in the supercooled regime considered in the MD simulations, pointed out the coexistence of cubic and hexagonal ice nuclei, potentially indicating towards the formation of stacking disordered ice[209–211]. As shown in Figures 7.5b and 7.5c, the building blocks of cubic and hexagonal ice, being double-diamond cages (DDCs) and hexagonal cages (HCs) respectively[212], can form at the CHL-water interface aided by hydrogen bonding between water and hydrophilic CHL head groups. The –OH groups of CHL, being amphiphilic in nature, can both donate and accept hydrogen bonds, and are directly the sites where ice nuclei form. This is in contrast to reports of certain ice-nucleating proteins, where

a layer of 'structured' water acts as a template upon which the ice nuclei grow[155,213]. The presence of amphiphilic –OH groups seems to facilitate ice nucleation for CHL monolayers in a similar fashion to what was reported for CHL crystals[172], where also the emergence of both cubic and hexagonal ice was observed.

The structuring of water determined from experiments and simulations

From the previous section, we have seen that CHL monolayers corresponding to the S_A/mol where the cholesterol molecules are more ordered, have a strong ice-nucleating ability; which however is still inferior compared to CHL crystals (see Figure 7.1). The microscopic mechanism underpinning the ice-nucleation activity behind the ordering of the monolayers, lies in the structuring of water molecules at the CHL-water interface, as shown in Figure 7.6. From the MD simulations, the average angle of the –OH fragments of both the water and the cholesterol molecules to the z-axis of the simulation box, can be computed for different S_A/mol values (Figure 7.6a). The extent of the CHL-water interface chosen to define 'interfacial water', was for oxygen atoms within ~7 Å^2, to also be able to compare analysis to previous work done on CHL crystals[172]. Besides, it was verified that results for the range 5 – 10 Å^2 were consistent.

The θ_z values obtained from the MD simulations are compared to the experimentally-measured signal. The SFG signal for the –OH groups cannot be differentiated for the CHL or the water molecules. The simulation data interestingly, allow disentanglement of the contributions of –OH fragments belonging to either water or CHL molecules. From the comparison displayed in Figure 7.6a, while $\theta_z(\mu_{OH}^{CHL})$ displays only a marginal variation as a function of S_A/mol, $\theta_z(\mu_{OH}^{Water})$ shows a sharp increase in the CHL-ordered region. This trend is in excellent agreement with the experimental data, where the SFG intensity of the –OH region is integrated (from spectra displayed in Figure 7.4) and displayed as a function of S_A/mol (Figure 7.6a in pink). This demonstrates that the increase in SFG signal is indeed due to ordering of interfacial water as the CHL monolayers become more ordered.

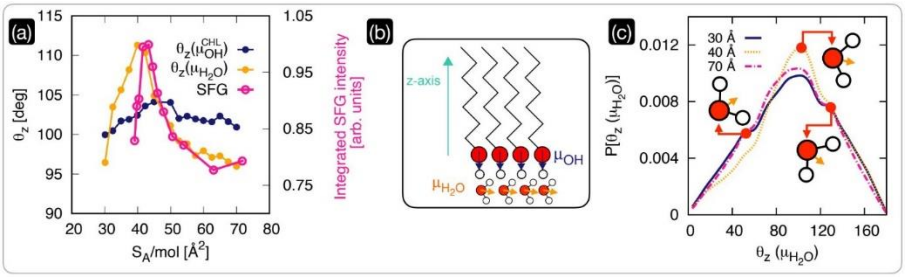

Figure 7.6: The structuring of interfacial water underpins the ice-nucleating abilities of cholesterol monolayers. (a) Comparison of the average orientation of the dipole moments (see panel (b)) of CHL $\theta_z(\mu_{OH}^{CHL})$ and water molecules as obtained via MD simulations with the square root of the integrated intensity of the experimental SFG signal in the -OH spectral region. (b) Schematics of the dipole moments of CHL and water defined with respect to the z-axis of the MD simulation box. (c) Probability density of the dipole moment for interfacial water molecules (P[$\theta_z(\mu_{Water})$], see text for the definition) at low and high coverage (S_A/mol = 70 and 30 Å^2, respectively), compared with the result obtained for a value of S_A/mol (40 Å^2) corresponding to the highly ordered region of CHL highlighted in Fig. 2; representative orientations of the water molecules are included as insets.

Through the MD simulations, we can also investigate the changes in the orientation of interfacial water at different coverages of CHL. As before, the results for the orientation at S_A/mol = 40 Å^2 corresponding to a highly ordered CHL monolayer are compared to S_A/mol = 30 Å^2 and S_A/mol = 70 Å, the high and low coverages respectively (see Figure 7.2). As shown in Figure 7.6c, on average the interfacial water molecules tend to align on top of the CHL monolayers in a configuration $\theta_z(\mu_{Water})\sim 102°$, where one of the hydrogen atoms points towards the CHL surface, leaving the oxygen atom available to hydrogen-bond with an –OH group of the CHL. A similar configuration provides a shoulder in the probability density at $\theta_z(\mu_{Water})\sim 130°$, which remains unchanged with the value of S_A/mol. However, the population feature at $\theta_z(\mu_{Water})\sim 55°$, substantially decreases for CHL coverages corresponding to the highly ordered region. Therefore, the highly ordered CHL monolayer has a higher probability to have its water molecules in the $\theta_z(\mu_{Water})\sim 120°$ configuration, and a lower probability to find them in the $\theta_z(\mu_{Water})\sim 55°$ configuration. This subtle change in the specific S_A/mol interval of CHL monolayers orders interfacial water to an extent to trigger ice nucleation.

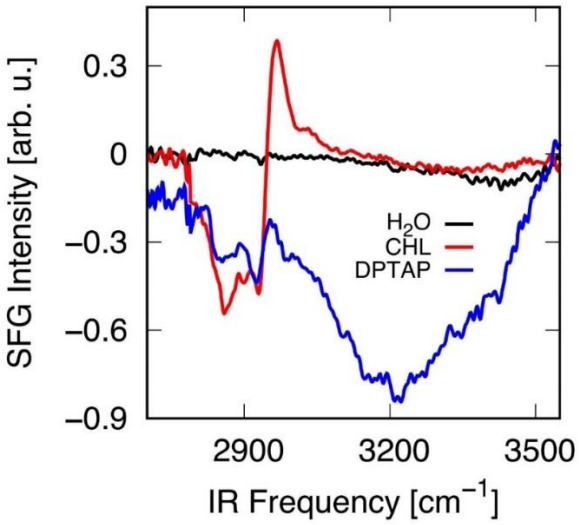

Figure 7.7: Phase-resolved SFG measurements. Imaginary $\chi^{(2)}$ spectra of pure water (black), CHL monolayer on water (red) and DPTAP (blue). As it concerns the CHL spectrum, alkyl chains point away from the water; the intensity in the OH region decreases compared to pure water.

Figure 7.6c shows the average angle of the ordered CHL monolayer to be above 90°. This result from simulations can be experimentally verified as well, by performing phase-resolved SFG spectroscopy. The imaginary $\chi^{(2)}$ spectrum obtained via phase-resolved SFG measurements is indicative of the orientation of the measured sample in reference to the orientation of the known sample. The reference sample we used is a monolayer of DPTAP, which is a long-chain alkyl lipid, positively charged, and hence strongly aligns the water molecules. Figure 7.7 shows the imaginary $\chi^{(2)}$ spectra of the DPTAP sample in blue, which gives a very strong negative peak in the –OH signal, corresponding to the –OH group pointing down, due to the positive charge of the lipid at the interface. The negative peak in the –CH region for DPTAP signifies the alkyl chains pointing up, originating from the –CH_2 and –CH_3 symmetric stretches. The phase-resolved spectrum

of CHL on water, represented in red has a lower intensity in the –OH region compared to water (in black). The negative signal indicates on average a downward pointing dipole, which is in good agreement with Figure 7.6c, showing that the average angle is above 90°.

This sweet-spot in terms of ice-nucleating ability cannot be detected with the frozen droplet assays, reported in Figure 1, as the activity of CHL monolayers is still relatively weak within the relevant range of S_A/mol. However, both the MD simulations and the SFG experiments successfully identify this subtle trend. Clearly, the CHL molecules have a higher degree of order and packing in its crystalline phase, which translates into being able to structure interfacial molecules better, and the ice nucleation activity being better than CHL molecules in its most ordered monolayer form. These results are consistent also with a very recent computational work[214] on phloroglucinol dehydrate monolayers, where the structuring of interfacial water determines whether ice nucleation follows classical nucleation theory or a two-step mechanism instead[147].

Conclusions

The freezing of water into ice is, as its very core, a question of which particular impurity can facilitate heterogeneous ice nucleation and how. Recent evidence suggests that amongst the different microscopic factors playing a role in this process, the interplay between the molecular structure and the degree of order of an impurity might be the key[169–173]. However, it is not clear if the molecular structure outweighs the order, or the other way around. This is primarily because disentangling the two effects is a very challenging task for experiments and simulations both. In this work, we tackle this open question by monitoring and rationalizing the ice-nucleating ability of the same compound, cholesterol (CHL), from crystals to self-assembled monolayers with varying degrees of order. We have found that CHL crystals outperform any self-assembled CHL monolayer. Additionally, our results demonstrate that the more ordered the monolayers are, the better they can facilitate the formation of ice, albeit always less than the crystal. We argue that an analysis of the pre-critical nuclei, as obtained by means of unbiased molecular dynamics simulations can be used in conjunction with experimental measurements such as SFG, to infer the actual ice-nucleating ability of a given material.

While this work focusses entirely on CHL, we expect our findings to be directly applicable to similar systems: for instance, particles containing long-chain fatty acids are of great relevance to the formation of ice driven by sea-spray aerosols[215], and there are many examples of ice-nucleating impurities in the form of self-assembled monolayers of alcohols[216–218]. In addition, the formation of ice in biological matter, which is key in the context of cryopreservation, does involve the formation of ice on/through the lipid bilayers which form the building blocks of cells[219–222].

Importantly, the fact that order seems to outweigh molecular structure when it comes to heterogeneous ice nucleation has a strong impact on the design and discovery of the next-generation of ice-nucleating agents, many of which are bound to be biological in nature[140,154,223–225]. In fact, some of them harness already supramolecular structures with variable degrees of ordering (ice nucleating proteins being an obvious example[226–229]) to facilitate ice formation. At the moment, there is a strong emphasis on the molecular structure of these compounds as opposed to their topology: our results suggest that we might want to shift our attention towards the design of supramolecular assemblies as opposed to trying to discover the most effective functional groups that are supposed to trigger ice formation – often a trial-and-error process.

References

(1) Kennedy, D. What Don't We Know? *Science.* **2005**, *309* (5731), 75–75. https://doi.org/10.1126/science.309.5731.75.

(2) So Much More to Know. *Science.* **2005**, *309* (5731), 78b-102b. https://doi.org/10.1126/science.309.5731.78b.

(3) Gasser, T. M.; Thoeny, A. V; Fortes, A. D.; Loerting, T. Structural Characterization of Ice XIX as the Second Polymorph Related to Ice VI. *Nat. Commun.* **2021**, *12* (1), 1128. https://doi.org/10.1038/s41467-021-21161-z.

(4) Benedict, W. S.; Gailar, N.; Plyler, E. K. Rotation-Vibration Spectra of Deuterated Water Vapor. *J. Chem. Phys.* **1956**, *24* (6), 1139–1165. https://doi.org/10.1063/1.1742731.

(5) Agmon, N. The Grotthuss Mechanism. *Chem. Phys. Lett.* **1995**, *244* (5–6), 456–462. https://doi.org/10.1016/0009-2614(95)00905-J.

(6) Phase diagram of water https://en.wikipedia.org/wiki/Phase_diagram#/media/File:Phase_diagram_of_water.svg.

(7) Fletcher, N. H. Structure and Energy of Ordinary Ice. In *The Chemical Physics of Ice*; Cambridge University Press, 1970; pp 23–48. https://doi.org/10.1017/CBO9780511735639.004.

(8) Leiter, A.; Gaukel, V. Food Freezing: Crystal Structure and Size. In *Reference Module in Food Science*; Elsevier, 2016. https://doi.org/10.1016/B978-0-08-100596-5.03109-7.

(9) Sánchez, M. A.; Kling, T.; Ishiyama, T.; van Zadel, M.-J.; Bisson, P. J.; Mezger, M.; Jochum, M. N.; Cyran, J. D.; Smit, W. J.; Bakker, H. J.; Shultz, M. J.; Morita, A.; Donadio, D.; Nagata, Y.; Bonn, M.; Backus, E. H. G. Experimental and Theoretical Evidence for Bilayer-by-Bilayer Surface Melting of Crystalline Ice. *Proc. Natl. Acad. Sci.* **2017**, *114* (2), 227–232. https://doi.org/10.1073/pnas.1612893114.

(10) Singer, S. J.; Knight, C. Hydrogen-Bond Topology and Proton Ordering in Ice and Water Clusters; John Wiley & Sons, Ltd, 2011; pp 1–74. https://doi.org/10.1002/9781118135242.ch1.

(11) Pan, D.; Liu, L.-M.; Tribello, G. A.; Slater, B.; Michaelides, A.; Wang, E. Surface Energy and Surface Proton Order of the Ice Ih Basal and Prism Surfaces. *J. Phys. Condens. Matter* **2010**, *22* (7), 074209. https://doi.org/10.1088/0953-8984/22/7/074209.

(12) Jackson, S. M.; Nield, V. M.; Whitworth, R. W.; Oguro, M.; Wilson, C. C. Single-Crystal Neutron Diffraction Studies of the Structure of Ice XI. *J. Phys. Chem. B* **1997**, *101* (32), 6142–6145. https://doi.org/10.1021/jp9632551.

(13) Singer, S. J.; Kuo, J.-L.; Hirsch, T. K.; Knight, C.; Ojamäe, L.; Klein, M. L. Hydrogen-Bond Topology and the Ice VII/VIII and Ice Ih/XI Proton-Ordering Phase Transitions. *Phys. Rev. Lett.* **2005**, *94* (13), 135701. https://doi.org/10.1103/PhysRevLett.94.135701.

(14) Parkkinen, P.; Riikonen, S.; Halonen, L. Ice XI: Not That Ferroelectric. *J. Phys. Chem. C* **2014**, *118* (45), 26264–26275. https://doi.org/10.1021/jp510009m.

(15) Segelstein, D. J. The Complex Refractive Index of Water. **1981**.

(16) Absorption spectrum of water https://omlc.org/spectra/water/abs/index.html.

(17) Petrenko, V. F.; Whitworth, R. W. Elastic, Thermal, and Lattice Dynamical Properties. In *Physics of Ice*; Oxford University Press, 2002; pp 36–59. https://doi.org/10.1093/acprof:oso/9780198518945.003.0003.

(18) Roos, D. v. d. S. Rapid Production of Single Crystals of Ice. *J. Glaciol.* **1975**, *14* (71), 325–328. https://doi.org/10.3189/S0022143000021808.

(19) Higuchi, K. A New Method for Recording the Grain-Structure of Ice. *J. Glaciol.* **1957**, *3* (22), 131–132.

https://doi.org/10.3189/S002214300002445X.
(20) Franken, P. A.; Hill, A. E.; Peters, C. W.; Weinreich, G. Generation of Optical Harmonics. *Phys. Rev. Lett.* **1961**, *7* (4), 118–119. https://doi.org/10.1103/PhysRevLett.7.118.
(21) Maiman, T. H. Optical and Microwave-Optical Experiments in Ruby. *Phys. Rev. Lett.* **1960**, *4* (11), 564–566. https://doi.org/10.1103/PhysRevLett.4.564.
(22) Boyd, R. W. Nonlinear Optics. **2020**.
(23) Halina, A. *Introduction to Laser Spectroscopy*; Elsevier, 2005. https://doi.org/10.1016/B978-0-444-51662-6.X5000-X.
(24) Lambert, A. G.; Davies, P. B.; Neivandt, D. J. Implementing the Theory of Sum Frequency Generation Vibrational Spectroscopy: A Tutorial Review. *Appl. Spectrosc. Rev.* **2005**, *40* (2), 103–145. https://doi.org/10.1081/ASR-200038326.
(25) Zhuang, X.; Miranda, P. B.; Kim, D.; Shen, Y. R. Mapping Molecular Orientation and Conformation at Interfaces by Surface Nonlinear Optics. *Phys. Rev. B* **1999**, *59* (19), 12632–12640. https://doi.org/10.1103/PhysRevB.59.12632.
(26) Hamm, P.; Zanni, M. *Concepts and Methods of 2D Infrared Spectroscopy*; Cambridge University Press: Cambridge, 2011; Vol. 9781107000. https://doi.org/10.1017/CBO9780511675935.
(27) Hamm, P. Principles of Nonlinear Optical Spectroscopy: A Practical Approach or: Mukamel for Dummies. **2005**.
(28) Elsaesser, T. Introduction: Ultrafast Processes in Chemistry. *Chem. Rev.* **2017**, *117* (16), 10621–10622. https://doi.org/10.1021/acs.chemrev.7b00226.
(29) Dods, R.; Båth, P.; Morozov, D.; Gagnér, V. A.; Arnlund, D.; Luk, H. L.; Kübel, J.; Maj, M.; Vallejos, A.; Wickstrand, C.; Bosman, R.; Beyerlein, K. R.; Nelson, G.; Liang, M.; Milathianaki, D.; Robinson, J.; Harimoorthy, R.; Berntsen, P.; Malmerberg, E.; Johansson, L.; Andersson, R.; Carbajo, S.; Claesson, E.; Conrad, C. E.; Dahl, P.; Hammarin, G.; Hunter, M. S.; Li, C.; Lisova, S.; Royant, A.; Safari, C.; Sharma, A.; Williams, G. J.; Yefanov, O.; Westenhoff, S.; Davidsson, J.; DePonte, D. P.; Boutet, S.; Barty, A.; Katona, G.; Groenhof, G.; Brändén, G.; Neutze, R. Ultrafast Structural Changes within a Photosynthetic Reaction Centre. *Nature* **2021**, *589* (7841), 310–314. https://doi.org/10.1038/s41586-020-3000-7.
(30) Xiong, W.; Laaser, J. E.; Mehlenbacher, R. D.; Zanni, M. T. Adding a Dimension to the Infrared Spectra of Interfaces Using Heterodyne Detected 2D Sum-Frequency Generation (HD 2D SFG) Spectroscopy. *Proc. Natl. Acad. Sci.* **2011**, *108* (52), 20902–20907. https://doi.org/10.1073/pnas.1115055108.
(31) Huang, J.; Kumar, P. Observation of Quantum Frequency Conversion. *Phys. Rev. Lett.* **1992**, *68* (14), 2153–2156. https://doi.org/10.1103/PhysRevLett.68.2153.
(32) Backus, E. H. G.; Cyran, J. D.; Grechko, M.; Nagata, Y.; Bonn, M. Time-Resolved Sum Frequency Generation Spectroscopy: A Quantitative Comparison Between Intensity and Phase-Resolved Spectroscopy. *J. Phys. Chem. A* **2018**, *122* (9), 2401–2410. https://doi.org/10.1021/acs.jpca.7b12303.
(33) Lock, A. J.; Woutersen, S.; Bakker, H. J. Ultrafast Energy Equilibration in Hydrogen-Bonded Liquids. *J. Phys. Chem. A* **2001**, *105* (8), 1238–1243. https://doi.org/10.1021/jp003158e.
(34) Hirlimann, C. Laser Basics; 2005; pp 1–23. https://doi.org/10.1007/0-387-26674-7_1.
(35) Abramczyk, H. Generation of Ultrashort Laser Pulses. In *Introduction to Laser Spectroscopy*; Elsevier, 2005; pp 31–58. https://doi.org/10.1016/B978-044451662-6/50004-6.
(36) Abramczyk, H. Pulse Amplification. In *Introduction to Laser Spectroscopy*; Elsevier, 2005; pp 147–160. https://doi.org/10.1016/B978-044451662-6/50007-1.
(37) Keller, U. 2.1 Ultrafast Solid-State Lasers. In *Laser Systems, Part 1*; Herziger, G., Weber, H., Poprawe, R., Eds.; Springer Berlin Heidelberg: Berlin, Heidelberg; pp 33–167. https://doi.org/10.1007/978-3-540-44821-1_2.
(38) Bretschneider, S. Gutenberg Open Science: Photophysics of Lead-Halide Perovskite https://openscience.ub.uni-mainz.de/handle/20.500.12030/1173 (accessed Aug 4, 2021). https://doi.org/http://doi.org/10.25358/openscience-1171.
(39) Cerullo, G.; De Silvestri, S. Ultrafast Optical Parametric Amplifiers. *Rev. Sci. Instrum.* **2003**, *74* (1 I), 1–18. https://doi.org/10.1063/1.1523642.
(40) De Silvestri, S.; Cerullo, G.; Lanzani, G. *Coherent Vibrational Dynamics*; Lanzani, G., Cerullo, G., De Silvestri, S., Eds.; CRC Press, 2007. https://doi.org/10.1201/9781420017519.
(41) Herrmann, H. Kinetics of Aqueous Phase Reactions Relevant for Atmospheric Chemistry. *Chem. Rev.* **2003**, *103* (12), 4691–4716. https://doi.org/10.1021/cr020658q.
(42) Aloisio, S.; Francisco, J. S. Radical-Water Complexes in Earth's Atmosphere. *Acc. Chem. Res.* **2000**, *33* (12), 825–830. https://doi.org/10.1021/ar000097u.
(43) Scatena, L. F. Water at Hydrophobic Surfaces: Weak Hydrogen Bonding and Strong Orientation Effects. *Science.* **2001**, *292* (5518), 908–912. https://doi.org/10.1126/science.1059514.
(44) Park, S.; Shao, Y.; Liu, J.; Wang, Y. Oxygen Electrocatalysts for Water Electrolyzers and Reversible Fuel Cells: Status and Perspective. *Energy Environ. Sci.* **2012**, *5* (11), 9331. https://doi.org/10.1039/c2ee22554a.
(45) Toney, M. F.; Howard, J. N.; Richer, J.; Borges, G. L.; Gordon, J. G.; Melroy, O. R.; Wiesler, D. G.; Yee, D.; Sorensen,

L. B. Voltage-Dependent Ordering of Water Molecules at an Electrode–Electrolyte Interface. *Nature* **1994**, *368* (6470), 444–446. https://doi.org/10.1038/368444a0.

(46) Hydro | Earth https://earth.gsfc.nasa.gov/index.php/hydro (accessed May 31, 2021).

(47) Tolbert, M. A.; Rossi, M. J.; Golden, D. M. Antarctic Ozone Depletion Chemistry: Reactions of N2O5 with H2O and HCl on Ice Surfaces. *Science.* **1988**, *240* (4855), 1018–1021. https://doi.org/10.1126/science.240.4855.1018.

(48) Bartels-Rausch, T.; Jacobi, H.-W.; Kahan, T. F.; Thomas, J. L.; Thomson, E. S.; Abbatt, J. P. D.; Ammann, M.; Blackford, J. R.; Bluhm, H.; Boxe, C.; Domine, F.; Frey, M. M.; Gladich, I.; Guzmán, M. I.; Heger, D.; Huthwelker, T.; Klán, P.; Kuhs, W. F.; Kuo, M. H.; Maus, S.; Moussa, S. G.; McNeill, V. F.; Newberg, J. T.; Pettersson, J. B. C.; Roeselová, M.; Sodeau, J. R. A Review of Air–Ice Chemical and Physical Interactions (AICI): Liquids, Quasi-Liquids, and Solids in Snow. *Atmos. Chem. Phys.* **2014**, *14* (3), 1587–1633. https://doi.org/10.5194/acp-14-1587-2014.

(49) Stibal, M.; Šabacká, M.; Žárský, J. Biological Processes on Glacier and Ice Sheet Surfaces. *Nat. Geosci.* **2012**, *5* (11), 771–774. https://doi.org/10.1038/ngeo1611.

(50) Kahan, T. F.; Wren, S. N.; Donaldson, D. J. A Pinch of Salt Is All It Takes: Chemistry at the Frozen Water Surface. *Acc. Chem. Res.* **2014**, *47* (5), 1587–1594. https://doi.org/10.1021/ar5000715.

(51) Shen, Y. R. Surface Properties Probed by Second-Harmonic and Sum-Frequency Generation. *Nature* **1989**, *337* (6207), 519–525. https://doi.org/10.1038/337519a0.

(52) Ford, T. A.; Falk, M. Hydrogen Bonding in Water and Ice. *Can. J. Chem.* **1968**, *46* (22), 3579–3586. https://doi.org/10.1139/v68-591.

(53) Rey, R.; Møller, K. B.; Hynes, J. T. Hydrogen Bond Dynamics in Water and Ultrafast Infrared Spectroscopy. *J. Phys. Chem. A* **2002**, *106* (50), 11993–11996. https://doi.org/10.1021/jp026419o.

(54) Schaefer, J.; Backus, E. H. G.; Nagata, Y.; Bonn, M. Both Inter- and Intramolecular Coupling of O-H Groups Determine the Vibrational Response of the Water/Air Interface. *J. Phys. Chem. Lett.* **2016**, *7* (22), 4591–4595. https://doi.org/10.1021/acs.jpclett.6b02513.

(55) Ni, Y.; Skinner, J. L. IR and SFG Vibrational Spectroscopy of the Water Bend in the Bulk Liquid and at the Liquid-Vapor Interface, Respectively. *J. Chem. Phys.* **2015**, *143* (1), 014502. https://doi.org/10.1063/1.4923462.

(56) Seki, T.; Sun, S.; Zhong, K.; Yu, C. C.; MacHel, K.; Dreier, L. B.; Backus, E. H. G.; Bonn, M.; Nagata, Y. Unveiling Heterogeneity of Interfacial Water through the Water Bending Mode. *J. Phys. Chem. Lett.* **2019**, *10* (21), 6936–6941. https://doi.org/10.1021/acs.jpclett.9b02748.

(57) Yu, C.-C.; Chiang, K.-Y.; Okuno, M.; Seki, T.; Ohto, T.; Yu, X.; Korepanov, V.; Hamaguchi, H.; Bonn, M.; Hunger, J.; Nagata, Y. Vibrational Couplings and Energy Transfer Pathways of Water's Bending Mode. *Nat. Commun.* **2020**, *11* (1), 5977. https://doi.org/http://dx.doi.org/10.1038/s41467-020-19759-w.

(58) Vinaykin, M.; Benderskii, A. Vibrational Sum-Frequency Spectrum of the Water Bend at the Air / Water Interface Supplementary Information. *J. Phys. Chem. Lett.* **2012**, *3*, 3348–3352.

(59) Hernandez, J.; Uras, N.; Devlin, J. P. Molecular Bending Mode Frequencies of the Surface and Interior of Crystalline Ice. *J. Chem. Phys.* **1998**, *108* (11), 4525–4529. https://doi.org/10.1063/1.475880.

(60) Imoto, S.; Xantheas, S. S.; Saito, S. Molecular Origin of the Difference in the HOH Bend of the IR Spectra between Liquid Water and Ice. *J. Chem. Phys.* **2013**, *138* (5), 054506. https://doi.org/10.1063/1.4789951.

(61) Rey, R.; Ingrosso, F.; Elsaesser, T.; Hynes, J. T. Pathways for H 2 O Bend Vibrational Relaxation in Liquid Water. *J. Phys. Chem. A* **2009**, *113* (31), 8949–8962. https://doi.org/10.1021/jp9036342.

(62) van der Post, S. T.; Hsieh, C.-S.; Okuno, M.; Nagata, Y.; Bakker, H. J.; Bonn, M.; Hunger, J. Strong Frequency Dependence of Vibrational Relaxation in Bulk and Surface Water Reveals Sub-Picosecond Structural Heterogeneity. *Nat. Commun.* **2015**, *6* (1), 8384. https://doi.org/10.1038/ncomms9384.

(63) Smit, W. J.; Tang, F.; Nagata, Y.; Sánchez, M. A.; Hasegawa, T.; Backus, E. H. G.; Bonn, M.; Bakker, H. J. Observation and Identification of a New OH Stretch Vibrational Band at the Surface of Ice. *J. Phys. Chem. Lett.* **2017**, *8* (15), 3656–3660. https://doi.org/10.1021/acs.jpclett.7b01295.

(64) Ishiyama, T.; Takahashi, H.; Morita, A. Origin of Vibrational Spectroscopic Response at Ice Surface. *J. Phys. Chem. Lett.* **2012**, *3* (20), 3001–3006. https://doi.org/10.1021/jz3012723.

(65) Wei, X.; Miranda, P. B.; Zhang, C.; Shen, Y. R. Sum-Frequency Spectroscopic Studies of Ice Interfaces. *Phys. Rev. B* **2002**, *66* (8), 085401. https://doi.org/10.1103/PhysRevB.66.085401.

(66) Falk, M. The Frequency of the HOH Bending Fundamental in Solids and Liquids. *Spectrochim. Acta Part A Mol. Spectrosc.* **1984**, *40* (1), 43–48. https://doi.org/10.1016/0584-8539(84)80027-6.

(67) Seki, T.; Yu, C. C.; Yu, X.; Ohto, T.; Sun, S.; Meister, K.; Backus, E. H. G.; Bonn, M.; Nagata, Y. Decoding the Molecular Water Structure at Complex Interfaces through Surface-Specific Spectroscopy of the Water Bending Mode. *Phys. Chem. Chem. Phys.* **2020**, *22* (19), 10934–10940. https://doi.org/10.1039/d0cp01269f.

(68) Ahmed, M.; Nihonyanagi, S.; Kundu, A.; Yamaguchi, S.; Tahara, T. Resolving the Controversy over Dipole versus Quadrupole Mechanism of Bend Vibration of Water in Vibrational Sum Frequency Generation Spectra. *J. Phys. Chem. Lett.* **2020**, *11* (21), 9123–9130. https://doi.org/10.1021/acs.jpclett.0c02644.

(69) Moberg, D. R.; Straight, S. C.; Paesani, F. Temperature Dependence of the Air/Water Interface Revealed by

Polarization Sensitive Sum-Frequency Generation Spectroscopy. *J. Phys. Chem. B* **2018**, *122* (15), 4356–4365. https://doi.org/10.1021/acs.jpcb.8b01726.

(70) Dutta, C.; Benderskii, A. V. On the Assignment of the Vibrational Spectrum of the Water Bend at the Air/Water Interface. *J. Phys. Chem. Lett.* **2017**, *8* (4), 801–804. https://doi.org/10.1021/acs.jpclett.6b02678.

(71) Wei, X.; Miranda, P. B.; Shen, Y. R. Surface Vibrational Spectroscopic Study of Surface Melting of Ice. *Phys. Rev. Lett.* **2001**, *86* (8), 1554–1557. https://doi.org/10.1103/PhysRevLett.86.1554.

(72) Huse, N.; Ashihara, S.; Nibbering, E. T. J.; Elsaesser, T. Ultrafast Vibrational Relaxation of O-H Bending and Librational Excitations in Liquid H 2 O. https://doi.org/10.1016/j.cplett.2005.02.007.

(73) Carpenter, W. B.; Fournier, J. A.; Biswas, R.; Voth, G. A.; Tokmakoff, A. Delocalization and Stretch-Bend Mixing of the HOH Bend in Liquid Water. *J. Chem. Phys.* **2017**, *147* (8), 84503. https://doi.org/10.1063/1.4987153.

(74) Riemenschneider, J.; Wulf, A.; Ludwig, R. The Effects of Temperature and H/D Isotopic Dilution on the Transmission and Attenuated Total Reflection FTIR Spectra of Water. *Zeitschrift für Phys. Chemie* **2009**, *223* (9), 1011–1022. https://doi.org/10.1524/zpch.2009.6067.

(75) Backus, E. H. G.; Garcia-Araez, N.; Bonn, M.; Bakker, H. J. On the Role of Fresnel Factors in Sum-Frequency Generation Spectroscopy of Metal-Water and Metal-Oxide-Water Interfaces. *J. Phys. Chem. C* **2012**, *116* (44), 23351–23361. https://doi.org/10.1021/jp306273d.

(76) Warren, S. G. Optical Constants of Ice from the Ultraviolet to the Microwave. *Appl. Opt.* **1984**, *23* (8), 1206. https://doi.org/10.1364/AO.23.001206.

(77) Zasetsky, A. Y.; Khalizov, A. F.; Earle, M. E.; Sloan, J. J. Frequency Dependent Complex Refractive Indices of Supercooled Liquid Water and Ice Determined from Aerosol Extinction Spectra. *J. Phys. Chem. A* **2005**, *109* (12), 2760–2764. https://doi.org/10.1021/jp044823c.

(78) Bernal, J. D.; Fowler, R. H. A Theory of Water and Ionic Solution, with Particular Reference to Hydrogen and Hydroxyl Ions. *J. Chem. Phys.* **1933**, *1* (8), 515–548. https://doi.org/10.1063/1.1749327.

(79) Pauling, L. The Structure and Entropy of Ice and of Other Crystals with Some Randomness of Atomic Arrangement. *J. Am. Chem. Soc.* **1935**, *57* (12), 2680–2684. https://doi.org/10.1021/ja01315a102.

(80) Giauque, W. F.; Stout, J. W. The Entropy of Water and the Third Law of Thermodynamics. The Heat Capacity of Ice from 15 to 273°K. *J. Am. Chem. Soc.* **1936**, *58* (7), 1144–1150. https://doi.org/10.1021/ja01298a023.

(81) Nagle, J. F. Lattice Statistics of Hydrogen Bonded Crystals. I. The Residual Entropy of Ice. *J. Math. Phys.* **1966**, *7* (8), 1484–1491. https://doi.org/10.1063/1.1705058.

(82) Hayashi, T.; Muguruma, C.; Okamoto, Y. Calculation of the Residual Entropy of Ice Ih by Monte Carlo Simulation with the Combination of the Replica-Exchange Wang–Landau Algorithm and Multicanonical Replica-Exchange Method. *J. Chem. Phys.* **2021**, *154* (4), 044503. https://doi.org/10.1063/5.0038157.

(83) Hirsch, T. K.; Ojamäe, L. Quantum-Chemical and Force-Field Investigations of Ice Ih: Computation of Proton-Ordered Structures and Prediction of Their Lattice Energies. *J. Phys. Chem. B* **2004**, *108* (40), 15856–15864. https://doi.org/10.1021/jp048434u.

(84) Kato, F.; Sugimoto, T.; Matsumoto, Y. Direct Experimental Evidence for Markedly Enhanced Surface Proton Activity Inherent to Water Ice. *J. Phys. Chem. Lett.* **2020**, *11* (7), 2524–2529. https://doi.org/10.1021/acs.jpclett.0c00384.

(85) Pan, D.; Liu, L.-M.; Tribello, G. A.; Slater, B.; Michaelides, A.; Wang, E. Surface Energy and Surface Proton Order of Ice Ih. *Phys. Rev. Lett.* **2008**, *101* (15), 155703. https://doi.org/10.1103/PhysRevLett.101.155703.

(86) Buch, V.; Groenzin, H.; Li, I.; Shultz, M. J.; Tosatti, E. Proton Order in the Ice Crystal Surface. *Proc. Natl. Acad. Sci.* **2008**, *105* (16), 5969–5974. https://doi.org/10.1073/pnas.0710129105.

(87) Good, R. J. Surface Entropy and Surface Orientation of Polar Liquids. *J. Phys. Chem.* **1957**, *61* (6), 810–813. https://doi.org/10.1021/j150552a029.

(88) Fletcher, N. H. Reconstruction of Ice Crystal Surfaces at Low Temperatures. *Philos. Mag. B* **1992**, *66* (1), 109–115. https://doi.org/10.1080/13642819208221298.

(89) Park, S. C.; Moon, E. S.; Kang, H. Some Fundamental Properties and Reactions of Ice Surfaces at Low Temperatures. *Phys. Chem. Chem. Phys.* **2010**, *12* (38), 12000–12011. https://doi.org/10.1039/c003592k.

(90) Slater, B.; Michaelides, A. Surface Premelting of Water Ice. *Nat. Rev. Chem.* **2019**, *3* (3), 172–188. https://doi.org/10.1038/s41570-019-0080-8.

(91) Dosch, H.; Lied, A.; Bilgram, J. H. Glancing-Angle X-Ray Scattering Studies of the Premelting of Ice Surfaces. *Surf. Sci.* **1995**, *327* (1–2), 145–164. https://doi.org/10.1016/0039-6028(94)00801-9.

(92) Llombart, P.; Noya, E. G.; MacDowell, L. G. Surface Phase Transitions and Crystal Habits of Ice in the Atmosphere. *Sci. Adv.* **2020**, *6* (21), eaay9322. https://doi.org/10.1126/sciadv.aay9322.

(93) Stiopkin, I. V.; Jayathilake, H. D.; Weeraman, C.; Benderskii, A. V. Temporal Effects on Spectroscopic Line Shapes, Resolution, and Sensitivity of the Broad-Band Sum Frequency Generation. *J. Chem. Phys.* **2010**, *132* (23). https://doi.org/10.1063/1.3432776.

(94) Groenzin, H.; Li, I.; Buch, V.; Shultz, M. J. The Single-Crystal, Basal Face of Ice Ih Investigated with Sum Frequency

Generation. *J. Chem. Phys.* **2007**, *127* (21), 214502. https://doi.org/10.1063/1.2801642.
(95) Shi, L.; Gruenbaum, S. M.; Skinner, J. L. Interpretation of IR and Raman Line Shapes for H 2 O and D 2 O Ice Ih. *J. Phys. Chem. B* **2012**, *116* (47), 13821–13830. https://doi.org/10.1021/jp3059239.
(96) Seifert, G.; Weidlich, K.; Graener, H. Picosecond Ir Hole-Burning Spectroscopy on HDO Ice Ih. *Phys. Rev. B* **1997**, *56* (22), R14231–R14234. https://doi.org/10.1103/PhysRevB.56.R14231.
(97) Sugimoto, T.; Aiga, N.; Otsuki, Y.; Watanabe, K.; Matsumoto, Y. Emergent High-Tc Ferroelectric Ordering of Strongly Correlated and Frustrated Protons in a Heteroepitaxial Ice Film. *Nat. Phys.* **2016**, *12* (11), 1063–1068. https://doi.org/10.1038/nphys3820.
(98) Rice, S. A.; Bergren, M. S.; Belch, A. C.; Nielsen, G. A Theoretical Analysis of the Hydroxyl Stretching Spectra of Ice Ih, Liquid Water, and Amorphous Solid Water. *J. Phys. Chem.* **1983**, *87* (21), 4295–4308. https://doi.org/10.1021/j100244a061.
(99) Nojima, Y.; Suzuki, Y.; Takahashi, M.; Yamaguchi, S. Proton Order toward the Surface of Ice Ih Revealed by Heterodyne-Detected Sum Frequency Generation Spectroscopy. *J. Phys. Chem. Lett.* **2017**, *8* (20), 5031–5034. https://doi.org/10.1021/acs.jpclett.7b02198.
(100) Water tetrahedral structure https://plus.maths.org/content/os/latestnews/may-aug10/ice/index.
(101) Donaldson, D. J.; Tuck, A. F.; Vaida, V. Atmospheric Photochemistry via Vibrational Overtone Absorption. *Chem. Rev.* **2003**, *103* (12), 4717–4730. https://doi.org/10.1021/cr0206519.
(102) Donaldson, D. J.; Frost, G. J.; Rosenlof, K. H.; Tuck, A. F.; Vaida, V. Atmospheric Radical Production by Excitation of Vibrational Overtones via Absorption of Visible Light. *Geophys. Res. Lett.* **1997**, *24* (21), 2651–2654. https://doi.org/10.1029/97GL02663.
(103) Staikova, M.; Donaldson, D. J.; Francisco, J. S. Overtone-Induced Reactions on the HO 2 NO 2 Potential Surface. *J. Phys. Chem. A* **2002**, *106* (12), 3023–3028. https://doi.org/10.1021/jp0143746.
(104) Vaida, V. Photolysis of Sulfuric Acid Vapor by Visible Solar Radiation. *Science.* **2003**, *299* (5612), 1566–1568. https://doi.org/10.1126/science.1079297.
(105) Shin, H. K. Inter- and Intramolecular Vibrational Energy Flow in a Formamide–Water Complex. *J. Phys. Chem. A* **2020**, *124* (16), 3031–3037. https://doi.org/10.1021/acs.jpca.0c00584.
(106) Staikova, M.; Donaldson, D. J. Water Complexes as Catalysts in Atmospheric Reactions. *Phys. Chem. Earth, Part C Solar, Terr. Planet. Sci.* **2001**, *26* (7), 473–478. https://doi.org/10.1016/S1464-1917(01)00034-4.
(107) Staikova, M.; Oh, M.; Donaldson, D. J. Overtone-Induced Decarboxylation: A Potential Sink for Atmospheric Diacids. *J. Phys. Chem. A* **2005**, *109* (4), 597–602. https://doi.org/10.1021/jp046141v.
(108) Devlin, J. P.; Uras, N.; Sadlej, J.; Buch, V. Discrete Stages in the Solvation and Ionization of Hydrogen Chloride Adsorbed on Ice Particles. *Nature* **2002**, *417* (6886), 269–271. https://doi.org/10.1038/417269a.
(109) Cyran, J. D.; Backus, E. H. G.; Nagata, Y.; Bonn, M. Structure from Dynamics: Vibrational Dynamics of Interfacial Water as a Probe of Aqueous Heterogeneity. *J. Phys. Chem. B* **2018**, *122* (14), 3667–3679. https://doi.org/10.1021/acs.jpcb.7b10574.
(110) Nihonyanagi, S.; Yamaguchi, S.; Tahara, T. Ultrafast Dynamics at Water Interfaces Studied by Vibrational Sum Frequency Generation Spectroscopy. *Chem. Rev.* **2017**, *117* (16), 10665–10693. https://doi.org/10.1021/acs.chemrev.6b00728.
(111) Timmer, R. L. A.; Bakker, H. J. Vibrational Förster Transfer in Ice Ih. *J. Phys. Chem. A* **2010**, *114* (12), 4148–4155. https://doi.org/10.1021/jp911726s.
(112) Perakis, F.; Hamm, P. Two-Dimensional Infrared Spectroscopy of Neat Ice Ih. *Phys. Chem. Chem. Phys.* **2012**, *14* (18), 6250–6256. https://doi.org/10.1039/c2cp23710e.
(113) Dokter, A. M.; Bakker, H. J. Transient Absorption of Vibrationally Excited Ice Ih. *J. Chem. Phys.* **2008**, *128* (2), 024502. https://doi.org/10.1063/1.2820765.
(114) Woutersen, S.; Emmerichs, U.; Nienhuys, H. K.; Bakker, H. J. Anomalous Temperature Dependence of Vibrational Lifetimes in Water and Ice. *Phys. Rev. Lett.* **1998**, *81* (5), 1106–1109. https://doi.org/10.1103/PhysRevLett.81.1106.
(115) Cowan, M. L.; Bruner, B. D.; Huse, N.; Dwyer, J. R.; Chugh, B.; Nibbering, E. T. J.; Elsaesser, T.; Miller, R. J. D. Ultrafast Memory Loss and Energy Redistribution in the Hydrogen Bond Network of Liquid H2O. *Nature* **2005**, *434* (7030), 199–202. https://doi.org/10.1038/nature03383.
(116) Roberts, S. T.; Ramasesha, K.; Tokmakoff, A. Structural Rearrangements in Water Viewed through Two-Dimensional Infrared Spectroscopy. *Acc. Chem. Res.* **2009**, *42* (9), 1239–1249. https://doi.org/10.1021/ar900088g.
(117) Woutersen, S.; Bakker, H. J. Resonant Intermolecular Transfer of Vibrational Energy in Liquid Water. *Nature* **1999**, *402* (6761), 507–509. https://doi.org/10.1038/990058.
(118) Nibbering, E. T. J.; Elsaesser, T. Ultrafast Vibrational Dynamics of Hydrogen Bonds in the Condensed Phase. *Chem. Rev.* **2004**, *104* (4), 1887–1914. https://doi.org/10.1021/cr020694p.
(119) Pakoulev, A.; Wang, Z.; Dlott, D. D. Vibrational Relaxation and Spectral Evolution Following Ultrafast OH Stretch

Excitation of Water. *Chem. Phys. Lett.* **2003**, *371* (5–6), 594–600. https://doi.org/10.1016/S0009-2614(03)00314-2.

(120) Stenger, J.; Madsen, D.; Dreyer, J.; Nibbering, E. T. J.; Hamm, P.; Elsaesser, T. Coherent Response of Hydrogen Bonds in Liquids Probed by Ultrafast Vibrational Spectroscopy. *J. Phys. Chem. A* **2001**, *105* (13), 2929–2932. https://doi.org/10.1021/jp003153h.

(121) Hsieh, C.-S.; Okuno, M.; Hunger, J.; Backus, E. H. G.; Nagata, Y.; Bonn, M. Aqueous Heterogeneity at the Air/Water Interface Revealed by 2D-HD-SFG Spectroscopy. *Angew. Chemie Int. Ed.* **2014**, *53* (31), 8146–8149. https://doi.org/10.1002/anie.201402566.

(122) Zhang, Z.; Piatkowski, L.; Bakker, H. J.; Bonn, M. Ultrafast Vibrational Energy Transfer at the Water/Air Interface Revealed by Two-Dimensional Surface Vibrational Spectroscopy. *Nat. Chem.* **2011**, *3* (11), 888–893. https://doi.org/10.1038/nchem.1158.

(123) McGuire; Shen. Ultrafast Vibrational Dynamics at Water Interfaces. *Science.* **2006**, *313* (5795), 1945–1948.

(124) Smits, M.; Ghosh, A.; Sterrer, M.; Müller, M.; Bonn, M. Ultrafast Vibrational Energy Transfer between Surface and Bulk Water at the Air-Water Interface. *Phys. Rev. Lett.* **2007**, *98* (9), 098302. https://doi.org/10.1103/PhysRevLett.98.098302.

(125) Smit, W. J.; Tang, F.; Sánchez, M. A.; Backus, E. H. G.; Xu, L.; Hasegawa, T.; Bonn, M.; Bakker, H. J.; Nagata, Y. Excess Hydrogen Bond at the Ice-Vapor Interface around 200 K. *Phys. Rev. Lett.* **2017**, *119* (13), 133003. https://doi.org/10.1103/PhysRevLett.119.133003.

(126) Du, Q.; Freysz, E.; Shen, Y. R. Surface Vibrational Spectroscopic Studies of Hydrogen Bonding and Hydrophobicity. *Science.* **1994**, *264* (5160), 826–828.

(127) Cyran, J. D.; Backus, E. H. G.; van Zadel, M.-J.; Bonn, M. Comparative Adsorption of Acetone on Water and Ice Surfaces. *Angew. Chemie Int. Ed.* **2019**, *58* (11), 3620–3624. https://doi.org/10.1002/anie.201813517.

(128) Novak, A. Hydrogen Bonding in Solids Correlation of Spectroscopic and Crystallographic Data. In *Large Molecules*; Springer Berlin Heidelberg: Berlin, Heidelberg; pp 177–216. https://doi.org/10.1007/BFb0116438.

(129) Deiseroth, M.; Bonn, M.; Backus, E. H. G. Electrolytes Change the Interfacial Water Structure but Not the Vibrational Dynamics. *J. Phys. Chem. B* **2019**, *123* (40), 8610–8616. https://doi.org/10.1021/acs.jpcb.9b08131.

(130) Deàk, J. C.; Rhea, S. T.; Iwaki, L. K.; Dlott, D. D. Vibrational Energy Relaxation and Spectral Diffusion in Water and Deuterated Water. *J. Phys. Chem. A* **2000**, *104* (21), 4866–4875. https://doi.org/10.1021/jp994492h.

(131) Finzi, J. Vibrational Relaxation of Water Vapor. *J. Chem. Phys.* **1977**, *67* (9), 4053. https://doi.org/10.1063/1.435379.

(132) Hsieh, C.-S.; Campen, R. K.; Okuno, M.; Backus, E. H. G.; Nagata, Y.; Bonn, M. Mechanism of Vibrational Energy Dissipation of Free OH Groups at the Air-Water Interface. *Proc. Natl. Acad. Sci.* **2013**, *110* (47), 18780–18785. https://doi.org/10.1073/pnas.1314770110.

(133) Clapp, M. L.; Worsnop, D. R.; Miller, R. E. Frequency-Dependent Optical Constants of Water Ice Obtained Directly from Aerosol Extinction Spectra. *J. Phys. Chem.* **1995**, *99* (17), 6317–6326. https://doi.org/10.1021/j100017a010.

(134) Xiao, S.; Figge, F.; Stirnemann, G.; Laage, D.; McGuire, J. A. Orientational Dynamics of Water at an Extended Hydrophobic Interface. *J. Am. Chem. Soc.* **2016**, *138* (17), 5551–5560. https://doi.org/10.1021/jacs.6b01820.

(135) Stiopkin, I. V; Weeraman, C.; Pieniazek, P. A.; Shalhout, F. Y.; Skinner, J. L.; Benderskii, A. V. Hydrogen Bonding at the Water Surface Revealed by Isotopic Dilution Spectroscopy. *Nature* **2011**, *474* (7350), 192–195. https://doi.org/10.1038/nature10173.

(136) Kang, H. Chemistry of Ice Surfaces. Elementary Reaction Steps on Ice Studied by Reactive Ion Scattering. *Acc. Chem. Res.* **2005**, *38* (12), 893–900. https://doi.org/10.1021/ar0501471.

(137) Jung, K.-H.; Park, S.-C.; Kim, J.-H.; Kang, H. Vertical Diffusion of Water Molecules near the Surface of Ice. *Ih J. Chem. Phys.* **2004**, *121*, 3886. https://doi.org/10.1063/1.1770518.

(138) Kahan, T. F.; Donaldson, D. J. Photolysis of Polycyclic Aromatic Hydrocarbons on Water and Ice Surfaces. *J. Phys. Chem. A* **2007**, *111* (7), 1277–1285. https://doi.org/10.1021/jp066660t.

(139) Kahan, T. F.; Zhao, R.; Jumaa, K. B.; Donaldson, D. J. Anthracene Photolysis in Aqueous Solution and Ice: Photon Flux Dependence and Comparison of Kinetics in Bulk Ice and at the Air–Ice Interface. *Environ. Sci. Technol.* **2010**, *44* (4), 1302–1306. https://doi.org/10.1021/es9031612.

(140) Murray, B. J.; O'Sullivan, D.; Atkinson, J. D.; Webb, M. E. Ice Nucleation by Particles Immersed in Supercooled Cloud Droplets. *Chem. Soc. Rev.* **2012**, *41* (19), 6519. https://doi.org/10.1039/c2cs35200a.

(141) Bartels-Rausch, T. Ten Things We Need to Know about Ice and Snow. *Nature* **2013**, *494* (7435), 27–29. https://doi.org/10.1038/494027a.

(142) Slater, B.; Michaelides, A.; Salzmann, C. G.; Lohmann, U. A Blue-Sky Approach to Understanding Cloud Formation. *Bull. Am. Meteorol. Soc.* **2016**, *97* (10), 1797–1802. https://doi.org/10.1175/BAMS-D-15-00131.1.

(143) Massie, I.; Selden, C.; Hodgson, H.; Fuller, B.; Gibbons, S.; Morris, G. J. GMP Cryopreservation of Large Volumes of Cells for Regenerative Medicine: Active Control of the Freezing Process. *Tissue Eng. Part C Methods* **2014**, *20* (9), 693–702. https://doi.org/10.1089/ten.tec.2013.0571.

(144) Asghar, W.; El Assal, R.; Shafiee, H.; Anchan, R. M.; Demirci, U. Preserving Human Cells for Regenerative, Reproductive, and Transfusion Medicine. *Biotechnol. J.* **2014**, *9* (7), 895–903. https://doi.org/10.1002/biot.201300074.

(145) Neves, L. S.; Rodrigues, M. T.; Reis, R. L.; Gomes, M. E. Current Approaches and Future Perspectives on Strategies for the Development of Personalized Tissue Engineering Therapies. *Expert Rev. Precis. Med. Drug Dev.* **2016**, *1* (1), 93–108. https://doi.org/10.1080/23808993.2016.1140004.

(146) Gurruchaga, H.; Saenz del Burgo, L.; Hernandez, R. .; Orive, G.; Selden, C.; Fuller, B.; Ciriza, J.; Pedraz, J. . Advances in the Slow Freezing Cryopreservation of Microencapsulated Cells. *J. Control. Release* **2018**, *281*, 119–138. https://doi.org/10.1016/j.jconrel.2018.05.016.

(147) Sosso, G. C.; Chen, J.; Cox, S. J.; Fitzner, M.; Pedevilla, P.; Zen, A.; Michaelides, A. Crystal Nucleation in Liquids: Open Questions and Future Challenges in Molecular Dynamics Simulations. *Chem. Rev.* **2016**, *116* (12), 7078–7116. https://doi.org/10.1021/acs.chemrev.5b00744.

(148) Whale, T. F.; Rosillo-Lopez, M.; Murray, B. J.; Salzmann, C. G. Ice Nucleation Properties of Oxidized Carbon Nanomaterials. *J. Phys. Chem. Lett.* **2015**, *6* (15), 3012–3016. https://doi.org/10.1021/acs.jpclett.5b01096.

(149) Kiselev, A.; Bachmann, F.; Pedevilla, P.; Cox, S. J.; Michaelides, A.; Gerthsen, D.; Leisner, T. Active Sites in Heterogeneous Ice Nucleation—the Example of K-Rich Feldspars. *Science.* **2017**, *355* (6323), 367–371. https://doi.org/10.1126/science.aai8034.

(150) Harrison, A. D.; Whale, T. F.; Carpenter, M. A.; Holden, M. A.; Neve, L.; O'Sullivan, D.; Vergara Temprado, J.; Murray, B. J. Not All Feldspars Are Equal: A Survey of Ice Nucleating Properties across the Feldspar Group of Minerals. *Atmos. Chem. Phys.* **2016**, *16* (17), 10927–10940. https://doi.org/10.5194/acp-16-10927-2016.

(151) Turner, M. A.; Arellano, F.; Kozloff, L. M. Three Separate Classes of Bacterial Ice Nucleation Structures. *J. Bacteriol.* **1990**, *172* (5), 2521–2526. https://doi.org/10.1128/jb.172.5.2521-2526.1990.

(152) Gurian-Sherman, D.; Lindow, S. E. Bacterial Ice Nucleation: Significance and Molecular Basis. *FASEB J.* **1993**, *7* (14), 1338–1343. https://doi.org/10.1096/fasebj.7.14.8224607.

(153) Pummer, B. G.; Bauer, H.; Bernardi, J.; Bleicher, S.; Grothe, H. Suspendable Macromolecules Are Responsible for Ice Nucleation Activity of Birch and Conifer Pollen. *Atmos. Chem. Phys.* **2012**, *12* (5), 2541–2550. https://doi.org/10.5194/acp-12-2541-2012.

(154) O'Sullivan, D.; Murray, B. J.; Ross, J. F.; Whale, T. F.; Price, H. C.; Atkinson, J. D.; Umo, N. S.; Webb, M. E. The Relevance of Nanoscale Biological Fragments for Ice Nucleation in Clouds. *Sci. Rep.* **2015**, *5* (1), 8082. https://doi.org/10.1038/srep08082.

(155) Hudait, A.; Odendahl, N.; Qiu, Y.; Paesani, F.; Molinero, V. Ice-Nucleating and Antifreeze Proteins Recognize Ice through a Diversity of Anchored Clathrate and Ice-like Motifs. *J. Am. Chem. Soc.* **2018**, *140* (14), 4905–4912. https://doi.org/10.1021/jacs.8b01246.

(156) Fitzner, M.; Sosso, G. C.; Cox, S. J.; Michaelides, A. The Many Faces of Heterogeneous Ice Nucleation: Interplay Between Surface Morphology and Hydrophobicity. *J. Am. Chem. Soc.* **2015**, *137* (42), 13658–13669. https://doi.org/10.1021/jacs.5b08748.

(157) Sosso, G. C.; Tribello, G. A.; Zen, A.; Pedevilla, P.; Michaelides, A. Ice Formation on Kaolinite: Insights from Molecular Dynamics Simulations. *J. Chem. Phys.* **2016**, *145* (21), 211927. https://doi.org/10.1063/1.4968796.

(158) Sosso, G. C.; Li, T.; Donadio, D.; Tribello, G. A.; Michaelides, A. Microscopic Mechanism and Kinetics of Ice Formation at Complex Interfaces: Zooming in on Kaolinite. *J. Phys. Chem. Lett.* **2016**, *7* (13), 2350–2355. https://doi.org/10.1021/acs.jpclett.6b01013.

(159) Zielke, S. A.; Bertram, A. K.; Patey, G. N. Simulations of Ice Nucleation by Kaolinite (001) with Rigid and Flexible Surfaces. *J. Phys. Chem. B* **2016**, *120* (8), 1726–1734. https://doi.org/10.1021/acs.jpcb.5b09052.

(160) Zhang, X.-X.; Chen, M.; Fu, M. Impact of Surface Nanostructure on Ice Nucleation. *J. Chem. Phys.* **2014**, *141* (12), 124709. https://doi.org/10.1063/1.4896149.

(161) Bi, Y.; Cabriolu, R.; Li, T. Heterogeneous Ice Nucleation Controlled by the Coupling of Surface Crystallinity and Surface Hydrophilicity. *J. Phys. Chem. C* **2016**, *120* (3), 1507–1514. https://doi.org/10.1021/acs.jpcc.5b09740.

(162) Reinhardt, A.; Doye, J. P. K. Effects of Surface Interactions on Heterogeneous Ice Nucleation for a Monatomic Water Model. *J. Chem. Phys.* **2014**, *141* (8), 084501. https://doi.org/10.1063/1.4892804.

(163) Fraux, G.; Doye, J. P. K. Note: Heterogeneous Ice Nucleation on Silver-Iodide-like Surfaces. *J. Chem. Phys.* **2014**, *141* (21), 216101. https://doi.org/10.1063/1.4902382.

(164) Pedevilla, P.; Fitzner, M.; Michaelides, A. What Makes a Good Descriptor for Heterogeneous Ice Nucleation on OH-Patterned Surfaces. *Phys. Rev. B* **2017**, *96* (11), 115441. https://doi.org/10.1103/PhysRevB.96.115441.

(165) Lupi, L.; Hanscam, R.; Qiu, Y.; Molinero, V. Reaction Coordinate for Ice Crystallization on a Soft Surface. *J. Phys. Chem. Lett.* **2017**, *8* (17), 4201–4205. https://doi.org/10.1021/acs.jpclett.7b01855.

(166) Bi, Y.; Cao, B.; Li, T. Enhanced Heterogeneous Ice Nucleation by Special Surface Geometry. *Nat. Commun.* **2017**, *8* (1), 15372. https://doi.org/10.1038/ncomms15372.

(167) Qiu, Y.; Hudait, A.; Molinero, V. How Size and Aggregation of Ice-Binding Proteins Control Their Ice Nucleation

Efficiency. *J. Am. Chem. Soc.* **2019**, *141* (18), 7439–7452. https://doi.org/10.1021/jacs.9b01854.
(168) Factorovich, M. H.; Naullage, P. M.; Molinero, V. Can Clathrates Heterogeneously Nucleate Ice? *J. Chem. Phys.* **2019**, *151* (11), 114707. https://doi.org/10.1063/1.5119823.
(169) Diao, Y.; Myerson, A. S.; Hatton, T. A.; Trout, B. L. Surface Design for Controlled Crystallization: The Role of Surface Chemistry and Nanoscale Pores in Heterogeneous Nucleation. *Langmuir* **2011**, *27* (9), 5324–5334. https://doi.org/10.1021/la104351k.
(170) Holbrough, J. L.; Campbell, J. M.; Meldrum, F. C.; Christenson, H. K. Topographical Control of Crystal Nucleation. *Cryst. Growth Des.* **2012**, *12* (2), 750–755. https://doi.org/10.1021/cg201084j.
(171) Campbell, J. M.; Meldrum, F. C.; Christenson, H. K. Observing the Formation of Ice and Organic Crystals in Active Sites. *Proc. Natl. Acad. Sci.* **2017**, *114* (5), 810–815. https://doi.org/10.1073/pnas.1617717114.
(172) Sosso, G. C.; Whale, T. F.; Holden, M. A.; Pedevilla, P.; Murray, B. J.; Michaelides, A. Unravelling the Origins of Ice Nucleation on Organic Crystals. *Chem. Sci.* **2018**, *9* (42), 8077–8088. https://doi.org/10.1039/C8SC02753F.
(173) Holden, M. A.; Whale, T. F.; Tarn, M. D.; O'Sullivan, D.; Walshaw, R. D.; Murray, B. J.; Meldrum, F. C.; Christenson, H. K. High-Speed Imaging of Ice Nucleation in Water Proves the Existence of Active Sites. *Sci. Adv.* **2019**, *5* (2), eaav4316. https://doi.org/10.1126/sciadv.aav4316.
(174) CRAVEN, B. M. Crystal Structure of Cholesterol Monohydrate. *Nature* **1976**, *260* (5553), 727–729. https://doi.org/10.1038/260727a0.
(175) Zhang, L.; Hao, C.; Xu, G.; Sun, R. Effects of Concentration and Surface Pressure on MBP Interaction with Cholesterol in Langmuir Films. *Scanning* **2017**, *2017*, 1–9. https://doi.org/10.1155/2017/1542156.
(176) Przykaza, K.; Woźniak, K.; Jurak, M.; Wiącek, A. E.; Mroczka, R. Properties of the Langmuir and Langmuir–Blodgett Monolayers of Cholesterol-Cyclosporine A on Water and Polymer Support. *Adsorption* **2019**, *25* (4), 923–936. https://doi.org/10.1007/s10450-019-00117-2.
(177) HEAD, R. B. Steroids as Ice Nucleators. *Nature* **1961**, *191* (4793), 1058–1059. https://doi.org/10.1038/1911058a0.
(178) Fukuta, N.; Mason, B. . Epitaxial Growth of Ice on Organic Crystals. *J. Phys. Chem. Solids* **1963**, *24* (6), 715–718. https://doi.org/10.1016/0022-3697(63)90217-8.
(179) Kunert, A. T.; Lamneck, M.; Helleis, F.; Pöschl, U.; Pöhlker, M. L.; Fröhlich-Nowoisky, J. Twin-Plate Ice Nucleation Assay (TINA) with Infrared Detection for High-Throughput Droplet Freezing Experiments with Biological Ice Nuclei in Laboratory and Field Samples. *Atmos. Meas. Tech.* **2018**, *11* (11), 6327–6337. https://doi.org/10.5194/amt-11-6327-2018.
(180) Vali, G. Revisiting the Differential Freezing Nucleus Spectra Derived from Drop-Freezing Experiments: Methods of Calculation, Applications, and Confidence Limits. *Atmos. Meas. Tech.* **2019**, *12* (2), 1219–1231. https://doi.org/10.5194/amt-12-1219-2019.
(181) Bjelkmar, P.; Larsson, P.; Cuendet, M. A.; Hess, B.; Lindahl, E. Implementation of the CHARMM Force Field in GROMACS: Analysis of Protein Stability Effects from Correction Maps, Virtual Interaction Sites, and Water Models. *J. Chem. Theory Comput.* **2010**, *6* (2), 459–466. https://doi.org/10.1021/ct900549r.
(182) Lim, J. B.; Rogaski, B.; Klauda, J. B. Update of the Cholesterol Force Field Parameters in CHARMM. *J. Phys. Chem. B* **2012**, *116* (1), 203–210. https://doi.org/10.1021/jp207925m.
(183) Abascal, J. L. F.; Sanz, E.; García Fernández, R.; Vega, C. A Potential Model for the Study of Ices and Amorphous Water: TIP4P/Ice. *J. Chem. Phys.* **2005**, *122* (23), 234511. https://doi.org/10.1063/1.1931662.
(184) Nutt, D. R.; Smith, J. C. Molecular Dynamics Simulations of Proteins: Can the Explicit Water Model Be Varied? *J. Chem. Theory Comput.* **2007**, *3* (4), 1550–1560. https://doi.org/10.1021/ct700053u.
(185) Lee, H. Structures, Dynamics, and Hydrogen-Bond Interactions of Antifreeze Proteins in TIP4P/Ice Water and Their Dependence on Force Fields. *PLoS One* **2018**, *13* (6), e0198887. https://doi.org/10.1371/journal.pone.0198887.
(186) Sajadi, F.; Rowley, C. The CHARMM36 Force Field for Lipids Can Be Used With More Accurate Water Models. **2018**. https://doi.org/10.26434/chemrxiv.6137474.v1 D O I: 10.26434/chemrxiv.6137474.v1.
(187) Van Der Spoel, D.; Lindahl, E.; Hess, B.; Groenhof, G.; Mark, A. E.; Berendsen, H. J. C. GROMACS: Fast, Flexible, and Free. *J. Comput. Chem.* **2005**, *26* (16), 1701–1718. https://doi.org/10.1002/jcc.20291.
(188) Venable, R. M.; Skibinsky, A.; Pastor, R. W. Constant Surface Tension Molecular Dynamics Simulations of Lipid Bilayers with Trehalose. *Mol. Simul.* **2006**, *32* (10–11), 849–855. https://doi.org/10.1080/08927020600615018.
(189) Van Gunsteren, W. F.; Berendsen, H. J. C. A Leap-Frog Algorithm for Stochastic Dynamics. *Mol. Simul.* **1988**, *1* (3), 173–185. https://doi.org/10.1080/08927028808080941.
(190) Bussi, G.; Donadio, D.; Parrinello, M. Canonical Sampling through Velocity Rescaling. *J. Chem. Phys.* **2007**, *126* (1), 014101. https://doi.org/10.1063/1.2408420.
(191) Berendsen, H. J. C.; Postma, J. P. M.; van Gunsteren, W. F.; DiNola, A.; Haak, J. R. Molecular Dynamics with Coupling to an External Bath. *J. Chem. Phys.* **1984**, *81* (8), 3684–3690. https://doi.org/10.1063/1.448118.
(192) Hess, B.; Bekker, H.; Berendsen, H. J. C.; Fraaije, J. G. E. M. LINCS: A Linear Constraint Solver for Molecular

Simulations. *J. Comput. Chem.* **1997**, *18* (12), 1463–1472. https://doi.org/10.1002/(SICI)1096-987X(199709)18:12<1463::AID-JCC4>3.0.CO;2-H.

(193) Miyamoto, S.; Kollman, P. A. Settle: An Analytical Version of the SHAKE and RATTLE Algorithm for Rigid Water Models. *J. Comput. Chem.* **1992**, *13* (8), 952–962. https://doi.org/10.1002/jcc.540130805.

(194) Bostick, D.; Berkowitz, M. L. The Implementation of Slab Geometry for Membrane-Channel Molecular Dynamics Simulations. *Biophys. J.* **2003**, *85* (1), 97–107. https://doi.org/10.1016/S0006-3495(03)74458-0.

(195) Wang, Y.; Teitel, S.; Dellago, C. Melting of Icosahedral Gold Nanoclusters from Molecular Dynamics Simulations. *J. Chem. Phys.* **2005**, *122* (21), 214722. https://doi.org/10.1063/1.1917756.

(196) Steinhardt, P. J.; Nelson, D. R.; Ronchetti, M. Bond-Orientational Order in Liquids and Glasses. *Phys. Rev. B* **1983**, *28* (2), 784–805. https://doi.org/10.1103/PhysRevB.28.784.

(197) Backus, E. H. G.; Bonn, D.; Cantin, S.; Roke, S.; Bonn, M. Laser-Heating-Induced Displacement of Surfactants on the Water Surface. *J. Phys. Chem. B* **2012**, *116* (9), 2703–2712. https://doi.org/10.1021/jp2074545.

(198) Whale, T. F.; Holden, M. A.; Kulak, A. N.; Kim, Y.-Y.; Meldrum, F. C.; Christenson, H. K.; Murray, B. J. The Role of Phase Separation and Related Topography in the Exceptional Ice-Nucleating Ability of Alkali Feldspars. *Phys. Chem. Chem. Phys.* **2017**, *19* (46), 31186–31193. https://doi.org/10.1039/C7CP04898J.

(199) Holden, M. A.; Campbell, J. M.; Meldrum, F. C.; Murray, B. J.; Christenson, H. K. Active Sites for Ice Nucleation Differ Depending on Nucleation Mode. *Proc. Natl. Acad. Sci.* **2021**, *118* (18), e2022859118. https://doi.org/10.1073/pnas.2022859118.

(200) Rapaport, H.; Kuzmenko, I.; Lafont, S.; Kjaer, K.; Howes, P. B.; Als-Nielsen, J.; Lahav, M.; Leiserowitz, L. Cholesterol Monohydrate Nucleation in Ultrathin Films on Water. *Biophys. J.* **2001**, *81* (5), 2729–2736. https://doi.org/10.1016/S0006-3495(01)75915-2.

(201) Polen, M.; Brubaker, T.; Somers, J.; Sullivan, R. C. Cleaning up Our Water: Reducing Interferences from Nonhomogeneous Freezing of "Pure" Water in Droplet Freezing Assays of Ice-Nucleating Particles. *Atmos. Meas. Tech.* **2018**, *11* (9), 5315–5334. https://doi.org/10.5194/amt-11-5315-2018.

(202) Daily, M. I.; Whale, T. F.; Partanen, R.; Harrison, A. D.; Kilbride, P.; Lamb, S.; Morris, G. J.; Picton, H. M.; Murray, B. J. Cryopreservation of Primary Cultures of Mammalian Somatic Cells in 96-Well Plates Benefits from Control of Ice Nucleation. *Cryobiology* **2020**, *93*, 62–69. https://doi.org/10.1016/j.cryobiol.2020.02.008.

(203) Del Castillo-Santaella, T.; Maldonado-Valderrama, J.; Faraudo, J.; Martín-Molina, A. Specific Ion Effects in Cholesterol Monolayers. *Materials (Basel).* **2016**, *9* (5), 340. https://doi.org/10.3390/ma9050340.

(204) Cadena-Nava, R. D.; Martin-Mirones, J. M.; Vázquez-Martínez, E. A.; Roca, J. A.; Ruiz-García, J. Direct Observations of Phase Changes in Langmuir Films of Cholesterol. *Rev. Mex. Física* **2006**, *52* (5), 32–40.

(205) Can, S. Z.; Chang, C. F.; Walker, R. A. Spontaneous Formation of DPPC Monolayers at Aqueous/Vapor Interfaces and the Impact of Charged Surfactants. *Biochim. Biophys. Acta - Biomembr.* **2008**, *1778* (10), 2368–2377. https://doi.org/10.1016/j.bbamem.2008.06.002.

(206) Qi, L.; Fresnais, J.; Muller, P.; Theodoly, O.; Berret, J.-F.; Chapel, J.-P. Interfacial Activity of Phosphonated-PEG Functionalized Cerium Oxide Nanoparticles. *Langmuir* **2012**, *28* (31), 11448–11456. https://doi.org/10.1021/la302173g.

(207) Ulaganathan, V.; Fainerman, V. B.; Gochev, G.; Aksenenko, E. V.; Gunes, D. Z.; Gehin-Delval, C.; Miller, R. Evidence of Negative Surface Pressure Induced by β-Lactoglobulin and β-Casein at Water/Air Interface. *Food Hydrocoll.* **2014**, *34*, 10–14. https://doi.org/10.1016/j.foodhyd.2013.03.019.

(208) Fitzner, M.; Sosso, G. C.; Pietrucci, F.; Pipolo, S.; Michaelides, A. Pre-Critical Fluctuations and What They Disclose about Heterogeneous Crystal Nucleation. *Nat. Commun.* **2017**, *8* (1), 2257. https://doi.org/10.1038/s41467-017-02300-x.

(209) Malkin, T. L.; Murray, B. J.; Salzmann, C. G.; Molinero, V.; Pickering, S. J.; Whale, T. F. Stacking Disorder in Ice I. *Phys. Chem. Chem. Phys.* **2015**, *17* (1), 60–76. https://doi.org/10.1039/C4CP02893G.

(210) Quigley, D. Communication: Thermodynamics of Stacking Disorder in Ice Nuclei. *J. Chem. Phys.* **2014**, *141* (12), 121101. https://doi.org/10.1063/1.4896376.

(211) Lupi, L.; Hudait, A.; Peters, B.; Grünwald, M.; Gotchy Mullen, R.; Nguyen, A. H.; Molinero, V. Role of Stacking Disorder in Ice Nucleation. *Nature* **2017**, *551* (7679), 218–222. https://doi.org/10.1038/nature24279.

(212) Haji-Akbari, A.; Debenedetti, P. G. Direct Calculation of Ice Homogeneous Nucleation Rate for a Molecular Model of Water. *Proc. Natl. Acad. Sci.* **2015**, *112* (34), 10582–10588. https://doi.org/10.1073/pnas.1509267112.

(213) Roeters, S. J.; Golbek, T. W.; Bregnhøj, M.; Drace, T.; Alamdari, S.; Roseboom, W.; Kramer, G.; Šantl-Temkiv, T.; Finster, K.; Pfaendtner, J.; Woutersen, S.; Boesen, T.; Weidner, T. Ice-Nucleating Proteins Are Activated by Low Temperatures to Control the Structure of Interfacial Water. *Nat. Commun.* **2021**, *12* (1), 1183. https://doi.org/10.1038/s41467-021-21349-3.

(214) Metya, A. K.; Molinero, V. Is Ice Nucleation by Organic Crystals Nonclassical? An Assessment of the Monolayer Hypothesis of Ice Nucleation. *J. Am. Chem. Soc.* **2021**, *143* (12), 4607–4624. https://doi.org/10.1021/jacs.0c12012.

(215) DeMott, P. J.; Mason, R. H.; McCluskey, C. S.; Hill, T. C. J.; Perkins, R. J.; Desyaterik, Y.; Bertram, A. K.; Trueblood, J. V.; Grassian, V. H.; Qiu, Y.; Molinero, V.; Tobo, Y.; Sultana, C. M.; Lee, C.; Prather, K. A. Ice Nucleation by Particles Containing Long-Chain Fatty Acids of Relevance to Freezing by Sea Spray Aerosols. *Environ. Sci. Process. Impacts* **2018**, *20* (11), 1559–1569. https://doi.org/10.1039/c8em00386f.

(216) Gavish, M.; Popovitz-Biro, R.; Lahav, M.; Leiserowitz, L. Ice Nucleation by Alcohols Arranged in Monolayers at the Surface of Water Drops. *Science.* **1990**, *250* (4983), 973–975. https://doi.org/10.1126/science.250.4983.973.

(217) Popovitz-Biro, R.; Gavish, M.; Lahav, M.; Leiserowitz, L. Ice Nucleation by Monolayers of Aliphatic Alcohols. *Makromol. Chemie. Macromol. Symp.* **1991**, *46* (1), 125–132. https://doi.org/10.1002/masy.19910460116.

(218) Qiu, Y.; Odendahl, N.; Hudait, A.; Mason, R.; Bertram, A. K.; Paesani, F.; DeMott, P. J.; Molinero, V. Ice Nucleation Efficiency of Hydroxylated Organic Surfaces Is Controlled by Their Structural Fluctuations and Mismatch to Ice. *J. Am. Chem. Soc.* **2017**, *139* (8), 3052–3064. https://doi.org/10.1021/jacs.6b12210.

(219) Toner, M.; Cravalho, E. G.; Karel, M. Cellular Response of Mouse Oocytes to Freezing Stress: Prediction of Intracellular Ice Formation. *J. Biomech. Eng.* **1993**, *115* (2), 169–174. https://doi.org/10.1115/1.2894117.

(220) Acker, J. P.; Elliott, J. A. W.; McGann, L. E. Intercellular Ice Propagation: Experimental Evidence for Ice Growth through Membrane Pores. *Biophys. J.* **2001**, *81* (3), 1389–1397. https://doi.org/10.1016/S0006-3495(01)75794-3.

(221) Mazur, P. 2. Roles of Intracellular Ice Formation, Vitrification of Cell Water, and Recrystallization of Intracellular Ice on the Survival of Mouse Embryos and Oocytes. *Cryobiology* **2012**, *65* (3), 339. https://doi.org/10.1016/j.cryobiol.2012.07.003.

(222) Yi, J.; Liang, X. M.; Zhao, G.; He, X. An Improved Model for Nucleation-Limited Ice Formation in Living Cells during Freezing. *PLoS One* **2014**, *9* (5), e98132. https://doi.org/10.1371/journal.pone.0098132.

(223) Hoose, C.; Kristjánsson, J. E.; Burrows, S. M. How Important Is Biological Ice Nucleation in Clouds on a Global Scale? *Environ. Res. Lett.* **2010**, *5* (2), 024009. https://doi.org/10.1088/1748-9326/5/2/024009.

(224) Hoose, C.; Möhler, O. Heterogeneous Ice Nucleation on Atmospheric Aerosols: A Review of Results from Laboratory Experiments. *Atmos. Chem. Phys.* **2012**, *12* (20), 9817–9854. https://doi.org/10.5194/acp-12-9817-2012.

(225) Augustin, S.; Wex, H.; Niedermeier, D.; Pummer, B.; Grothe, H.; Hartmann, S.; Tomsche, L.; Clauss, T.; Voigtländer, J.; Ignatius, K.; Stratmann, F. Immersion Freezing of Birch Pollen Washing Water. *Atmos. Chem. Phys.* **2013**, *13* (21), 10989–11003. https://doi.org/10.5194/acp-13-10989-2013.

(226) Kajava, A. V.; Lindow, S. E. A Model of the Three-Dimensional Structure of Ice Nucleation Proteins. *J. Mol. Biol.* **1993**, *232* (3), 709–717. https://doi.org/10.1006/jmbi.1993.1424.

(227) Liu, K.; Wang, C.; Ma, J.; Shi, G.; Yao, X.; Fang, H.; Song, Y.; Wang, J. Janus Effect of Antifreeze Proteins on Ice Nucleation. *Proc. Natl. Acad. Sci.* **2016**, *113* (51), 14739–14744. https://doi.org/10.1073/pnas.1614379114.

(228) Dreischmeier, K.; Budke, C.; Wiehemeier, L.; Kottke, T.; Koop, T. Boreal Pollen Contain Ice-Nucleating as Well as Ice-Binding 'Antifreeze' Polysaccharides. *Sci. Rep.* **2017**, *7* (1), 41890. https://doi.org/10.1038/srep41890.

(229) Ling, M. L.; Wex, H.; Grawe, S.; Jakobsson, J.; Löndahl, J.; Hartmann, S.; Finster, K.; Boesen, T.; Šantl-Temkiv, T. Effects of Ice Nucleation Protein Repeat Number and Oligomerization Level on Ice Nucleation Activity. *J. Geophys. Res. Atmos.* **2018**, *123* (3), 1802–1810. https://doi.org/10.1002/2017JD027307.

Summary

Water has a 71% coverage on Earth, of which only 0.001% is present in the atmosphere in the form of small droplets, ice crystals, and water vapour. Despite a small fraction, water in its condensed states in the atmosphere has implications in heterogeneous photochemical reactions, most notable being the catalysis of ozone hole formation on crystalline ice surfaces. Understanding molecular structure, dynamics and energy transfer pathways at water interfaces, which are the immediate reaction sites, are thus a gateway to understanding fundamentally relevant physical, chemical and biological processes. Vibrational spectroscopy is a suitable method to study the dynamic cohesive three-dimensional hydrogen bond network of water in its liquid and solid states. The vibrational modes of water are sensitive to the hydrogen bond environment and provide information on the hydrogen bond strength and types. By using the second-order non-linear technique Sum Frequency Generation (SFG) spectroscopy in the Infrared frequency range, vibrational properties of specifically the interface can be obtained. This thesis is a comprehensive study of the interfacial vibrational properties of water in its solid and liquid states, to answer fundamental questions on the microscopic differences we observe for the two states.

The first experimental chapter is centred on probing the spectral region around 1600 cm^{-1} where we perform the first H-O-H vibrational bend mode measurements of interfacial ice. From isotopic dilution measurements on water, it is known that the vibrational bend mode is less influenced by intermolecular coupling compared to the stretch region, making it interesting to study systems without spectral complications due to intermolecular coupling effects. The bend mode is also important for vibrational relaxation mechanisms, acting as an intermediate between the high-frequency stretch, and the low-frequency librational and rotational bands. Surprisingly, the interfacial vibrational bend mode of ice is considerably wider in comparison to liquid water. In contrast, the vibrational stretch band of ice is considerably narrower for ice than water. Moreover, the vibrational stretch mode in its intensity and central frequency is strongly temperature dependent, while hardly any temperature effects were observed for the bend mode. Our measurements reveal that the ice bend mode is primarily homogeneously broadened. This is an interesting result, pointing towards ultrafast pure dephasing of the bend mode, thereby asserting the importance of the bend mode region for energy transfer mechanisms. Further comparison of the bend mode for ice and water, and differences to the stretch mode shed more light on the structure of interfacial ice.

The second experimental chapter explores the possibility of proton order at the ice interface. It is known that the bulk of ice, although having an ordered crystalline arrangement of oxygen atoms, has a disordered hydrogen arrangement throughout the entire temperature range till absolute zero. At the surface however, due to different electrostatics than in the bulk, reconstruction of the proton arrangement is proposed to occur. We measure the -OH stretch vibrational SFG spectra of ice, ranging from the low-frequency strongly hydrogen-bonded, to the high-frequency free-OH region, as a function of temperature. The low-frequency 3200 cm^{-1} stretch region, being sensitive to relative orientation of dipoles, is a potential measure of the orientational disorder of water molecules at the ice surface. Experimental measurements are correlated to calculated SFG spectra in an attempt to unravel the nature and mechanism of proton ordering on the surface of ice. Estimations of the enthalpic and entropic contributions of differently proton-ordered surfaces are performed to complement the simulation models and experimental data. Our understanding is far from complete, and through our thorough analysis we hope to be able to encourage further experimental and

theoretical work in this direction. Specifically, simple entropic and enthalpic contributions do not sustain in the temperature range of our experimental study; the data however could be described by a simple disordered to ordered transition, with an associated reaction enthalpy.

The third experimental chapter uses an advanced pump-probe scheme of SFG spectroscopy to perform time-resolved measurements in the vibrational stretch region of interfacial ice. We employed the pump-probe method on both ice and water, in the hydrogen-bonded and the free-OH stretch region, to elucidate vibrational relaxation dynamics of the two systems. We find a faster relaxation time constant for ice in the hydrogen-bonded region compared to water, but surprisingly a rather slow time constant in the free-OH region. These differences in dynamics can point towards differences in photochemical reaction mechanisms for ice and water. Specifically, our results potentially shed light on the efficient catalytic properties of ice, possibly explained due to better adsorption of species on the ice surface because of slower re-orientation of the free-OH species, when compared to water.

Finally, the last experimental chapter is focussed on understanding if the molecular structure or the structural order is majorly accountable for the ice nucleation efficiency of a substance. We looked at the water-cholesterol interface, combining SFG experiments, ice nucleation assay experiments, and MD simulations to understand the ice nucleating activities of cholesterol in its crystalline and monolayer forms. From a comparison of the different physical forms explored of the same ice nucleating agent cholesterol, varying in structure flexibility and order, we conclude that order outweighs molecular structure, as the ordering of the monolayer directly impacts the ice nucleating efficiency. This work may provide some guidelines into designing of next-generation ice-nucleating agents, especially focussing on its supra-molecular chemistry.

Samenvatting

71% van de aarde is bedekt met water. Slechts 0,001% daarvan is aanwezig in de atmosfeer in de vorm van kleine druppels, ijskristallen en waterdamp. Ondanks zijn kleine fractie heeft water in gecondenseerde toestand in de atmosfeer belangrijke implicaties in heterogene fotochemische reacties, met als meest opmerkelijke de katalyse van de vorming van ozongaten aan kristallijne ijsoppervlakken. Inzicht in de moleculaire structuur van en de dynamica en energieoverdracht aan wateroppervlakken, is dus belangrijk om fysische, chemische en biologische processen te begrijpen. Vibratiespectroscopie is een geschikte methode om het dynamische driedimensionale waterstofbruggennetwerk van water in zijn vloeibare en vaste toestand te bestuderen. De trillingsmodes van water zijn gevoelig voor de waterstofbrug omgeving en geven informatie over de waterstofbrug sterkte en types. Door gebruik te maken van de tweede-orde niet-lineaire techniek somfrequentiegeneratie (SFG) spectroscopie in het infrarode frequentiegebied, kunnen vibratie-eigenschappen van specifiek het oppervlak worden verkregen. Dit proefschrift gebruikt de vibratie-eigenschappen van water aan een oppervlak in zijn vaste en vloeibare toestand, om fundamentele vragen te beantwoorden over de microscopische verschillen die we waarnemen voor de twee toestanden.

Het eerste experimentele hoofdstuk is gericht op het spectrale gebied rond 1600 cm^{-1} waar we voor de eerste keer de H-O-H buigvibratie van het oppervlak van ijs hebben kunnen meten. Uit isotopische verdunningsmetingen aan water is bekend dat de buigvibratie minder wordt beïnvloed door intermoleculaire koppeling dan de strekvibratie; deze vibratie maakt het dus mogelijk water te bestuderen bijna zonder spectrale complicaties als gevolg van intermoleculaire koppelingseffecten. De buigvibratie is ook belangrijk voor trillingsrelaxatiemechanismen, omdat deze vibratie fungeert als een intermediair tussen de hoogfrequente strekband en de laagfrequente librationele en rotationele banden. Onze data laten zien dat de buigmodus van ijs aan het ijs-lucht grensvlak aanzienlijk breder is in vergelijking met vloeibaar water. Daarentegen is de strekvibratieband van ijs aanzienlijk smaller dan die van water. Bovendien is de intensiteit en de centrale frequentie van de strekvibratieband sterk afhankelijk van de temperatuur, terwijl er nauwelijks temperatuureffecten zijn waargenomen bij de buigvibratieband. Onze metingen laten zien dat de buigmodus van ijs voornamelijk homogeen verbreed is. Dit is een interessant resultaat, dat wijst op ultrasnelle pure dephasing van de buigmodus, waarmee het belang van de buigmodus voor energieoverdracht wordt bevestigd. Verdere vergelijking van de buigmodus voor ijs en water, en verschillen met de strekmodus werpen meer licht op de structuur van oppervlakte-ijs.

Het tweede experimentele hoofdstuk onderzoekt de mogelijkheid van protonorde aan het grensvlak van ijs. Hoewel in bulk ijs de zuurstofatomen volgens het kristalrooster zeer geordend zijn, zijn de waterstofatomen over het gehele temperatuurbereik tot aan het absolute nulpunt zeer ongeordend. Aan het oppervlak echter, als gevolg van een andere elektrostatica dan in de bulk, zou een reconstructie van de protonorde plaats moeten kunnen vinden. Met SFG hebben we de O-H strekvibratie van ijs, in het waterstofgebonden en het vrije O-H gebied, als functie van de temperatuur gemeten. Het signaal bij 3200 cm^{-1} van de waterstofgebrugde molekulen is gevoelig voor de relatieve oriëntatie van dipolen en dus een potentiële maat voor de oriëntatie van watermoleculen aan het ijsoppervlak. De experimenten worden gecorreleerd aan berekende SFG spectra in een poging om de aard en het mechanisme van proton ordening aan het oppervlak van ijs te ontrafelen. Schattingen van de enthalpische en entropische bijdragen van verschillend proton-geordende oppervlakken worden uitgevoerd om de simulatiemodellen en experimentele gegevens aan te vullen. Ons inzicht is verre van volledig. Door onze grondige analyse hopen we toekomstig experimenteel en

theoretisch werk in deze richting te kunnen aanmoedigen. In het bijzonder, de eenvoudige entropische en enthalpische bijdragen laten zien dat pas in de buurt van het absolute nulpunt protonorde aan het oppervlak plaats zou vinden. De experimenten kunnen beschreven worden door een eenvoudige ongeordende naar geordende overgang, met een bijbehorende reactie-enthalpie.

Het derde experimentele hoofdstuk maakt gebruik van een geavanceerd pomp-probe schema van SFG spectroscopie om tijdsopgeloste metingen uit te voeren in het strekvibratie gebied van het ijsoppervlak. We hebben de pomp-probe methode toegepast op zowel ijs als water, in het waterstof-gebonden en het vrije-OH strekgebied, om de dynamica van de trillingsrelaxatie van de twee systemen op te helderen. We vinden een snellere relaxatie voor ijs in het waterstof-gebonden gebied dan voor water, maar verrassend genoeg een eerder trage relaxatie in het vrije-OH gebied. Deze verschillen in dynamica kunnen wijzen op verschillen in fotochemische reactiemechanismen voor ijs en water. Meer specifiek, onze resultaten werpen mogelijk licht op de efficiënte katalytische eigenschappen van ijs, mogelijk te verklaren door betere adsorptie van molekulen aan het ijsoppervlak als gevolg van langzamere reoriëntatie van de molekulen met een vrije OH, vergeleken met water.

Het laatste experimentele hoofdstuk is gericht op de vraag of de moleculaire structuur of de ordening van de molekulen in belangrijke mate verantwoordelijk is voor de ijsvormingsefficiëntie van een stof. We hebben gekeken naar het grensvlak tussen water en cholesterol, waarbij we SFG-experimenten, ijsvormingsexperimenten en MD-simulaties hebben gecombineerd om te onderzoeken wat bepalende factoren zijn voor de formatie van ijs. We hebben cholesterol in twee verschillende fysische vormen, kristallijn en als monolaag vergeleken. We concluderen dat ordening zwaarder weegt dan moleculaire structuur, omdat de ordening van de monolaag direct van invloed is op de efficiëntie van ijsformatie. Dit werk kan een aantal richtlijnen geven voor het ontwerpen van de volgende generatie ijs-nucleatiemiddelen, waarbij de aandacht vooral uitgaat naar de supramoleculaire chemie.

Publications covered in the thesis

1. Sudera, P., Cyran, J.D., Deiseroth, M., Backus, E.H.G., Bonn, M. Interfacial Vibrational Dynamics of Ice Ih and Liquid Water. *J. Am. Chem. Soc.* 2020, 142, 28, 12005–12009.

2. Sudera, P., Cyran, J.D., Bonn, M, Backus, E.H.G., Interfacial Vibrational Spectroscopy of the Water Bending Mode on Ice Ih. Just *Published, J. Phys. Chem. C (2021)*. DOI: 10.1021/acs.jpcc.1c08046

3. Sosso, G.C., Sudera, P., Kunert, A.T., Whale, T.F., Fröhlich-Nowoisky, J., Bonn, M., Michaelides, A., Backus, E.H.G., Molecular Structure versus Structural Order: Understanding Heterogeneous Ice Nucleation. *Submitted*.

Acknowledgements

Ellen: for her availability (Vienna or Mainz, skype, call or in person, for problems in the lab, writing, understanding, thesis, ...), dedication, incredible patience (I'm sure i was not the easiest student ;)), quick-wittedness, dymanism, and her openness (to ideas, discussions, criticism, and acceptance). I could not have asked for more, thank you for your immense support and backing!

Mischa for being an epitome of conducting both excellent science and excellent presentation of the science, his expansive grasp on science, and his perceptional skills on mind-boggling levels.

Maksim, for his utmost patience, dedication and desire to make people understand things at a fundamental level. Discussions with you both in the lab and the office, have been the most enriching experiences for me scientifically.

Laurie: well besides the formal set of thanks that I owe you for being the best person at your job, thanks for being such a wonderful friend I could always rely on, for that extra little nudge that I needed way too many times, for being an ear to all my troubles and problems, for the deep conversations that connected us, for the coffee and focaccia times, and so much more.

Hansjörg and **Florian** for all the excellent technical help. Also **Yuki Nagata** and **Johannes Hunger** for excellent scientific help and discussions. **Christian Schneider** for all the print related help.

TeamIce #1 **Marc-Jan van Zadel**: for being an amazing team player, always in to help even if it means a weekend, and on both professional and personal fronts. "Care and Quality are internal and external aspects of the same thing. A person who sees Quality and feels it as he works is a person who cares. A person who cares about what he sees and does is a person who's bound to have some characteristic of quality."

TeamIce #2 **Jenee Cyran** #SFAM: need i say more? this would have not been anywhere the same without you, you just left too early, or i stayed too long :P well it started with optics and ice in the lab, to staring at the stars, to crazy defense preparations and carnivals, to a whole new level of connectedness. Thank you for being there, and also for (I hope the covid situation does not disappoint us) coming all the way to make it on the other side of my defense, in black ;)

Malte Deiseroth: we dealt with the same jazz, taming Python and unstable pumps, you've been like the big bro, thanks for all the discussions on work and other things, and for being someone who'd stand up for the right things, and also know how to not take everything so seriously :)

Veronika for a really good time off work, and at work battling Fresnel factors, wish you all the best for winding up your PhD soon! **Patrick**, the most organized person I know, (no cover letter ;)), **Max** (I guess you should be up defending soon, if not before me already :)), and **Alessandro** (congratulations, you've done really well so far) for being lovely group mates**; Shumei, Lisa, Simon Schlegel**, **Jan, and Christoph** for all the introductory help; **Johannes Franz** for time in Dolly, for setting high standards, and my first SFG spectrum; **Mike** for the rituals and ways to tame Veronica, even during Christmas; **Keno, Ulmas, Kevin, Marco, Yujen, Yelena, Peng, Daria, Azade, Laura, Amelie, and Ivan** for a good time at the institute. **Hai** and **Leonie** and their beautiful girls, for being such nice neighbours and friends. Also, **Anna Kunert Backes** from MPIC, and **Gabriele Sosso** from University of Warwick for great collaborative work.

Clara, for her inquisitiveness and assertiveness, it was fun being in the lab with you, however little. **Mirela**, i wish you maintain the same level of positivity and cherpiness throughout your PhD :)

Amala, Sergio, Grazia (can't forget Freeletics!), and Jonas for being the very benevolent, open, and wonderful friends: always there for whatever I'd need, you're just wonderful people! Also Natalia, Vasilios, Antonis, Dimitra, Todd for the memorable time outside, it was a pleasure. Sudipta for being a good group member and friend (agle adhyaay ke liye bahut shubhkaamnayen!), and Soham, albeit overlapping for a very short period.

My lovely office mates, even though you hardly saw me since covid: Alex for all the wonderful time, mostly outside of work, it has been a pleasure, Giovanni for all the laughs and good times, not to forget Mária ;) Heng for all the good conversations on life and on science, and also Lukas, Mayank, Xiaoxing, and Qu Sheng; and of course the frequent visitors to the office, most prominently Wenhao for always smiling and the amazing positivity :)

Also a couple of friends outside of the institute but who still provided support and help in their own ways. Harshita Bhatia, for being always there in all these years, to listen to my rants, and many a times give me the strength to get going. Nayancee Pandey for being someone with whom I could totally be myself, and for being such a strong support system. Akash Singh for inspiring me to keep my spirits up, and look at the brighter side.

Simon Bretschneider for sticking with my countless melodramatic times, the many ups and downs, and falls and breaking limbs :P for help on the thesis, and the many question-answer sessions, for the late night snack deliveries during lab time, for handling my pre-talk anxieties with some liquid courage (or placebos), and some solid technical feedback. Thank you for having been there, throughout.

My family: Rajendra Kumar, Kiran Sudera, Prateek Sudera: for believing in me, for the constant support, for all the love and care, for having my back. Aap teenon ho toh jahaan hai.

Paniz, I'd not imagined doing this with you not being there, but in some absurd ways you still are. This is also for you. And Eduard, it was not easy to see you go.